Journal of Engineering Design and Technology

Vol. 26 No. 1 March 2026

POLITEKNIK NEGERI BALI

logic

p-ISSN. 1412-114X

e-ISSN. 2580-5649

LOGIC

Jurnal Rancang Bangun dan Teknologi

LOGIC

Jurnal Rancang Bangun dan Teknologi

Journal of Engineering Design and Technology

Gedung P3M, lt.1 Politeknik Negeri Bali, Bukit Jimbaran
PO BOX 1064 Kuta Selatan, Badung, Bali - Indonesia
Telp. (+62)361 701981 Fax. (+62)361 701128
Email: logic@pnb.ac.id

LOGIC JOURNAL TEAM

PREFACE

Logic: Jurnal Rancang Bangun dan Teknologi (Journal of Engineering Design and Technology) is a peer-reviewed research journal aiming at promoting and publishing original high quality research in all disciplines of engineering and applied technology. All research articles submitted to Logic should be original in nature, never previously published in any journal or presented in a conference or undergoing such process across the world. All the submissions will be peer-reviewed by the panel of experts associated with particular field. Submitted papers should meet the internationally accepted criteria and manuscripts should follow the style of the journal for the purpose of both reviewing and editing.

Logic is a journal covering articles in the field of civil and mechanical engineering, design, and technology published 3 times a year in March, July, and November. Language used in this journal is English.

LOGIC. P-ISSN 1412-114X
LOGIC. E-ISSN 2580-5649
Indexing : GOOGLE SCHOLAR, DOAJ, EBSCO OPEN SCIENCE DIRECTORY, SINTA, GARUDA

Best Regard,

LOGIC Editorial Team

TABLE OF CONTENTS

LOGIC
Journal of Engineering Design and Technology
Vol. 26 No.1 March 2026 ; p. 1 - 9

p-ISSN : 1412-114X
e-ISSN : 2580-5649
http://ojs2.pnb.ac.id/index.php/LOGIC

EFFECT OF WASTE PLASTIC AS A BINDER ON COMPRESSIVE STRENGTH, WATER ABSORPTION, AND ABRASION RESISTANCE OF PAVING BLOCKS

Risman Firman [1)*], Joey Limbongan [1)], Muhammad Ali Taufan [1)]

1) Department Civil Engineering, Institut Teknologi Bacharuddin Jusuf Habibie, Parepare, Indonesia

Correponding email [1)*] :
risman@ith.ac.id

Abstract. The increasing accumulation of plastic waste has become a serious environmental problem, particularly in developing countries where waste management systems remain limited. A large proportion of plastic waste ends up in landfills or pollutes terrestrial and marine environments due to its non-biodegradable nature. One potential solution to this issue is the utilization of plastic waste as an alternative material in the construction sector. This study aims to evaluate the potential use of plastic waste as a binding material in the production of paving blocks and to analyze its influence on the mechanical and physical properties of the resulting product. This research employed an experimental laboratory approach using plastic waste consisting of polyethylene terephthalate (PET), polypropylene (PP), and low-density polyethylene (LDPE), processed through a melting method and mixed with fine sand. The mixture compositions included 100% plastic, 75% plastic : 25% sand, 50% plastic : 50% sand, and 25% plastic : 75% sand. The produced specimens were then tested for compressive strength, water absorption, and abrasion resistance in accordance with relevant testing standards. The results indicate that the mixture containing 75% plastic and 25% sand exhibited the most optimal performance, with a compressive strength of 11.64 MPa, water absorption of 1.32%, and abrasion resistance of 0.098 mm/min. In general, a higher plastic proportion improved compressive strength and reduced material porosity. These findings demonstrate that plastic waste has strong potential as an environmentally friendly alternative material for sustainable paving block production.

Keywords : Plastic waste, Paving blocks, Compressive strength, Water absorption, Abrasion resistance.

1. INTRODUCTION

Plastic waste continues to pose a major environmental challenge in many developing countries. The ongoing growth in global plastic production has led to a substantial increase in waste that is highly resistant to decomposition, thereby impacting both terrestrial and aquatic ecosystems as well as human health. Inadequate plastic waste management contributes significantly to marine pollution and deteriorates soil quality due to its slow degradation rate and the accumulation of microplastics [1], [2]. Moreover, only a small fraction of global plastic waste is actually recycled through formal waste management systems [3].

Indonesia, as one of the major contributors to global plastic waste, faces significant challenges in managing this type of waste [4], [5]. The accumulation of plastic in landfill sites not only leads to soil degradation and water contamination but also poses a threat to local ecosystems through the release of hazardous substances and the physical disruption of soil structures [6].

In response to this issue, increasing attention has been directed toward converting plastic waste into a valuable resource through circular economy approaches in the construction sector. One potential solution is the use of recycled plastics as a component in building materials, particularly for the production of paving blocks [7]. This strategy not only reduces reliance on natural aggregates and cement, whose manufacturing processes generate significant carbon emissions, but also helps minimize the accumulation of plastic waste in landfills and the surrounding environment [8], [9].

Several experimental studies have shown that plastics such as PET, PP, and LDPE can be utilized in paving block mixtures. For example, recent studies indicate that the incorporation of PET plastic waste in paving blocks can influence mechanical properties such as compressive strength and water absorption, although the resulting products may still meet certain quality standards [10]. In addition, other studies on the use of recycled plastics as binder materials or as substitutes for aggregates have demonstrated that specific mix formulations are capable of producing paving blocks with good abrasion resistance and relatively low water absorption [11].

A number of studies in the literature report that incorporating plastic waste as an aggregate component in lightweight concrete can lower the overall density of the material and broaden the development of sustainable construction materials. Nevertheless, this modification is commonly associated with a decrease in compressive strength, mainly attributed to the higher porosity introduced into the concrete matrix [12]. In addition, several review studies emphasize that careful optimization of the plastic content, improvement of plastic surface properties, and the use of appropriate processing techniques are essential to mitigate the negative effects on mechanical performance and long-term durability [13].

In Indonesia, while several studies have explored the use of plastic in paving blocks, for example by partially replacing fine aggregates with PET, research investigating the long term performance of these materials under tropical climatic conditions is still very scarce [14]. In addition, most existing studies rely on conventional approaches, such as limited substitution of sand or cement, and do not integrate multiple types of plastics with varying melting points and physical characteristics into a single, unified production process.

Consequently, this study introduces an integrative method that combines PET, PP, and LDPE using a smart melting technique followed by multi-layer mixing. This approach allows for the utilization of mixed plastic waste without the need for rigorous sorting, while enhancing the microstructure and uniformity of the resulting paving blocks. The study will assess how varying plastic ratios influence compressive strength, abrasion resistance, and water absorption through standardized testing procedures.

2. METHODS

This study employs a quantitative experimental approach conducted entirely in the laboratory [15]. Through this approach, each variation of the mixture between liquid plastic and sand is tested to examine how the composition affects its physical and mechanical properties, specifically compressive strength, water absorption, and abrasion resistance.

The population in this study comprises all paving blocks that can be produced from mixtures of liquid plastic and sand with various composition ratios. From this population, four mixture variations were selected: 100% plastic, 75% plastic : 25% sand, 50% plastic : 50% sand, and 25% plastic : 75% sand, based on the proportion of plastic by weight relative to sand.

The plastic waste used in this study consisted of a mixture of polyethylene terephthalate (PET), polypropylene (PP), and low density polyethylene (LDPE). To minimize phase separation due to differences in melting temperatures, the processing was carried out based on the thermal characteristics of each polymer. The optimum processing temperature was determined through preliminary trial heating, considering the melting ranges of LDPE (110-130°C), PP (160-170°C), and PET (250-260°C). The operating temperature was controlled within an effective range that allowed the lower-melting polymers to fully melt and act as the binding matrix, while the higher-melting polymers remained in a softened state to ensure homogeneous dispersion without thermal degradation.

Mechanical hot mixing was employed in the production process. The shredded plastics were first melted and continuously stirred until a homogeneous mixture was achieved, after which sand was gradually added while maintaining constant mixing to ensure uniform aggregate distribution and prevent segregation. The polymer blend ratio within the plastic fraction was set at 33.33% LDPE, 33.33% PP, and 33.33% PET (by weight sand) and was kept constant across all plastic–sand mixture variations to maintain experimental consistency.

For each mixture variation, five specimens were prepared, resulting in a total of 20 samples for each type of test. This number was applied consistently across all testing procedures, including compressive strength testing, water absorption testing, and abrasion resistance testing. Thus, each test was conducted using 20 specimens, ensuring more reliable and representative results in evaluating the influence of plastic-sand composition on the properties of the paving blocks.

2.1 Materials

Plastic waste was collected, cleaned, and then cut into small pieces to facilitate the melting process as shown in Figure 1. Fine sand was used as the aggregate. The main equipment consisted of a metal pan for melting, a heater, a stirring tool, paving block molds, a press machine, a digital scale, a soaking tank, a Universal Testing Machine (UTM), and an abrasion machine.

Figure 1. Plastic waste sorting and shredding process

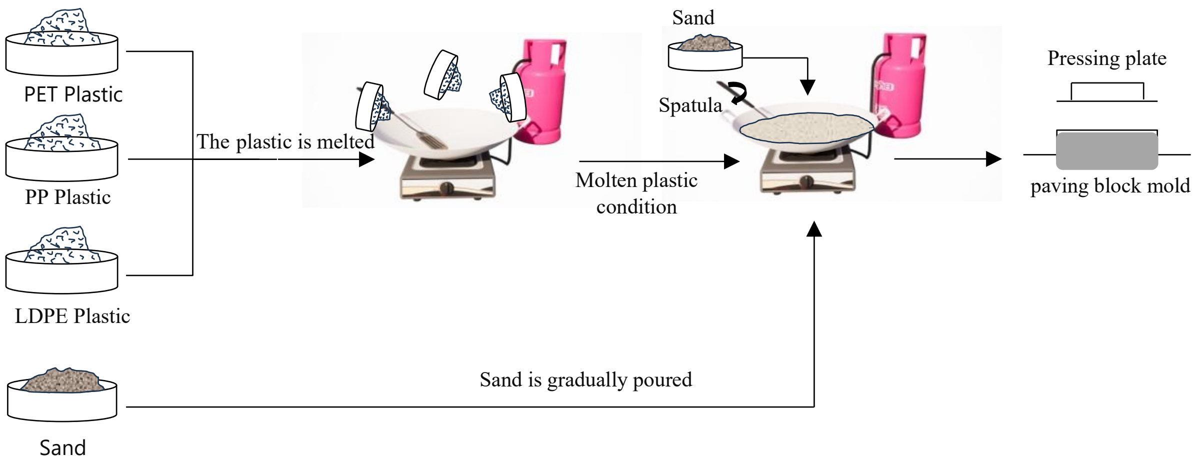

Figure 2. Steps in the production process of paving blocks from plastic waste–sand mixtures

2.2 Sample Preparation Procedure

The paving block was prepared according to the production diagram as seen in Figure 2. The initial stage involved melting the plastics using a metal. Detailed composition of each ingredients is shown in Table 1. Each type of plastic was processed individually according to its melting temperature to prevent thermal degradation and ensure optimal melting. LDPE was melted at 110-130°C, PP at 160-170°C, and PET at 250-260°C. Each plastic was maintained in a molten state for approximately 10-15 minutes after reaching the target temperature, with slow and continuous stirring to ensure uniform heat distribution.

Table 1. Mix Design Paving Block

No.	Mix Variation		Plastic Weight (gram)			Sand Weight (gram)
			PET	PP	LDPE	
1	100	0	736	491	507	-
2	75	25	552	368	380	673
3	50	50	368	245	253	1346
4	25	75	184	123	127	2018

Once the plastic reached a stable liquid state, sand was gradually added while stirring for approximately 5–7 minutes until a visually homogeneous mixture was obtained. The gradual addition of sand aimed to prevent agglomeration and ensure an even distribution of aggregates within the plastic matrix. The homogeneous mixture was then transferred into paving block molds and compacted using a conventional press. Specimens were allowed to cool at room temperature until fully hardened before testing. Homogeneity of the mixture was confirmed through visual inspection of the fracture surface, which showed evenly distributed sand without large voids or material segregation.

(a) (b) (c)

Figure 3. (a) Plastic weighing process, (b) Melting process, (c) Molding process

The molds were subjected to pressure using a conventional pressing machine to compact the mixture thoroughly. After this process, the specimens were left to cool at room temperature until fully hardened before testing. The complete process of sample preparation is shown in Figure 3.

2.3 Testing Procedures

a. Compressive Strenght (SNI 1974:2011)

Each sample was placed in a Universal Testing Machine (UTM). Load was applied gradually until the specimen showed signs of failure. The compressive strength value was calculated using the equation:

$$\sigma = P/A \tag{1}$$

Description:
σ = Compressive strength (MPa)
P = Maximum applied load (N)
A = Loaded surface area (mm²)

b. Water Absorption

Prior to testing, samples were weighed in their dry condition. Then, each sample was immersed in clean water for 24 hours. The weight after immersion was recorded, and the water absorption value was calculated using the formula:

$$\text{Water Absorption (\%)} = \frac{W_2 - W_1}{W_1} \times 100\% \tag{2}$$

Description:
W_1 = Dry weight (g)
W_2 = Weight after immersion (g)

c. Abrasion resistance (SNI 03-0028-1987)

Abrasion testing was conducted using a standard abrasion machine. Samples were rotated or rubbed against an abrasive surface for a specified duration. The difference in weight before and after the test was used to calculate the wear rate.

$$D = 1.26\ G \times 0.0246 \tag{3}$$

Description:
D = Abrasion loss (mm/min)
G = Mass loss (g/min)

3. RESULTS AND DISCUSSION

3.1 Compressive Strength Of Paving Blocks

This section presents the results of compressive strength and water absorption tests on variations of plastic-sand-based paving blocks, and discusses the influence of plastic composition on the material's mechanical performance. The analysis was conducted to identify the optimal mix ratio and to understand the strengthening mechanisms occurring within the composite structure.

The data presented in Figure 5 and Figure 6 show that compositions with higher plastic content yield better compressive performance. The mixture with 75% plastic and 25% sand recorded the highest compressive strength at 11.64 MPa. The 100% plastic composition also exhibited a relatively high compressive strength of 10.82 MPa. However, when the sand proportion increased, the performance declined significantly; the 25% plastic and 75% sand ratio reached only 8.91 MPa, making it the variation with the lowest value.

This phenomenon indicates that under the processing conditions used, plastic appears to act as a more dominant binding matrix compared to sand. This finding aligns with studies on plastic–sand interlocking blocks, which report that an increased plastic fraction can produce a more compact structure because the molten polymer is able to coat and bind sand grains more uniformly, thereby enhancing the compressive strength of the material [16]. Similar results have been observed in PET-sand brick research, where a polymer matrix processed at appropriate melting temperature can form a dense and stable structure, thus contributing significantly to mechanical strength despite a lower aggregate content [17]. Furthermore, other studies have demonstrated that increasing the proportion of certain plastics (e.g., HDPE or PET) in the mixture can improve mechanical performance and material durability, provided that the composition and melting process are properly controlled [18].

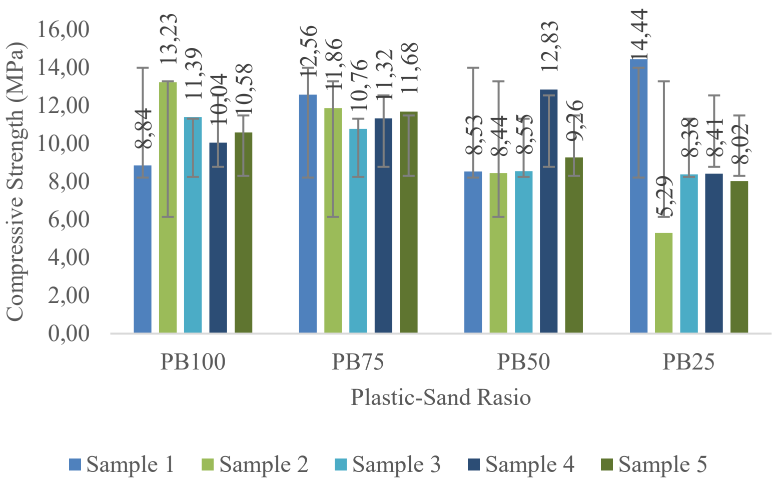

Figure 4. Compressive strength variations of paving blocks with different plastic-sand ratios

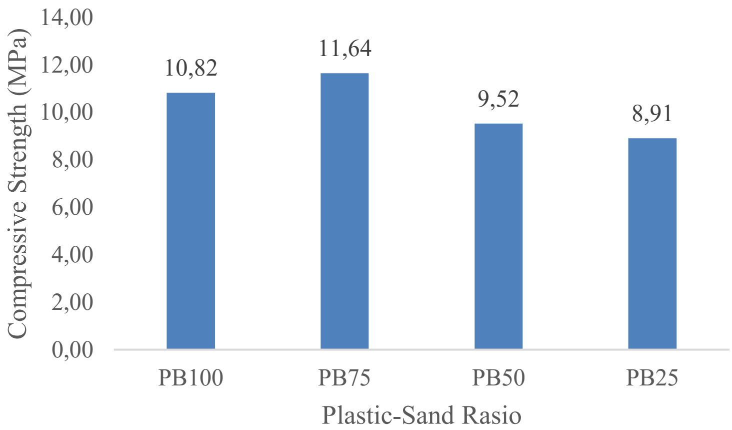

Figure 5. Average compressive strength of paving blocks with varying plastic-sand ratios

The 75% plastic composition performs better than 100% plastic because it provides an optimal balance between the plastic binder and the sand aggregate. At this ratio, the plastic is sufficient to coat and adhere to the sand grains evenly, allowing the load to be distributed more effectively throughout the material. The bond between the plastic and sand helps spread stress uniformly, reducing weak points that could lead to cracking. In contrast, the 100% plastic composition lacks enough sand as a structural filler, so even though the plastic matrix is dense, overall stiffness and stress distribution are less effective. Therefore, the 75% plastic : 25% sand ratio produces a composite structure that is more stable, compact, and mechanically stronger.

When the compressive strength values are compared with the SNI 03-0691-1996 standard, two variations 100% plastic and 75% plastic : 25% sand have met the minimum requirement for Quality Class D, which stipulates an average compressive strength above 10 MPa. Therefore, these two compositions have the potential for application in light to medium-duty uses, particularly in pedestrian areas, residential yards, or public facilities with low loading.

These finding also indicate that the liquid plastic-based bonding system in this study tends to perform optimally when the aggregate content is not excessively high, as an excess of sand can hinder the formation of a compact polymer matrix. This factor should be carefully considered in the further development of plastic waster based paving block products.

3.2 Water Absorption

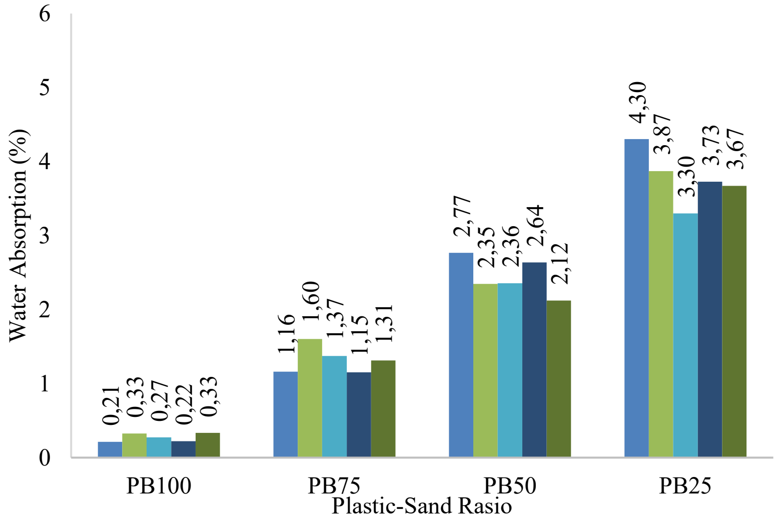

Figure 6. Percentage of water absorption in paving block samples with various plastic

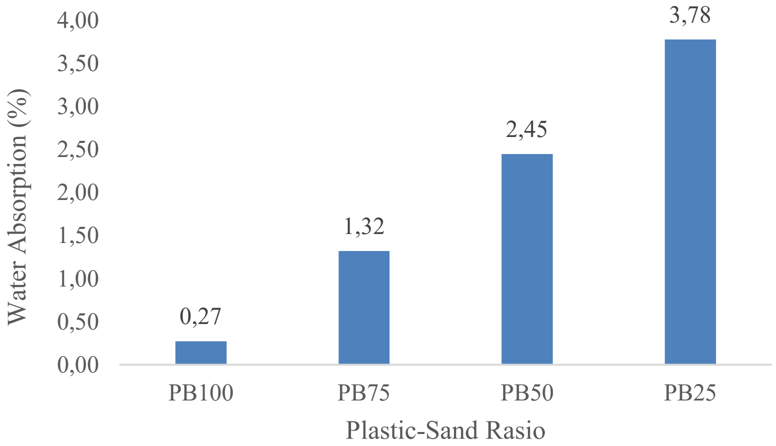

Figure 7. Average water absorption of paving blocks with varying plastic-sand ratios

This section discusses the results of water absorption tests on plastic-sand based paving blocks. Water absorption is an important indicator for assessing the material's resistance to water penetration, which affects the durability and quality of the paving blocks. The analysis was conducted to evaluate the influence of varying plastic-to-sand ratios on the blocks' water absorption capacity, in order to identify the optimal composition. The test results were subsequently compared with the SNI 03-0691-1996 standard to assess the material's compliance in terms of quality class.

Figure 7 and Figure 8 illustrates an interesting pattern of water absorption in paving blocks with varying plastic-sand mixture ratios. The 100% plastic composition exhibited the lowest absorption rate, whereas the block with a 25% plastic : 75% sand ratio showed the highest water absorption. This decrease in absorption is consistent with the increasing proportion of plastic. Compared to the SNI 03-0691-1996 standard, the water absorption values of the high-plastic-content variations fall within Quality Classes A (3%) and B (6%), while the maximum limit for Class D according to the standard is 10%.

These findings reinforce the hypothesis that plastic in the mixture acts as a matrix filler that seals pores and reduces water penetration. This is consistent with the results reported by Mildawati (2023), who found that the addition of waste PP in paving blocks led to increased water absorption, and at low plastic proportions, porosity rose drastically [19]. Similarly, a study using recycled LDPE demonstrated that at a pure plastic composition (100%), water absorption was very low, approximately 0.317% [20].

The low water absorption in blocks with dominant plastic content is likely due to the non-hygroscopic nature of the polymer: molten plastic can form a coating layer around sand grains, reducing capillary pores within the material. This is supported by pragmatic research, such as the study by Fauzi & Mustakim, which showed that polypropylene-based paving blocks exhibit relatively low water absorption at certain ratios due to a sufficiently dense polymer-sand bonding [21].

The effect of low water absorption is crucial from a structural feasibility perspective; the reduced internal porosity makes the blocks more resistant to chemical reactions, physical stresses, and mechanical loads. This factor contributes to a longer service life by limiting water ingress, which can cause cracking. Conversely, increased water absorption in blocks with higher sand content indicates higher porosity, which can accelerate the decline in compressive strength and increase the risk of structural damage such as cracking or breaking over time.

3.3 Abrasion Resistance

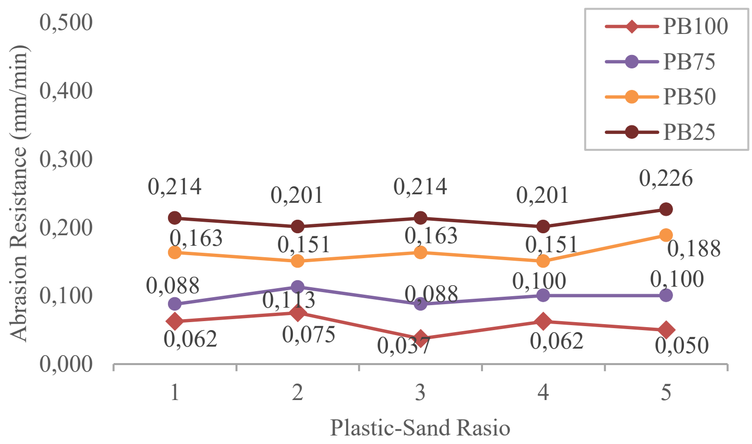

Figure 8. Percentage of abrasion resistance of paving blocks with various plastic-sand mixture ratios

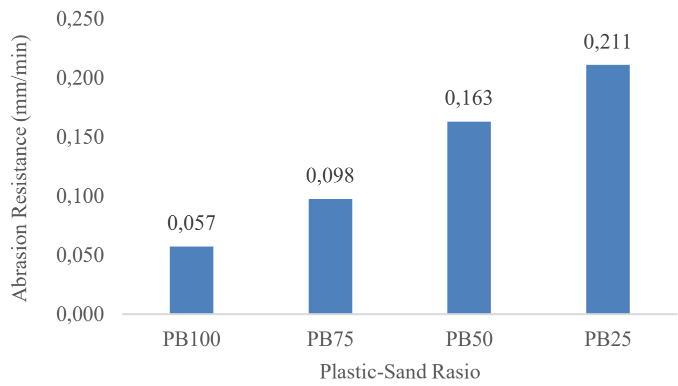

Figure 9. Average abrasion resistance of paving blocks with varying plastic-sand ratios

This section presents the results of abrasion tests on plastic-sand based paving blocks. Abrasion resistance is a key parameter for evaluating surface durability and long-term performance under frictional wear. The analysis focuses on the effect of varying plastic-to-sand ratios on the rate of material wear, highlighting the role of plastic in enhancing surface strength. The results provide insight into optimal compositions that improve abrasion resistance, which is critical for practical applications under different load and traffic conditions.

Figure 9 and Figure 10 illustrates the abrasion trends of paving blocks with varying plastic-to-sand ratios: the higher the sand proportion, the faster the material wears. For instance, in the PB100 variation (100% plastic), the abrasion rate ranges between 0.037 and 0.062 mm/min, whereas in PB25 (25% plastic : 75% sand), the wear rate sharply increases to approximately 0.201-0.226 mm/min. These findings clearly demonstrate that a high plastic content significantly enhances the abrasion resistance of paving blocks.

The thermoplastic properties of LDPE and PP make the material more flexible, so when friction occurs, the surface is less prone to cracking or breaking. Plastics tend to distribute and absorb shear forces, thereby reducing abrasion. This is supported by previous research where Rajat Akrawal et al. (2023) reported that paver blocks with a high plastic proportion (LDPE/PP) exhibited lower abrasion values compared to mixtures with low plastic content [22].

Table 2. Paving Block Quality Standards of SNI-03-0691-1996

Grade	Compressive Strength (MPa)		Abrasion Resistance (mm/menit)		Average Water Absorption (%)
	Average	Min	Min	Average	
A	40	35	0.09	0.103	3

B	20	17	0.130	0.149	6
C	15	12.5	0.160	0.184	8
D	10	8.5	0.219	0.251	10

According to the SNI 03-0691-1996 standard, the PB100 and PB75 variations are classified as Quality Class A, PB50 falls into Class C, and PB25 is categorized as Class D due to its relatively high abrasion (Table 2.). These results demonstrate that selecting the plastic ratio is not merely a matter of material substitution but is closely related to physical durability against abrasion. The low wear coefficient of blocks with dominant plastic content can be a significant advantage in applications requiring resistance to friction, such as pedestrian sidewalks or other light-use areas.

4. CONCLUSION

This study demonstrates that plastic waste can effectively function as a binder material for paving blocks, where an increased plastic proportion results in improved mechanical performance. Among the tested variations, the 75% plastic : 25% sand composition exhibited the most optimal performance, with a compressive strength of 11.64 MPa, water absorption of 1.32%, and abrasion resistance of 0.098 mm/min. The 100% plastic variation also showed high performance, with a compressive strength of 10.82 MPa and abrasion rates between 0.037 and 0.062 mm/min, while the low-plastic mixture (25%) experienced a significant decline in performance, with a compressive strength of 8.91 MPa, water absorption of 3.78%, and abrasion rates of 0.201–0.226 mm/min. Therefore, the best performance was achieved at the 75% plastic : 25% sand ratio, indicating the optimal combination of strength, abrasion resistance, and water absorption. According to SNI 03-0691-1996, the PB100 and PB75 variations meet Class A quality, PB50 falls into Class C, and PB25 is categorized as Class D. Overall, a high plastic ratio has been proven to produce paving blocks with low porosity, high abrasion resistance, and better mechanical performance, indicating the great potential of plastic waste as a sustainable construction material. These paving blocks have specific prospective applications as materials for sidewalks, pedestrian pathways, parking areas, light-duty roads, and as an eco-friendly alternative in modular or prefabricated construction systems.

5. REFERENCES

[1] S. Waghmare, M. Kshirsagar, and M. Date, "Impacts of microplastics in soils due to connected built environments, identification challenges, and regulating policies: A ComprehensiveReview," 2025, *Springer Science and Business Media Deutschland GmbH*. doi: 10.1007/s43995-025-00235-9.

[2] R. S. Yu and S. Singh, "Microplastic Pollution: Threats and Impacts on Global Marine Ecosystems," Sep. 01, 2023, *Multidisciplinary Digital Publishing Institute (MDPI)*. doi: 10.3390/su151713252.

[3] K. Novakovic *et al.*, "Zero-waste circular economy of plastic packaging: The bottlenecks and a way forward," *Sustainable Materials and Technologies*, vol. 38, p. e00735, 2023, doi: https://doi.org/10.1016/j.susmat.2023.e00735.

[4] A. T. Purwandari, A. Ratnamirah, N. Parwati, and W. N. Tanjung, "Determining optimum eco paving block compositions by using factorial design method," in *IOP Conference Series: Materials Science and Engineering*, Institute of Physics Publishing, May 2020. doi: 10.1088/1757-899X/847/1/012008.

[5] P. Lestari, G. Purwiandono, A. N. Amalia, E. K. I. Ma'Rufi, M. R. Firdaus, and D. Wacano, "Coexistence of microplastic particles and heavy metals in landfill leachate: A case study of a landfill in Indonesia," *Case Studies in Chemical and Environmental Engineering*, vol. 11, p. 101082, 2025, doi: https://doi.org/10.1016/j.cscee.2024.101082.

[6] K. Manikanda Bharath, A. L. Muthulakshmi, and U. Natesan, "Microplastic contamination around the landfills: Distribution, characterization and threats: A review," *Curr. Opin. Environ. Sci. Health*, vol. 31, p. 100422, 2023, doi: https://doi.org/10.1016/j.coesh.2022.100422.

[7] P. O. Awoyera and A. Adesina, "Plastic wastes to construction products: Status, limitations and future perspective," *Case Studies in Construction Materials*, vol. 12, p. e00330, Jun. 2020, doi: 10.1016/J.CSCM.2020.E00330.

[8] A. I. Almohana, M. Y. Abdulwahid, I. Galobardes, J. Mushtaq, and S. F. Almojil, "Producing sustainable concrete with plastic waste: A review," *Environmental Challenges*, vol. 9, p. 100626, Dec. 2022, doi: 10.1016/J.ENVC.2022.100626.

[9] B. Iftikhar *et al.*, "Experimental study on the eco-friendly plastic-sand paver blocks by utilising plastic waste and basalt fibers," *Heliyon*, vol. 9, no. 6, Jun. 2023, doi: 10.1016/j.heliyon.2023.e17107.

[10] Fauzan, R. F. Zakaria, M. D. A. Nugraha, and Z. Al Jauhari, "THE EFFECT OF PET AND LDPE PLASTIC WASTES ON THE COMPRESSIVE STRENGTH OF PAVING BLOCKS," *International Journal of GEOMATE*, vol. 24, no. 101, pp. 94–101, 2023, doi: 10.21660/2023.101.g12250.

[11] R. H. Kibiina, S. Biira, E. B. Amabayo, and R. Akoba, “Performance evaluation of the paving blocks moulded with plastic waste as a binding material,” *Discover Environment*, vol. 3, no. 1, Dec. 2025, doi: 10.1007/s44274-025-00292-w.

[12] N. Pereira Soares, M. Gonçalves Marques, L. Carvalho Mesquita, A. R. Garcez de Azevedo, and M. Teixeira Marvila, “Recycled Plastic Waste as Aggregates in Lightweight Concrete: A Study of Saturation Effects,” *Journal of Sustainability*, vol. 1, no. 1, Jun. 2025, doi: 10.55845/jos-2025-1114.

[13] P. Minde, M. Kulkarni, J. Patil, and A. Shelake, “Comprehensive review on the use of plastic waste in sustainable concrete construction,” Dec. 01, 2024, *Discover*. doi: 10.1007/s43939-024-00126-1.

[14] A. Surya, D. A. Al Anzari, A. Juniarti, and A. Setiawan, “Pemanfaatan Limbah Plastik Polyethylene Terephthalate Sebagai Pengganti Agregat Halus Dalam Pembuatan Paving Block,” *Jurnal Ilmiah Ecosystem*, vol. 21, no. 3, pp. 526–531, Dec. 2021, doi: 10.35965/eco.v21i3.1078.

[15] R. Firman, J. Limbongan, Y. Febry Fitriani Sofyan, S. Satar, A. Tamsil Yunus, and A. Widiasari Maruddani, “Optimization of High Early-Strength Concrete Mix Design for Structural Applications in the BJ. Habibie Stadium Construction Project,” *Civilla: Jurnal Teknik Sipil Universitas Islam Lamongan*, vol. 10, no. 2, pp. 123–132, Sep. 2025, doi: 10.30736/cvl.v2i2.

[16] A. Kumi-Larbi Jnr, L. Mohammed, T. A. Tagbor, S. K. Tulashie, and C. Cheeseman, “Recycling Waste Plastics into Plastic-Bonded Sand Interlocking Blocks for Wall Construction in Developing Countries,” *Sustainability (Switzerland)*, vol. 15, no. 24, Dec. 2023, doi: 10.3390/su152416602.

[17] F. I. Aneke, B. O. Awuzie, M. M. H. Mostafa, and C. Okorafor, “Durability assessment and microstructure of high-strength performance bricks produced from pet waste and foundry sand,” *Materials*, vol. 14, no. 19, Oct. 2021, doi: 10.3390/ma14195635.

[18] K. Gounden, F. M. Mwangi, T. P. Mohan, and K. Kanny, “Improving the performance properties of plastic-sand bricks with Kaolin Clay,” *Environ. Dev. Sustain.*, 2024, doi: 10.1007/s10668-024-05788-8.

[19] R. Mildawati, “Pengaruh Penambahan Limbah Plastik Sebagai Campuran Beton Terhadap Kuat Tekan dan Daya Serap Air Pada Paving Block,” *JURNAL SAINTIS*, vol. 23, no. 02, pp. 27–34, Dec. 2023, doi: 10.25299/saintis.2023.vol23(02).7966.

[20] Firman, R. Ismy, and A. Malik, “Analisis Dampak Produksi Paving Block Menggunakan Plastik Jenis Low Density Polyethylene (LDPE) Terhadap Pengurangan Limbah Plastik,” *Future Academia : The Journal of Multidisciplinary Research on Scientific and Advanced*, vol. 3, no. 2, pp. 800–813, May 2025, doi: 10.61579/future.v3i2.506.

[21] M. A. F. Fauzi, M. Mustakim, and A. B. Didi, “Compressive Strength Analysis and Water Absorption of Paving Blocks Made from Polypropylene Plastic Seeds,” *Journal of Civil Engineering and Planning*, vol. 6, no. 1, pp. 1–8, Jun. 2025, doi: 10.37253/jcep.v6i1.10200.

[22] R. Agrawal *et al.*, “Utilization of Plastic Waste in Road Paver Blocks as a Construction Material,” *CivilEng*, vol. 4, no. 4, pp. 1071–1082, Dec. 2023, doi: 10.3390/civileng4040058.

LOGIC
Journal of Engineering Design and Technology
Vol. 26 No. 1 Maret 2026; p. 10 - 16

p-ISSN : 1412-114X
e-ISSN : 2580-5649
http://ojs2.pnb.ac.id/index.php/LOGIC

AUTOMATIC *POLYALUMINIUM CHLORIDE* (PAC) DOSING CONTROL SYSTEM FOR WATER PURIFICATION USING NODEMCU-ESP32

1) Instrumentation and Control Engineering Technology, Politeknik Negeri Indramayu, Jawa Barat, Indonesia.
2) Refrigeration Engineering and Air Conditioning, Politeknik Negeri Indramayu, Jawa Barat, Indonesia.

Correponding email [1)*] :
fauzanamri@polindra.ac.id

Fauzan Amri [1)*], Bagus Dharmawan Hadi [1)], Tri Haryanti [2)], Revan Lutfiar Rizky [1)], Sri Rahayu [1)], Aulia Wanda Alifah [1)]

Abstract. This study discusses the design and implementation of a control system for a water pump used to inject PAC solution into raw water, thereby producing treated water that meets quality standards. The pump's operating duration is adaptively controlled based on the turbidity level of the water to be clarified. The system employs a turbidity sensor as the input signal, which generates data to be processed by a NodeMCU-ESP32 device serving as the central controller. Subsequently, the controller issues commands to the water pump, functioning as the actuator, to perform the PAC injection process. Experiments were conducted on three types of water sources, namely river water, paddy field water, and groundwater, with initial turbidity levels of 29, 35, and 64 NTU, respectively. The results showed that all water samples were successfully clarified to a turbidity value of 0 NTU within 47, 120, and 137 minutes, respectively. At the beginning of the treatment process, turbidity value readings exhibited fluctuations due to the initial mixing of PAC solution with raw water. However, the turbidity values steadily decreased once the PAC and suspended particles were fully settled. To facilitate monitoring, the system is equipped with an IoT feature via the Firebase platform, which displays numerical indicators including water volume, turbidity level, pump speed, pump operating duration, and water status classified according to clarity. This innovation is expected to contribute as an effective water purification automation technology, expecially for small- and medium-scale clean water treatment facilities.

Keywords : Water pump, Polyalumunium Chloride (PAC), turbidity sensor, NodeMCU-ESP32, IoT

1. INTRODUCTION

The availability of clean water is a fundamental requirement for human life and public health [1], [2]. Clean water services are delivered through a series of raw water treatment processes designed to ensure water quality and safety [3]. One of the most crucial stages in this process is coagulation and flocculation, which aim to remove suspended particles and colloids responsible for water turbidity [4], [5]. At this stage, Polyaluminium Chloride (PAC) chemical is widely used as a coagulant due to its several advantages, including high effectiveness in precipitating contaminants, good flocculation and sedimentation capabilities, and a wide operational range of pH and temperature, while requiring only relatively low dosages [1], [6], [7].

The determination of PAC dosage in water treatment is generally carried out manually or semi-automatically through estimation or laboratory tests, such as the Jar Test [8], [9], [10], [11], [12]. Although effective, this method has several limitations, including low responsiveness to fluctuations in raw water quality, the risk of overdosing or underdosing that may affect both water quality and operational costs, as well as the absence of comprehensive and real-time data for optimal decision-making [12], [13]. Bello and Owoeye modeled the dosing pump control using Proportional Integral (PI), Proportional Integral Derivative (PID), and Model Predictive Control (MPC) techniques. The results indicated that MPC outperformed the other methods in both servo-control and regulatory-control responses, exhibiting faster rise time, shorter settling time, absence of overshoot, and superior set-point tracking capability compared to PI and PID [14]. In addition, Kurniawan *et al.*

conducted a study on the control of Palm Oil Mill Effluent (POME) quality using a PAC solution, processed through a fuzzy logic algorithm embedded in an Arduino Mega 2560. The findings demonstrated that the turbidity sensor effectively detected a reduction in wastewater turbidity from 160 to 138 Nephelometric Turbidity Units (NTU) within 12 minutes, with the results satisfying the regulatory standards for wastewater discharge [15]. Despite achieving turbidity levels below 150 NTU, the effluent turbidity remained relatively high, suggesting that further optimization of the treatment process is necessary to enhance effluent quality and ensure greater environmental protection prior to discharge. Fadliondi and Purwanto also constructed a motor pump control system for PAC dosing using a Programmable Logic Controller (PLC). The study demonstrated that the motor speed was adjusted according to the turbidity level of the raw water, enabling the PAC solution to be injected based on the required dosage. However, the experiment was limited to a single turbidity condition of 50 NTU with a motor speed of 375.36 rpm [16]. The absence of testing across multiple turbidity levels limits the comprehensiveness and generalizability of the research findings, as it does not provide sufficient evidence regarding the system's performance, stability, and responsiveness under varying raw water conditions that commonly occur in real operational environments.

Based on the aforementioned description, this study focuses on controlling pump operating duration according to raw water turbidity to adjust the PAC dosage required for the coagulation process. The system utilizes a turbidity sensor to measure water clarity and transmit data to a NodeMCU-ESP32 controller, which regulates pump activation and sends monitoring data to the Internet of Things (IoT) cloud platform for real-time display via Firebase. This approach is expected to enhance operational efficiency in the PAC dosing process and support the sustainable provision of clean water that meets regulatory standards [17].

2. METHODS

2.1 System Design

The water purification control system was designed using three main components: a turbidity sensor module to measure the turbidity level of raw water, a GP-129JXK Panasonic water pump to inject the PAC solution into the turbid water, and a NodeMCU-ESP32 serving as both the system controller and the internet interface. According to Figure 1(a), the turbidity sensor receives power from the 5V-GND pins, with its analog output routed to GPIO34 of the ESP32 through a resistor voltage divider circuit to ensure that the signal remains ≤ 3.3 V in accordance with the Analog-to-Digital Converter (ADC) operating limit. The ADC value represents digital data obtained from the conversion of the turbidity sensor's analog signal. The value then transforms into a voltage level for futher processing in the ESP32 [18], [19]. Subsequently, the module IR infrared obstacle sensor is connected to GPIO2 as a digital input. The relay is supplied from the 5V pin and controlled via GPIO23, functioning to connect or disconnect the current to the water pump. The primary power source is a 12 V adapter, which is converted to 5 V DC via a step-down module to supply the entire circuit. The overall system is illustrated in the form of a block diagram, as displayed in Figure 1(b).

Following the proper connection of all component pins as shown in Figure 1(a), the system was programmed using Arduino IDE 1.8.19, with the code shown in Figure 1(c). This sketch employs an ESP32 to monitor water quality using a turbidity sensor, an infrared sensor, and a relay module, with the acquired data transmitted to Firebase via WiFi. Sensor readings are processed using a median filter to reduce noise, while an interrupt routine is utilized to count RPM pulses, and the water status is classified based on NTU values. In summary, the program is designed to acquire sensor data with improved accuracy, control the pump, and present real-time water quality conditions through Firebase.

Real-time data display and internet connectivity were implemented through the Firebase platform, with the program code presented in Figure 1(d). The code from lines 1 to 139 represents a web-based water monitoring dashboard that integrates Bootstrap for layout design, Chart.js for data visualization, and the Firebase Realtime Database for real-time sensor data storage. The initial section defines the HTML structure, CSS styling, and sidebar navigation, followed by information cards displaying water volume, turbidity (NTU), RPM, pump operating duration, and water status, along with corresponding graphical visualizations. The final section contains the Firebase configuration, the *updateGauge* function for dynamically updating values and indicators, and the initialization of the RPM chart. Overall, this code constructs a monitoring interface that presents real-time sensor data in the form of numerical values, indicators, and graphical charts.

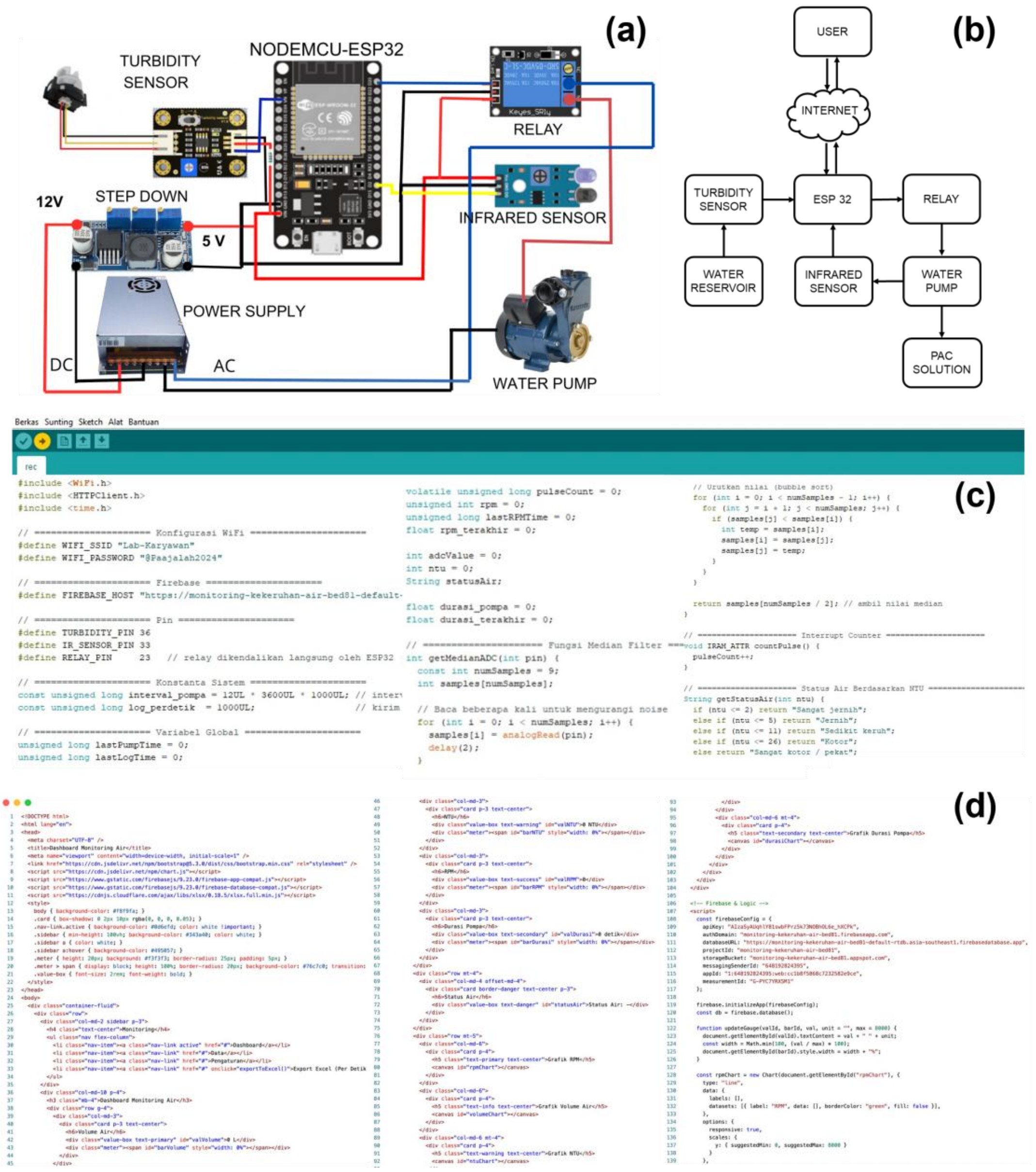

Figure 1. System architecture. (a) wiring diagram, (b) block diagram, (c) controller program code, and (d) firebase program code of the system.

2.2 Working Principle of System

The system operates by utilizing a turbidity sensor as an input device to measure the turbidity level of raw water. The measurement data are transmitted to the ESP32 microcontroller, which activates a relay to drive a water pump that injects PAC solution into the raw water reservoir. The water pump operation is adjusted according to the turbidity level, as presented in Table 1. An infrared sensor is installed on the water pump to measure its rotational speed. After the PAC solution is injected, the mixing process is performed conventionally for 15 minutes. Subsequently, turbidity measurements are performed in real-time and connected to the internet to facilitate remote monitoring. The water generally becomes clear within 47 to 137 minutes after the addition of the PAC solution. In this study, three types of raw water with different turbidity levels were examined, namely river water, rice field water, and ground water.

Table 1. The Pump Operating Duration Based on Water Turbidity

Turbidity Range (NTU)	Pump Operating Duration (second)
4 – 30	9.4
31 – 60	16.5

> 60	28.5

2.3 PAC Dosage and Turbidity Measurement

To clarify water using PAC chemical, a dosage of 13–130 ppm is required depending on the turbidity level of the raw water [20], [21], [22]. In this study, an 82.5 ppm PAC solution was applied to treat 5 liters of turbid water. The operating time of the water pump was regulated according to the measured turbidity level. The turbidity value of the raw water was calculated using Eq. (1), where T denotes the turbidity (NTU), a represents the slope of the linear relationship between turbidity variation and voltage, V is the output voltage of the turbidity sensor obtained from ADC-to-voltage conversion, and b indicates the intercept of the linear relationship [23].

$$T = a.V + b \tag{1}$$

The calibration process of the turbidity sensor is performed using standard solutions with known turbidity values, such as 0 NTU (distilled water) and several reference points (e.g., 50 and 100 NTU). The sensor is immersed in each solution, and the corresponding analog output voltage is recorded through a ESP32 microcontroller. The collected data are plotted to establish the relationship between output voltage and NTU value, from which a calibration equation—typically linear within a specific measurement range—is derived. Based on this calibration, the control system operates according to the predetermined threshold values obtained during the calibration stage. Measurement accuracy is evaluated by comparing sensor readings with the reference standards and calculating the percentage error. Under stable testing conditions, the sensor turbidity generally provides an accuracy of approximately ±5–10%, depending on calibration quality, optical cleanliness, and ambient lighting conditions.

3. RESULTS AND DISCUSSION

3.1 Water Purification Data

The designed system successfully operated in accordance with the implemented program. The system could clarify three types of water, with varying treatment durations depending on the initial turbidity level. Measurement data were recorded every 2.5 minutes through the Firebase platform and systematically stored in a digital dataset.

As shown in Figure 2(a), river water with an initial turbidity of 29 NTU was successfully clarified through the injection of a PAC solution using a water pump, resulting in a turbidity reduction to 0 NTU within 47 minutes. The turbidity sensor effectively detected changes in turbidity throughout the treatment period. However, the sensor readings exhibited fluctuations due to instability of the sensing device. This phenomenon is caused by the temporary stickiness of some PACs and suspended particles to the sensor probe, which reduces the light intensity received by the photodiode and results in elevated turbidity readings. After the particles settle, the light intensity received by the photodiode increases, and the turbidity readings decrease in accordance with the actual water clarity [24], [25]. A consistent decrease in turbidity values was observed during the last seven minutes prior to complete purification. Figure 2(b) shows the purification process of paddy field water with an initial turbidity of 35 NTU. A similar pattern was observed in the sensor readings, where turbidity values fluctuated during the early stages of measurement. However, a more consistent decline in turbidity was recorded, with minor noise detected within the first ten minutes. Figure 2(c) presents the turbidity data of ground water over time, with an initial value of 64 NTU. The purification process lasted for 137 minutes, during which turbidity readings were unstable and showed significant fluctuations at the 32nd and 60th minutes. Nevertheless, a consistent decrease in turbidity with minor noise occurred from the 65th minute until the final stage of purification. Furthermore, Figure 2(d) presents the pump operating duration based on the turbidity level of the water. The higher the turbidity, the longer the pump operating time required.

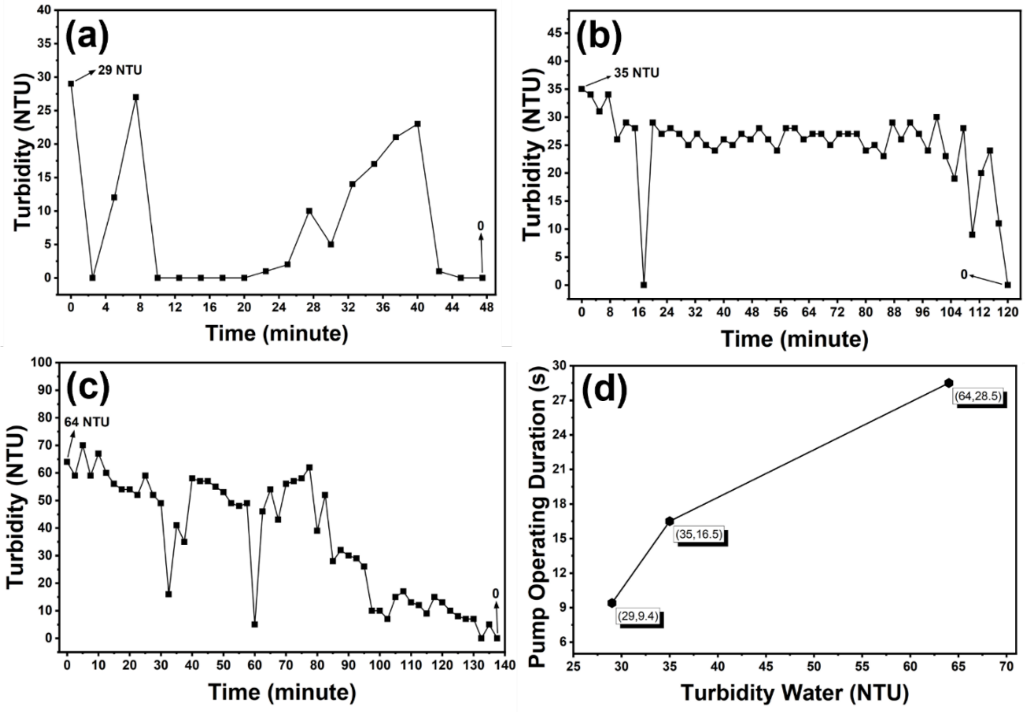

Figure 2. Experimental Data of Water Purification for Various Water. (a) River Water, (b) Rice Field Water, (c) Ground Water, and (d) Pump Operation Duration against Water Turbidity Level

The detailed experimental results of the clarification process for three types of raw water are presented in Table 2. It is observed that higher initial turbidity levels require longer treatment durations to achieve complete clarification (0 NTU). The 0 NTU value represents the actual measured turbidity for each sample and corresponds to the minimum detection limit of the turbidity sensor employed. The final outcome of the purification process is illustrated in Figure 3, demonstrating that within a specified time frame, all three types of raw water were successfully clarified automatically by the proposed system.

The experiments were conducted repeatedly to ensure system reliability and data consistency. Although minor variations were observed among the recorded results, these differences were not significant and did not affect the overall trend of the findings. Overall, the system exhibited stable performance and consistent responsiveness in regulating the pump operating duration according to the detected turbidity level. The water pump effectively injected the PAC solution into the raw water based on the measured turbidity value. The implementation of this prototype is expected to enhance the efficiency of PAC utilization, particularly in small- to medium-scale clean water treatment facilities.

Table 2. Results of Water Purification

Water Type	Initial Turbidity (NTU)	Final Turbidity (NTU)	Purification Duration (min)
River Water	29	0	47
Rice Field Water	35	0	120
Ground Water	64	0	137

Figure 3. Visual Comparison of Various Types of Water Prior to and Following Treatment

3.2 Website Dashboard Interface

The website provides a real-time dashboard for monitoring water quality. Numerical indicators include water volume (L), turbidity (NTU), pump speed (RPM), pump operating time (s), and water status categorized according to clarity (see Figure 4). Graphs of these parameters facilitate effective tracking of changes, while a side navigation panel offers system settings, Excel data export, and main page access. Integration with Firebase ensures real-time data storage and updates via the internet.

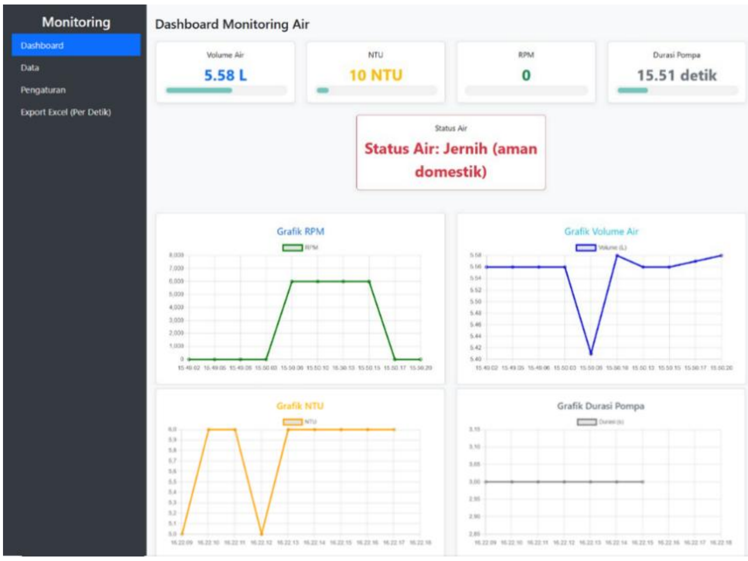

Figure 4. Website Dashboard Interface

4. CONCLUSION

This work successfully clarified various types of water automatically through the injection of a PAC solution into raw water. Three water sources with initial turbidity levels of 29, 35, and 64 NTU were clarified to a final turbidity of 0 NTU within 47, 120, and 137 minutes, respectively. At the beginning stage of the purification process, turbidity readings exhibited fluctuations caused by the stickiness of some PACs and suspended particles to the sensor probe, which affected the intensity of light captured by the photodiode. However, once these particles settled, turbidity readings decreased consistently. Overall, the turbidity sensor proved effective in detecting changes in the turbidity levels of the samples during the treatment process. For monitoring purposes, the system integrates an IoT feature through the Firebase platform, providing numerical indicators such as water volume, turbidity level, pump speed, pump operating time, and water status categorized by clarity.

5. ACKNOWLEDGEMENT

The authors gratefully acknowledge the financial support from the Directorate of Research and Community Service, Directorate of Research and Development, Ministry of Higher Education, Science, and Technology, provided through Contract No. 031/C3/DT.05.00/PL/2025 and Subcontract No. 1000/PL42.PL42.9/AL.04/2025.

6. REFERENCES

[1] S. O. Nti, R. Buamah, and J. Atebiya, “Polyaluminium chloride dosing effects on coagulation performance: case study, Barekese, Ghana,” *Water Pract. Technol.*, vol. 16, no. 4, pp. 1215–1223, 2021, doi: 10.2166/wpt.2021.069.

[2] I. Fitriyanto, T. Haryanti, I. Fatwasauri, and D. Putranto, “Perancangan Sensor Kekeruhan Air Menggunakan LED dan Photodiode Sebagai Pemancar dan Penerima Gelombang Cahaya,” *J. Ilm. Sutet*, vol. 14, no. 2, pp. 110–116, 2024.

[3] I. Fitriyanto, F. Amri, and R. Robiyanto, “Desain Meteran Air Prabayar Berbasis Sensor YF-S201 dengan Generator Air Mini Sebagai Catu Daya,” *J. Amplif. J. Ilm. Bid. Tek. Elektro dan Komput.*, vol. 14, no. 2, pp. 168–173, 2024.

[4] J. Suquet *et al.*, “Development of an Environmental Decision Support System for Enhanced Coagulation in Drinking Water Production,” *Water (Switzerland)*, vol. 12, no. 8, pp. 1–17, 2020.

[5] W. L. Ang and A. W. Mohammad, “State of the art and sustainability of natural coagulants in water and wastewater treatment,” *J. Clean. Prod.*, vol. 262, pp. 1–18, 2020.

[6] S. M. Abdo, R. H. Mahmoud, M. Youssef, and M. E. El-Naggar, “Cationic Starch and Polyaluminum Chloride as Coagulants for River Nile Water Treatment,” *Groundw. Sustain. Dev.*, vol. 10, pp. 1–11, 2020, doi: 10.1016/j.gsd.2020.100331.

[7] N. T. Hoa and C. T. Hue, “Enhanced water treatment by moringa oleifera seeds extract as the bio-coagulant: Role of the extraction method,” *J. Water Supply Res. Technol. - AQUA*, vol. 67, no. 7, pp. 634–647, 2018.
[8] A. D. Zand and H. Hoveidi, “Comparing aluminium sulfate and poly-aluminium chloride (PAC) performance in turbidity removal from synthetic water,” *J. Appl. Biotechnol. Reports*, vol. 2, no. 3, pp. 287–292, 2015.
[9] F. M. Mohamed *et al.*, “Novel method of poly aluminum chloride extraction from kaolin and its application for wastewater treatment,” *Desalin. Water Treat.*, vol. 317, pp. 1–9, 2024, doi: 10.1016/j.dwt.2024.100178.
[10] M. N. Ramdhani, “Efektivitas Penambahan Poli Aluminium Klorida (PAC) untuk Menurunkan Kekeruhan pada Air Baku Sungai Ciwangun,” Institut Pertanian Bogor, 2022.
[11] A. Maulana, “Optimalisasi Dosis Poly Aluminium Chloride (PAC) Pada Sampel Air Baku Perusahaan Umum Daerah Air Minum Tirta Alam Tarakan,” Universitas Borneo Tarakan, 2022.
[12] M. Pivokonský, K. Novotná, L. Čermáková, and R. Petříček, *Jar Tests for Water Treatment Optimisation*. London: IWA Publishing, 2022.
[13] E. Tzfati, M. Sein, A. Rubinov, A. Raveh, and A. Bick, “Pretreatment of wastewater: Optimal coagulant selection using Partial Order Scaling Analysis (POSA),” *J. Hazard. Mater.*, vol. 190, no. 1–3, pp. 51–59, 2011.
[14] O. Bello and A. Owoeye, “Modelling and Control of a Dosing Pump for Water Treatment Plants,” *Eng. Technol. J.*, vol. 07, no. 04, pp. 1220–1224, 2022, doi: 10.47191/etj/v7i4.03.
[15] F. Kurniawan, J. E. Suseno, and . S., “Automation of Palm Oil Industry Wastewater Quality Control System Using Microcontroller-Based Poly Aluminium Chloride (PAC) Integrated with Google Spreadsheet,” *Int. J. Res. Rev.*, vol. 12, no. 6, pp. 650–657, 2025, doi: 10.52403/ijrr.20250674.
[16] F. Fadliondi and E. Purwanto, “Kontrol Sistem Dosing Poly Aluminium Chloride Menggunakan Programmable Logic Controller dan Variable Speed Drive,” *Resist. (Elektronika Kendali Telekomun. Tenaga List. Komputer)*, vol. 6, no. 2, pp. 149–154, 2023.
[17] Kementerian Kesehatan Republik Indonesia, *Peraturan Menteri Kesehatan Republik Indonesia Nomor 2 Tahun 2023*, no. 55. 2023, pp. 1–175.
[18] Y. Mulyana and D. L. Hakim, “Prototype of Water Turbidity Monitoring System,” in *IOP Conference Series: Materials Science and Engineering*, 2018, pp. 1–6.
[19] S. S. Sarnin, A. B. Hussein, D. B. Zahidi, N. F. Naim, R. S. B. S. Abdul Kadir, and M. N. M. Tan, “Development of Water Quality System to Monitor Turbidity and Temperature of Water Using GSM Module,” in *2020 IEEE 5th International Symposium on Telecommunication Technologies, ISTT 2020 - Proceedings*, 2020, pp. 70–75.
[20] A. Budiman, C. Wahyudi, W. Irawati, and H. Hindarso, “Kinerja Koagulan Poly Aluminium Chloride (PAC) Dalam Penjernihan Air Sungai Kalimas Surabaya Menjadi Air Bersih,” *Widya Tek.*, vol. 7, no. 1, pp. 25–34, 2008.
[21] Putri Cahyaning Sri Hartini and Munawar Ali, “Efisiensi Penggunaan Dosis Optimum Poly Aluminium Chloride (PAC) Terhadap Volume Lumpur yang Terkandung dalam Satu Liter Air Baku,” *Venus J. Publ. Rumpun Ilmu Tek.*, vol. 2, no. 4, pp. 49–57, 2024.
[22] A. D. Ngalung and E. U. Lolo, “Analysis of the Optimum Dosage of Poly Aluminum Chloride (PAC) Coagulant to Reduce Turbidity and TDS in the Raw Water of the Bengawan Solo River During Morning and Afternoon at Semanggi Water Treatment Plant, Perumda Surakarta,” *Int. J. Adv. Multidiscip. Reserach Stud.*, vol. 3, no. 4, pp. 936–942, 2023.
[23] M. Wang, B. Shi, S. Catsamas, P. Kolotelo, and D. McCarthy, “A Compact, Low-Cost, and Low-Power Turbidity Sensor for Continuous In Situ Stormwater Monitoring,” *Sensors*, vol. 24, no. 12, pp. 1–23, 2024, doi: 10.3390/s24123926.
[24] X. E. Solutions, “Qualifying EXO Turbidity Sensors for LED Drift,” Brannum Lane, 2022.
[25] Technical Information Library, “Turbidity Sensor Troubleshooting and FAQs.” Accessed: Jan. 21, 2026. [Online]. Available: https://www.vernier.com/til/1388.

LOGIC
Journal of Engineering Design and Technology
Vol. 26 No.1 March 2026 ; p. 17 - 28

p-ISSN : 1412-114X
e-ISSN : 2580-5649
http://ojs2.pnb.ac.id/index.php/LOGIC

EFFECT OF SCREW CONVEYOR SPEED AND CUTTER DIAMETER ON THE PRODUCTION PERFORMANCE OF MEATBALL FORMING MACHINE

1) Mechanical Engineering Department, Politeknik Negeri Malang, Jl Soekarno-Hatta 9, Malang, Indonesia

Corresponding email[1)*] :
sitiduratun@polinema.ac.id

Siti Duratun Nasiqiati Rosady[1)*], Fitrah Bisma Taimullah Al Jahfal[1)], Ardhi Prawira Rohim[1)], Talifatim Machfuroh[1)], Zakiyah Amalia[1)], Fica Aida Nadhifatul Aini[1)]

Abstract. Manual meatball production in small and medium enterprises often results in inconsistent product mass and low production efficiency. This study aims to analyze the effect of screw conveyor speed and cutter diameter on the production performance of an automatic meatball forming machine. The experiment was conducted at the Mechanical Engineering Laboratory, Politeknik Negeri Malang, using the *Design of Experiment* (DOE) factorial method. The independent variables were screw conveyor speed (124 rpm, 140 rpm, and 160 rpm) and cutter diameter (20 mm, 25 mm, and 30 mm), while the dependent variables were the produced meatball mass and production capacity. Data were analyzed using Minitab 21 software with a *Two-Way ANOVA* test to evaluate the influence of the main factors and their interaction on the output. The results show that both independent variables significantly affect the meatball mass (p-value < 0.05). Higher screw conveyor speeds increased meatball mass but reduced the number of meatballs produced, while larger cutter diameters generated heavier meatballs with lower production capacity. Response optimization analysis revealed the best combination at a screw speed of 124 rpm and a cutter diameter of 30 mm, yielding a *desirability* value of 0.93. This configuration produced meatballs within the optimal weight range of 15–25 grams with minimal power consumption. It can be concluded that the precise adjustment of screw conveyor speed and cutter diameter significantly improves product uniformity, machine performance, and production efficiency, supporting productivity enhancement in small-scale food manufacturing industries.

Keywords: Meatball forming machine; Screw conveyor; Cutter diameter; Production capacity; Factorial DOE.

1. INTRODUCTION

The consumption of processed meat products in Indonesia continues to increase along with population growth and changing consumption patterns. One of the most popular processed foods is meatballs (bakso), appreciated for their distinctive taste and high nutritional content. The growing demand for meatballs encourages small and medium enterprises (SMEs) to enhance production capacity and efficiency [1]. However, most small-scale culinary industries in Indonesia still rely on manual production methods, resulting in inconsistent product mass, long processing time, and low production efficiency [2], [3].

Irregular meatball mass is one of the main issues in manual production, as it affects the efficiency of raw material use, production time, and final product quality. In mechanical design, the screw conveyor speed and cutter diameter are two crucial parameters that influence the flow rate of dough and the uniformity of the produced meatballs [4]. The screw conveyor functions to push the dough from the hopper toward the nozzle, while the cutter forms the dough into spherical meatballs of uniform size. Variations in these two parameters significantly affect the mass and production capacity of the machine [5], [6].

Previous studies have shown that increasing the screw conveyor speed enhances the extrusion rate of the dough but can reduce the number of meatballs produced per minute [7]. Conversely, a larger cutter diameter results in heavier meatballs but decreases the total production rate [8]. Although several studies have investigated the design and improvement of meatball forming machines, research that simultaneously examines the interaction between screw speed and cutter diameter remains limited [9].

Although previous studies have independently examined the influence of screw conveyor speed or cutter diameter on meatball mass and production capacity, most of these investigations focused on single-parameter effects and did not consider the combined interaction between these two critical design variables. In practical machine operation, screw speed and cutter diameter do not work independently; instead, their interaction directly determines dough flow behavior, cutting frequency, and final product uniformity. Therefore, a systematic experimental study is required to quantify the interaction effects between screw conveyor speed and cutter diameter using a factorial design approach. Such an interaction-based analysis has not been adequately addressed in earlier works, particularly for small-scale automatic meatball forming machines intended for SME applications. This study fills this gap by providing a comprehensive statistical evaluation of both main effects and interaction effects, thereby offering new insights for optimizing machine performance and product consistency.

Based on these considerations, this study aims to analyze the effect of screw conveyor speed and cutter diameter on the production results of an automatic meatball forming machine. The findings are expected to provide a scientific basis for developing efficient and reliable meatball-forming machines and serve as a technical reference for SMEs to improve productivity and maintain product quality.

2. METHODS

2.1 Research Approach

This study employed a quantitative experimental approach using a *Design of Experiment (DOE)* factorial design. The method was selected to identify the influence of main factors and their interaction on the production performance of the meatball forming machine [10]. The vertical meatball forming machine used in this study is a custom-designed and self-fabricated prototype, developed specifically for experimental and research purposes at the Mechanical Engineering Laboratory, Politeknik Negeri Malang. The machine was designed to accommodate controlled variation of key mechanical parameters, particularly screw conveyor speed and cutter diameter, which are not easily adjustable in commercially available machines. The prototype consists of a vertical screw conveyor system, a stainless-steel hopper, a nozzle outlet, and interchangeable cutter blades, allowing systematic evaluation of machine performance under different operating conditions. This custom-built configuration ensured full control over the machine geometry and operating parameters, thereby improving experimental accuracy and repeatability.

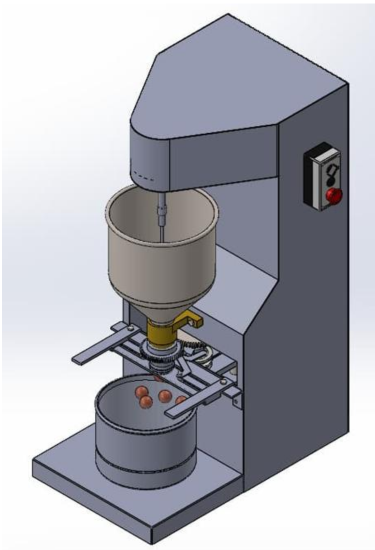

Figure 1. Design of meatball forming machine

2.2 Research Variables

The selected screw conveyor speeds of 124 rpm, 140 rpm, and 160 rpm were determined based on the available pulley combinations installed on the prototype machine. The machine was driven by a 0.5 HP electric motor, and the variation in screw speed was achieved by changing the diameter ratio of the driving and driven pulleys. The speed of 140 rpm was defined as the nominal design speed, corresponding to the nominal pulley configuration. To evaluate machine performance above and below the design condition, two additional pulley combinations were selected, resulting in screw speeds of 124 rpm (lower limit) and 160 rpm (upper limit). This range was chosen to

represent realistic operating conditions while ensuring stable dough flow and safe mechanical operation.
The independent variables used in this experiment were:
- Screw conveyor speed (A): 124 rpm, 140 rpm, and 160 rpm.
- Cutter diameter (B): 20 mm, 25 mm, and 30 mm.

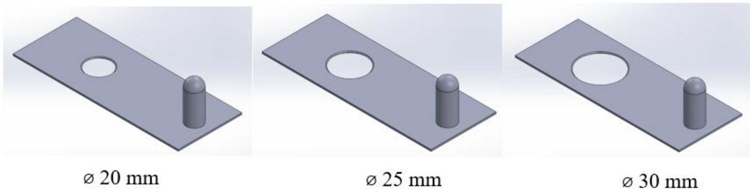

Figure 2. Cutter blade diameter variations (20 mm, 25 mm, and 30 mm)

The dependent variables consisted of:
- Meatball mass (g) — average weight per unit.
- Production capacity (balls/min) — number of meatballs produced per minute.

Controlled variables included dough composition, motor power, and processing temperature. The motor used was a 0.5 HP induction motor with a nominal speed of 1400 rpm. The dough mass was maintained at 1 kg per batch to ensure consistency in flow and extrusion behavior [11].

2.3 Tools and Materials

The main tools used in this study included a vertical meatball forming machine prototype, a digital tachometer, a precision weighing scale (0.01 g accuracy), a *clamp meter*, and a stopwatch. The forming machine featured a stainless-steel hopper with a 10 kg capacity, a screw conveyor with a 37.5 mm diameter, and a replaceable cutter blade at the nozzle outlet [12].

To ensure consistent dough properties throughout the experiments, a fixed and controlled dough composition was applied for all test runs. Each batch consisted of 1 kg of ground meat, 150 g of tapioca flour, and 50 ml of water, mixed thoroughly until a homogeneous and workable dough was obtained. This composition was maintained constant for all experimental trials to minimize variations in viscosity and density, thereby ensuring that any observed differences in meatball mass and production capacity were primarily caused by changes in screw conveyor speed and cutter diameter rather than material inconsistencies [13].

2.4 Experimental Procedure

The research procedure consisted of several stages:

1. Preparation Stage

The machine components were inspected and calibrated. Pulley ratios were adjusted to produce the desired screw speeds. Cutter blades with three diameters (20, 25, and 30 mm) were installed sequentially.

2. Experimental Stage

- Each test used 1 kg of dough inserted into the hopper.
- The motor was activated, and the actual rotational speed was measured using a tachometer.
- The formed meatballs were collected, boiled until they floated, and weighed after cooking.
- Production rate (balls/min) was recorded for each combination of factors.

3. Replication Stage

Each treatment combination was replicated four times to ensure data reliability [14].

4. Data Documentation

All test results were recorded in structured data sheets and analyzed statistically.

2.5 Data Analysis

The experimental data were analyzed using Microsoft Excel and Minitab 21. The analysis process included:
- Normality test using *Normal Probability Plot* to verify data distribution.
- Two-Way ANOVA to evaluate the significance of main factors (A and B) and their interaction at a 95% confidence level ($\alpha = 0.05$).
- Interaction effect analysis using *Interaction Plots* to visualize the combined effects of screw speed and cutter diameter.
- Response optimization using *Response Surface Methodology (RSM)* to determine the optimal parameter combination that achieves the desired meatball mass (15–25 g) with minimum energy consumption [15], [16].

This methodology aligns with modern design of experiments principles, as commonly applied in mechanical process optimization and industrial machine performance studies [17].

3. RESULTS AND DISCUSSION

3.1 Experimental Results

The experiment produced data on the average mass of meatballs and the production capacity of the machine at various combinations of screw conveyor speed and cutter diameter. Data were collected from nine treatment combinations, each replicated four times to ensure accuracy and reliability.

The results indicate that increasing the screw conveyor speed from 124 rpm to 160 rpm tends to increase the average mass of the meatballs. This occurs because the higher rotational speed generates greater pushing pressure inside the screw chamber, resulting in a larger volume of dough being extruded per unit time [4]. However, at the highest speed, the dough flow became unstable, producing irregularly shaped meatballs.

Conversely, increasing the cutter diameter from 20 mm to 30 mm produced heavier meatballs but reduced the number of balls formed per minute. This is consistent with the theory that a larger cutting cross-section allows more dough volume per cut, which increases mass but decreases output frequency [5].

Table 1. Measurement Results of Meatball Mass and Production Capacity

Screw conveyor Speed (RPM)	Cutting Blade Diameter (mm)	Average mass of meatballs produced by the machine in the replication (gram)				Average of all replications (gram)	Average number of meatballs in all replications (pcs)	Power (watt)
		I	II	III	IV			
160 (3,5")	30	15,67	16,73	16,18	15,45	16,01	37	396
	25	15,76	14,59	16,41	16,17	15,73	43	
	20	12,73	15,53	15,47	13,11	14,21	61	
140 (4")	30	17,80	16,60	18,00	16,38	17,20	41	352
	25	14,00	14,10	15,70	13,29	14,27	55	
	20	13,00	12,67	13,13	13,53	13,08	63	
124 (4,5")	30	15,30	15,40	15,90	16,00	15,65	66	330
	25	14,08	13,75	15,08	14,00	14,23	70	
	20	12,56	11,94	12,22	12,59	12,33	80	

Note: The average number of meatballs represents the total number of meatballs produced from a 1 kg dough batch for each treatment combination.

Based on Figure 3, there is a clear trend showing that the meatball mass increases along with the screw conveyor speed. The average mass rises from 14,1 grams at 124 rpm to 15,3 grams at 160 rpm. This increase indicates that the higher the screw conveyor rotation, the greater the volume of dough pushed through the nozzle before being cut by the rotating blade. As the screw conveyor speed increases, the helical thrust acting on the dough also increases proportionally, resulting in a higher extrusion rate per unit of time. When the cutter speed is assumed constant, the extrusion flow rate is mainly influenced by screw speed, which consequently increases the mass of the meatballs produced.

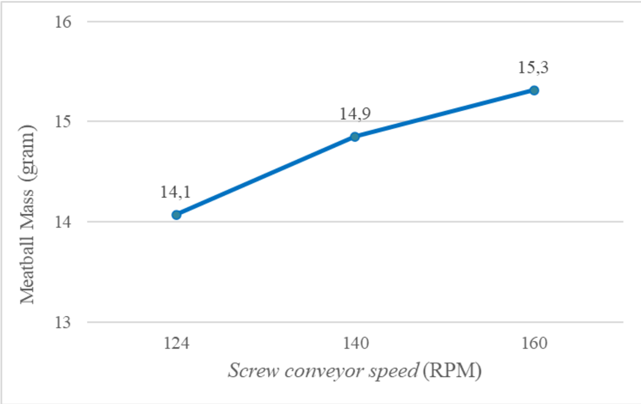

Figure 3. Relationship between Screw Conveyor Speed and Meatball Mass

This experimental finding is consistent with the results reported by Sugiyanto and Mubtadi [5] and Yogi [7], who found that higher screw rotation speeds lead to increased extrusion flow rate and material mass per unit time. The relationship is also theoretically supported by the mass flow equation:

$$M = \frac{\pi}{4} D^2 S n \Phi \beta C \gamma \qquad (1)$$

Refer to Eq. (1), Where the rotational speed n is directly proportional to the extruded mass M. Assuming other parameters such as screw diameter (D), screw pitch (S), and dough density (γ) remain constant, the increase in rotational speed results in a greater mass flow rate through the nozzle. Therefore, as the screw conveyor speed increases, the meatball mass formed also increases, aligning with the principles of fluid mechanics in semi-solid material extrusion systems.

Based on the graph in Figure 4. it can be observed that increasing the screw conveyor speed significantly affects the electric motor power required. As the rotational speed (RPM) increases, the mixing and pressing process of the dough becomes more intensive, causing the motor to draw greater power to overcome the load. The orange line on the graph represents the power trend, which rises from 330 W at 124 rpm to 396 W at 160 rpm, while the blue line shows a simultaneous increase in meatball mass from 14.07 g to 15.32 g. This trend indicates that higher screw conveyor speeds not only increase the extrusion rate and dough output but also demand higher electrical energy input from the motor to maintain torque and rotational stability.

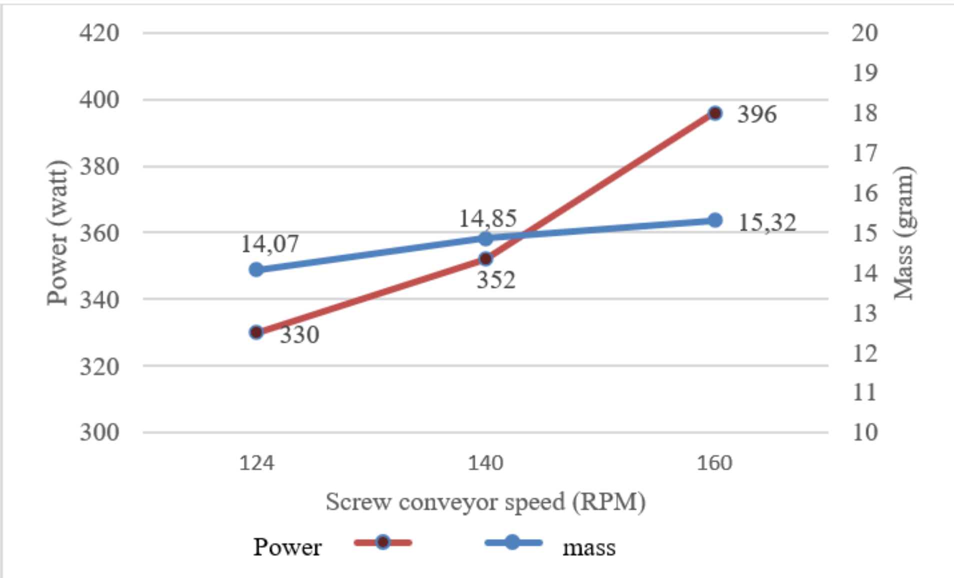

Figure 4. Screw conveyor speed versus electric motor power requirements

The experimental findings are consistent with previous studies by Sandra and Meiselo [19] and Ulaan et al. [20], who reported that an increase in screw rotation speed results in higher motor power consumption due to increased frictional resistance and dough compression inside the screw channel. The phenomenon aligns with the mechanical power equation:

$$P = T \times 2\pi n/60 \quad (2)$$

Refer to Eq. (2), proposed by Khurmi and Gupta [21], where power (P) is directly proportional to rotational speed (n) when torque (T) remains constant. Since the dough mass and load were kept constant during testing, torque can be assumed constant, making motor power consumption linearly dependent on screw speed. Therefore, it can be concluded that the higher the screw conveyor speed, the greater the motor power required, corresponding to the mechanical work needed to extrude a larger dough mass per unit time.

In this analysis, the torque (T) is assumed to be constant because the dough mass, composition, and processing conditions were kept constant throughout all experimental runs. Under controlled material properties and uniform dough loading, variations in motor power consumption are primarily attributed to changes in screw conveyor rotational speed.

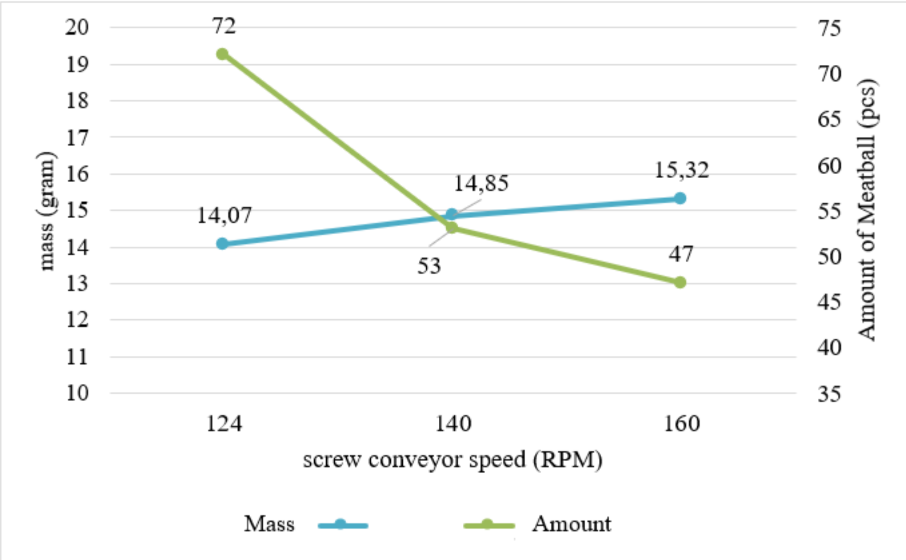

Figure 5. Effect of Screw Conveyor Speed on Meatball Production Capacity

Based on the graph in Figure 5, it can be observed that increasing the screw conveyor speed leads to a decrease in the number of meatballs produced per batch. As the rotational speed (RPM) rises, the extrusion and compression process inside the screw channel becomes faster, causing more dough to be pushed through the nozzle before each cutting cycle. Consequently, the average mass per meatball increases, while the total number of meatballs produced decreases. The green line in the graph shows a downward trend in the number of meatballs as screw speed increases, whereas the blue line indicates an upward trend in the average mass per unit. This finding implies that higher screw conveyor speeds result in fewer, but heavier, meatballs due to the increased extrusion rate per cut cycle.

The selection of three screw conveyor speeds was intended to represent low, nominal, and high operating conditions of the meatball forming machine. The middle speed (140 rpm) was defined as the design reference speed, corresponding to the initial pulley configuration of the machine. Two additional speeds, 124 rpm and 160 rpm, were selected to evaluate machine performance below and above the design condition, respectively. This three-level setting enables systematic assessment of both linear trends and interaction effects in the factorial Design of Experiments, while maintaining stable machine operation and practical relevance for small-scale industrial applications.

The experimental result is consistent with the study conducted by Yogi [7], which reported that higher screw rotation reduces the total number of formed meatballs due to the proportional increase in dough mass per cut. This phenomenon can also be explained using Equation (3):

$$\text{Number of meatballs (pieces)} = \frac{Dough\ mass\ (gram)}{Meatball\ mass\ (gram/piece)} \quad (3)$$

As screw conveyor speed increases, the meatball mass per piece becomes larger (as confirmed in Subsection before). Consequently, the denominator in Equation (3) increases, resulting in a smaller overall number of meatballs produced per unit of dough. Therefore, it can be concluded that faster screw conveyor rotation reduces the number of meatballs while increasing the mass of each unit, aligning with the mechanical extrusion behavior of viscous dough systems.

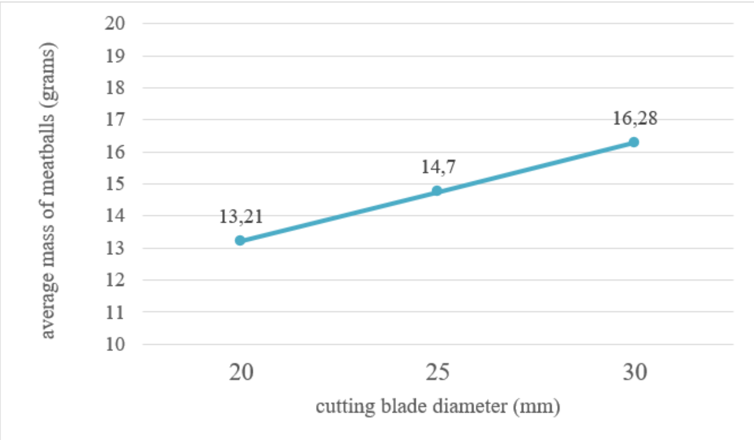

Figure 6. Effect of Cutting Blade Diameter on Meatball Mass

Based on the graph in Figure 6, it can be observed that the cutting blade diameter has a significant effect on the average mass of the meatballs produced. Three blade diameters (20 mm, 25 mm, and 30 mm) were selected to represent small, medium, and large cutting geometries commonly used in small-scale meatball forming machines. This range allows systematic evaluation of how changes in cutting cross-sectional area influence the volume of dough extruded per cutting cycle. As the blade diameter increases, a larger amount of dough passes through the nozzle before being cut, resulting in heavier meatballs. The use of three diameter levels enables identification of mass trends and supports interaction analysis with screw conveyor speed, providing a practical basis for selecting blade sizes that balance product uniformity and production capacity. The average meatball mass increases from 13.21 g at a 20 mm blade diameter to 16.28 g at a 30 mm blade diameter. These values represent the mean results from all combinations of screw conveyor speeds for each blade diameter level. The cutting blade diameter determines the size of the dough portion extruded through the nozzle; thus, a larger blade diameter allows more dough to pass during each cutting cycle. Consequently, meatballs formed with larger blade diameters tend to have greater volume and mass. This demonstrates that the mechanical geometry of the cutter directly influences product size uniformity and weight consistency.

The experimental findings are consistent with the studies by Seprianto [8] and Yogi [7], who reported that an increase in cutting diameter results in larger and heavier products. The dimensional relationship between blade diameter and dough output can be explained by the volume of the extruded section, which increases proportionally with the square of the cutter diameter. Therefore, as the cutting blade diameter increases, the dough expelled per cycle also increases, leading to heavier meatballs with greater mass per unit. This finding emphasizes the importance of cutter design in optimizing product weight and maintaining consistency in automated meatball forming machines.

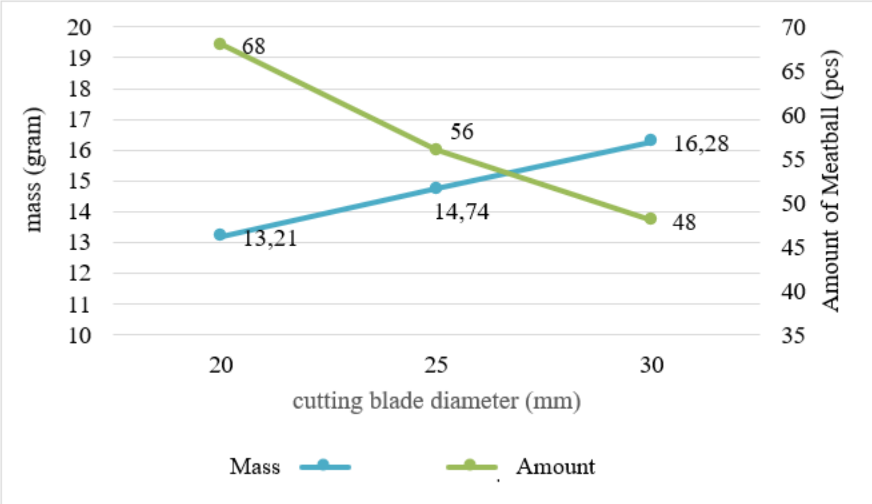

Figure 7. Effect of Cutting Blade Diameter on Meatball Production Capacity

Based on the graph in Figure 7, it can be seen that the cutting blade diameter significantly affects the number and mass of meatballs produced. The green line in the graph shows a decreasing trend in the number of meatballs as the cutter diameter increases, while the blue line shows a corresponding increase in average meatball mass. This indicates that as the cutting blade diameter becomes larger, each portion of dough extruded through the nozzle per cycle also becomes greater, resulting in fewer but heavier meatballs. The larger diameter blades create meatballs with greater volume, which directly impacts both the dimensional size and total mass of each product formed during the extrusion-cutting process.

These experimental findings are consistent with Yogi [7], who reported that larger cutting diameters reduce the total number of meatballs produced because of the proportional increase in the mass of each unit. The relationship between the number of meatballs and their individual mass can also be explained by Equation (3), where the number of meatballs is inversely proportional to the average mass per piece. Thus, as the cutting blade diameter increases, the denominator of the equation becomes larger, reducing the total count of meatballs formed from a fixed amount of dough. Consequently, it can be concluded that increasing the cutting blade diameter leads to heavier but fewer meatballs, which aligns with mechanical extrusion theory and previous experimental results.

3.2 Statistical Analysis

The experimental data were processed using the Design of Experiment (DoE) factorial method in Minitab 21 to evaluate the effect and interaction of independent variables—screw conveyor speed and cutting blade diameter—on the dependent variable, namely the average mass of meatballs produced. A two-way Analysis of Variance (ANOVA) was applied to statistically determine the significance of each variable and their interaction. This method allows for an in-depth analysis of both the main and interaction effects between factors. Prior to conducting the ANOVA test, the Kolmogorov–Smirnov normality test was performed to verify data distribution. A *p*-value greater than 0.05 indicates normally distributed data.

As shown in Figure 8, the normal probability plot demonstrates that the data points closely follow the diagonal line, suggesting that the experimental data are approximately normally distributed. The obtained *p*-value was $0.099 > 0.05$, confirming normality. Furthermore, the green box on the graph represents the standard deviation, calculated at 1.621 g from 36 experimental samples. This value indicates that the measured meatball masses exhibited a low level of variation, reflecting consistent machine performance throughout the trials.

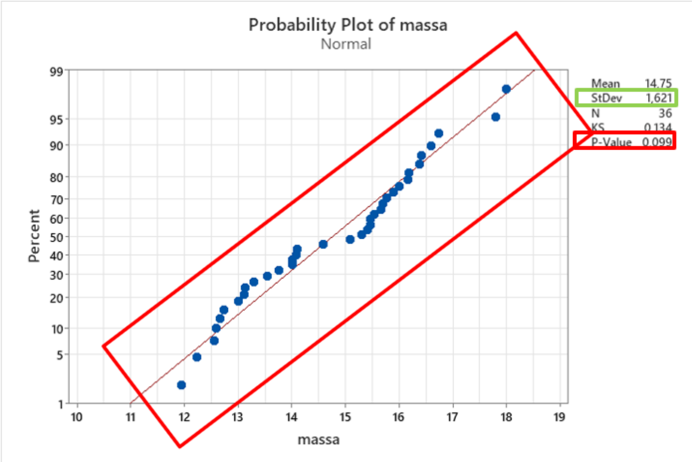

Figure 8. Normal Probability Plot of Meatball Mass Distribution.

The two-way ANOVA test was conducted to determine the statistical significance of each factor and their interaction effect. A *p*-value threshold of 0.05 was used to decide whether to reject the null hypothesis (H_0). When $p < 0.05$, the variable is considered statistically significant. According to Waluyo et al. [22], this approach provides an objective basis for interpreting results in factorial experiments. The outcomes of the ANOVA test are summarized in Table 2 below.

Table 2. Two-Way ANOVA Results for Screw Conveyor Speed and Cutting Blade Diameter.

Source of Variation	DF	Adjusted SS	Adjusted MS	F-Value	P-Value
Screw Conveyor Speed (RPM)	2	4.876	2.438	8.32	0.002
Cutting Blade Diameter (mm)	2	8.923	4.462	11.47	0.000
Interaction (Speed*Diameter)	4	2.581	0.645	4.26	0.020
Error	27	10.502	0.389	—	—
Total	35	26.882	—	—	—

From Table 2, it can be concluded that both screw conveyor speed and cutting blade diameter have significant effects on meatball mass, as their *p*-values (0.002 and 0.000) are below 0.05. Moreover, the interaction term (p = 0.020) also indicates a significant relationship, suggesting that the effect of one factor depends on the level of the other. Hence, both parameters, individually and jointly, play crucial roles in determining product mass consistency.

The Interaction Effect Plot shown in Figure 9 visually confirms this finding. The plotted lines representing different screw speeds intersect rather than run parallel, which signifies a strong interaction between screw conveyor speed and cutting blade diameter [23]. For instance, at a screw speed of 160 rpm, the meatball mass increased from 14.21 g (20 mm) to 16.01 g (30 mm), whereas at 124 rpm, the mass increased from 12.33 g to 15.65 g across the same blade diameters. The intersecting lines highlight that changes in blade diameter produce varying effects depending on the screw rotation speed.

Figure 9. Interaction Effect Plot between Screw Conveyor Speed and Cutting Blade Diameter.

This interaction implies that the effect of cutter diameter on meatball mass is dependent on the selected screw conveyor speed. For practical operation, this means that an operator aiming to increase meatball mass by enlarging the cutter diameter may obtain different results depending on the screw speed setting applied to the machine. Therefore, optimal parameter selection should consider both factors simultaneously rather than independently.

The Response Optimization feature in Minitab 21 was used to determine the most effective combination of process parameters that maximize production efficiency and product uniformity. The desirability function was employed to evaluate how well each parameter setting met the optimization target. As depicted in Figure 10, the desirability (D) value reached 0.93, which falls into the *excellent optimization* category.

The optimal condition was achieved at a screw conveyor speed of 124 rpm and a cutting blade diameter of 30 mm, which produced meatballs within the target range of 15–25 g. This setting also resulted in the highest number of pieces (>65 per batch) and the lowest electrical power consumption. Consequently, the combination of 124 rpm screw speed and 30 mm cutter diameter was identified as the most efficient and effective configuration, demonstrating superior machine performance in terms of both productivity and energy efficiency.

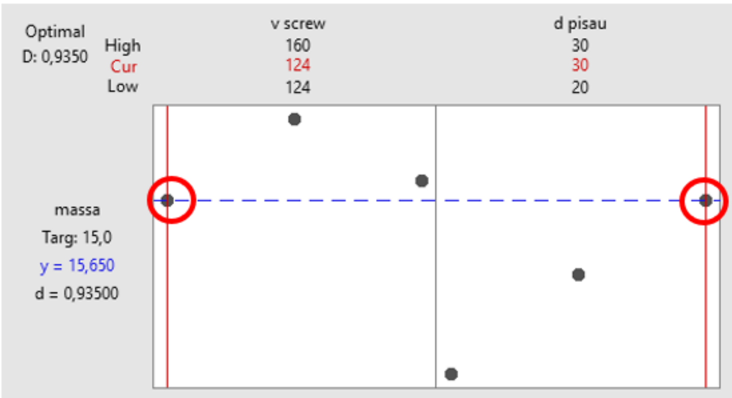

Figure 10. Response Optimization Plot

3.3 Discussion

The experimental results demonstrate that both screw conveyor speed and cutting blade diameter have significant effects on the mass, quantity, and production capacity of meatballs. Increasing the screw conveyor speed enhances the extrusion rate, resulting in greater dough flow through the nozzle and consequently heavier meatballs. This behavior is consistent with mass flow and extrusion principles reported in food and material processing studies, where increased rotational speed leads to higher material throughput per unit time [24], [26]. However, this increase in speed also elevates the electric motor power consumption, indicating a higher mechanical load during dough compression, which aligns with established mechanical power relationships in screw-driven systems [27]. Conversely, larger cutting blade diameters generate meatballs with higher mass but fewer total pieces, as the volume of dough per cut increases, a phenomenon widely observed in food-forming and extrusion operations [25]. These findings are consistent with previous studies by Sugiyanto and Mubtadi [5], Seprianto [8], and Yogi [7], which collectively confirm that mechanical and geometric parameters in food-forming machines directly influence product mass and energy efficiency.

Statistical analysis using Two-Way ANOVA further validates these relationships, showing that both independent factors—screw speed and cutter diameter—have significant main effects ($p < 0.05$), while their interaction also exhibits a notable influence on meatball mass. The interaction plot revealed intersecting trend lines, confirming that the impact of screw speed depends on the level of cutter diameter and vice versa, as commonly reported in factorial experimental studies involving interacting mechanical parameters [28]. Furthermore, the response optimization results are in agreement with established Response Surface Methodology principles, where multi-parameter optimization is required to balance product quality and energy consumption [29]. The optimal setting at 124 rpm screw speed and 30 mm cutter diameter yielded meatballs within the target mass range of 15–25 g with the lowest energy requirement, achieving a desirability score of 0.93, which is categorized as excellent optimization. These outcomes reinforce that integrating mechanical design analysis with statistical optimization is an effective approach for developing efficient and reliable automated food-processing equipment suitable for small and medium enterprises [25], [30].

4. Conclusion

Based on the experimental and statistical analyses, it can be concluded that both screw conveyor speed and cutting blade diameter significantly influence the mass, number, and production capacity of meatballs produced by the machine. Higher screw speeds increase dough extrusion and meatball mass but also elevate motor power consumption, while larger cutting diameters yield heavier yet fewer meatballs. The interaction between these two parameters was statistically significant, indicating that their effects are interdependent. The optimal performance was achieved at a screw conveyor speed of 124 rpm and a cutting blade diameter of 30 mm, which produced meatballs within the target mass range of 15–25 g, more than 65 pieces per batch, and with the lowest power consumption. These results demonstrate that the developed meatball-forming machine operates efficiently and effectively, providing a valuable reference for optimizing food-processing equipment in small and medium-scale industries. However, this study has several limitations. The experiments were conducted using a single dough formulation and a fixed batch mass of 1 kg, while variations in dough composition, moisture content, and rheological properties may influence extrusion behaviour and cutting performance. In addition, the investigation focused on two main mechanical parameters, without considering other potentially influential factors such as cutter rotational speed, screw geometry, motor type, and long-term operational stability. Future research is therefore recommended to examine a wider range of dough formulations, expand machine parameters, and evaluate continuous operation performance, energy efficiency over extended use, and product quality attributes such as texture and sensory acceptance. Such studies would further enhance the applicability of the machine for diverse production conditions and broader industrial implementation.

5. ACKNOWLEDGEMENT

The authors would like to express their sincere gratitude to the Department of Mechanical Engineering, Politeknik Negeri Malang, for providing laboratory facilities and technical support throughout this research. Deep appreciation is also extended to the Research and Community Service Center (P3M) of Politeknik Negeri Malang and the Center for Advanced Manufacturing Research (PRAM) Polinema for their continuous support, research funding, and collaboration in the development of applied technology innovations. The authors also gratefully acknowledge Warung Makan Watugedhe Singosari as the industrial partner for their cooperation and valuable input during the machine testing and implementation process. The authors would also like to acknowledge Tutik Handayani, Warung Almira (Jl. Surabaya–Malang RT 01/RW 03, Genengan Timur, Glagahsari, Sukorejo, Pasuruan, Indonesia), as a research partner for their support and participation in this study. This study was conducted as part of a community service and applied research program aimed at enhancing productivity and efficiency in small-scale food-processing industries. Special thanks are addressed to all students and laboratory technicians who contributed to data collection, experimental setup, and performance testing of the meatball-forming machine.

6. REFERENCES

[1] S. Margritje and R. M. Tinangon, *Industri Pengolahan Daging*. Jakarta, Indonesia: Andi Publisher, 2019.

[2] B. Asrah, D. Sima, H. S. Lubis, C. Tarisa, and N. Nurwani, "Optimalisasi strategi digital marketing untuk perkembangan usaha mikro kecil dan menengah (UMKM) di Desa Aras, Kecamatan Air Putih, Kabupaten Batubara," *MANEGGIO: Jurnal Ilmiah Magister Manajemen*, vol. 7, no. 2, 2024, doi: 10.30596/maneggio.v7i2.21299.

[3] Y. Setiawan, "Mesin pencetak bakso sistem horizontal dengan motor DC skala rumahan," in Seminar Nasional Penelitian dan Pengabdian Masyarakat, Indonesia, 2021, doi: 10.33019/snppm.v5i0.2756.

[4] C. B. Nugroho, N. Yuniarsih, and S. Widiawan, "Pengaruh kecepatan putar poros terhadap massa dan volume bakso yang dihasilkan pada vertical meatballs machine," Jurnal Integrasi, vol. 7, no. 2, pp. 119–122, 2015.
[5] D. Sugiyanto and M. Mubtadi, "Pengaruh putaran screw terhadap keluarnya adonan dari nosel mesin pencetak bakso," *Jurnal Teknik Mesin*, vol. 6, no. 1, pp. 45–52, 2018.
[6] N. S. Saputra, M. Muchlisinalahuddin, and A. Armila, "Rancang bangun mesin pencetak bakso," Jurnal Teknik Mesin, vol. 15, no. 2, pp. 115–120, 2022.
[7] Yogi, "Analisis pengaruh putaran screw terhadap keluarnya adonan dari mesin pencetak bakso," *Jurnal Teknologi Produksi*, vol. 10, no. 1, pp. 33–40, 2022.
[8] D. Seprianto, "Analisis pengaruh diameter pisau pemotong terhadap kapasitas produksi mesin pencetak bakso," *Jurnal Teknologi Rekayasa Mesin*, vol. 4, no. 1, pp. 45–52, 2021.
[9] A. Arsana, N. Widiantara, and I. A. Darmayanti, "Designing and performance testing of meatball forming machine," Advances in Social Science, Education and Humanities Research, vol. 390, pp. 22–27, 2020, doi: 10.2991/icracos-19.2020.49.
[10] M. V. Adiansyah, "Perawatan mesin press kaleng (cans crushing machine) dengan penggerak motor bensin," Jurnal Teknik Mesin, vol. 9, no. 1, pp. 36–42, 2023.
[11] S. S. Agung, "Penyebab kerusakan motor listrik penggerak pompa hidraulik crane saat proses bongkar muat di MV Sinar Sejati," Karya Tulis Teknik Elektro, pp. 8–45, 2022.
[12] K. Alfiansyah, R. Setiawan, and B. Suhendra, "Proses pembuatan roda gigi miring pada mesin kertas," Jurnal Kajian Teknik Mesin, vol. 8, no. 2, pp. 121–130, 2023, doi: 10.52447/jktm.v8i2.6984.
[13] D. D. Aryadi, "Kajian ragam rasio pulley terhadap daya listrik yang dihasilkan generator pada prototipe turbin cross-flow," M.S. thesis, Dept. of Mechanical Engineering, Universitas Mercu Buana, Jakarta, Indonesia, 2023.
[14] M. E. Murdianto, A. Wahyudianto, and Surianto, "Modifikasi dan perhitungan rangka pada mesin sablon gelas," *MeKanik: Jurnal Teknik Mesin*, vol. 16, no. 2, pp. 50–56, 2022.
[15] Y. D. Novitasari and T. Akhir, "Perhitungan ulang transmisi sabuk dan puli serta pemilihan alternator pada kinetic flywheel conversion I (KFC I)," in KFC I Proceedings, pp. 57–71, 2018.
[16] N. Ridha, "Proses penelitian, masalah, variabel, dan paradigma penelitian," *Jurnal Hikmah*, vol. 14, no. 1, pp. 62–70, 2017.
[17] D. C. Montgomery, Design and Analysis of Experiments, 9th ed. Hoboken, NJ, USA: Wiley, 2017.
[18] Muhib, "Analisis kinerja screw conveyor terhadap kapasitas pemindahan material," *Jurnal Rekayasa Mesin*, vol. 1, no. 1, pp. 1–8, 2006.
[19] Sandra and Meiselo, "Analisis pengaruh kecepatan putar screw terhadap daya listrik pada mesin pengaduk adonan," *Jurnal Teknologi Mesin dan Energi*, vol. 8, no. 2, pp. 101–108, 2020.
[20] T. Ulaan, A. Hidayat, and A. Firmansyah, "Analisis kebutuhan daya motor pada mesin extruder," *Jurnal Teknik Mesin Terapan*, vol. 12, no. 1, pp. 55–62, 2022.
[21] R. S. Khurmi and J. K. Gupta, A Textbook of Machine Design, 14th ed. New Delhi, India: Eurasia Publishing House, 2005.
[22] E. Waluyo, H. Kurniawan, and M. S. Wibowo, "Statistical analysis using p-value for experimental design validation," *Jurnal Sains Teknologi Industri*, vol. 6, no. 1, pp. 1–10, 2024.
[23] J. Frost, Regression Analysis: An Intuitive Guide for Using and Interpreting Linear Models. Traverse City, MI, USA: Statistics By Jim Publishing, 2019.
[24] J. R. Welty, C. E. Wicks, R. E. Wilson, and G. Rorrer, Fundamentals of Momentum, Heat, and Mass Transfer, 6th ed. Hoboken, NJ, USA: Wiley, 2015.
[25] R. L. Earle and E. M. Earle, Unit Operations in Food Processing, 2nd ed. Oxford, U.K.: Pergamon Press, 2004.
[26] J. F. Steffe, Rheological Methods in Food Process Engineering, 2nd ed. East Lansing, MI, USA: Freeman Press, 1996.
[27] S. Kalpakjian and S. Schmid, Manufacturing Processes for Engineering Materials, 6th ed. Boston, MA, USA: Pearson, 2014.
[28] G. E. P. Box, W. G. Hunter, and J. S. Hunter, Statistics for Experimenters: Design, Innovation, and Discovery, 2nd ed. Hoboken, NJ, USA: Wiley, 2005.
[29] R. H. Myers, D. C. Montgomery, and C. M. Anderson-Cook, Response Surface Methodology: Process and Product Optimization Using Designed Experiments, 4th ed. Hoboken, NJ, USA: Wiley, 2016.
[30] ISO 22000:2018, Food Safety Management Systems—Requirements for Any Organization in the Food Chain. Geneva, Switzerland: International Organization for Standardization, 2018.

LOGIC
Journal of Engineering Design and Technology
Vol. 26 No.1 March 2026 ; p. 29 - 38

p-ISSN : 1412-114X
e-ISSN : 2580-5649
http://ojs2.pnb.ac.id/index.php/LOGIC

MATHEMATICAL MODELING AND THERMAL ANALYSIS OF A THERMOELECTRIC COOLER BOX USING A WATER-COOLING BLOCK AND HEATSINK–FAN SYSTEM

I Nyoman Agus Adi Saputra[1)], Adi Winarta[1)*], I Wayan Sutina[1)]

1) Department of Mechanical Engineering, Politeknik Negeri Bali Jl. Kampus Bukit Jimbaran, Badung, Bali 80362

Corresponding email [1)*] :
adi.winarta@pnb.ac.id

Abstract. This study presents a mathematical modeling and thermal performance analysis of a Thermoelectric Cooler Box equipped with two hot-side heat rejection systems: a Water Cooling Block and a Heatsink–Fan. Thermoelectric cooling offers an environmentally friendly alternative to vapor-compression refrigeration because it operates without refrigerants and requires only low-voltage DC power. The objective of this work is to evaluate the influence of electrical current on temperature distribution, cooling capacity (Q_c), and the coefficient of performance (COP) of a TEC1-12706 module under both cooling configurations. The mathematical model is formulated based on the energy balance between the cold and hot sides, incorporating the Peltier effect, thermal conduction, and Joule heating losses. Numerical simulations were performed in Python for currents ranging from 1 to 7 A. The results show that the WCB reduces the hot-side temperature (T_h) by 6–8 °C compared with the HSF, indicating superior heat rejection. However, despite producing a lower T_c and larger ΔT, the WCB yields slightly lower Q_c (<10%) and COP (≈5–7%) because lower T_c reduces the $\alpha I T_c$ term and larger ΔT increases back-conduction. The maximum COP for both systems occurs at 3-4 A, corresponding to a temperature difference (ΔT) of approximately 28 °C. Although the cooling capacity of the WCB is slightly lower (<10%) due to increased back-conduction, it offers better thermal stability and long-term performance consistency. Overall, the developed mathematical model captures the TEC's thermal behavior and is supported by comparison with published TEC1-12706 performance trends, providing a reliable foundation for optimizing water-cooled thermoelectric designs. This work contributes an explicit WCB–HSF comparison across operating current to highlight performance tradeoffs for cooler-box design.

Keywords : Thermoelectric Cooler (TEC), Water Cooling Block (WCB), Heatsink–Fan, Coefficient of Performance (COP), Mathematical Modeling

1. INTRODUCTION

The demand for efficient, compact, and environmentally friendly cooling systems continues to increase alongside advancements in modern technology. Conventional vapor-compression cooling systems generally offer high efficiency; however, their use presents several issues, including high energy consumption, the use of refrigerants that may harm the ozone layer, and limited flexibility for small-scale applications [1]. Consequently, there is growing interest in alternative cooling technologies that are simpler and more environmentally sustainable. These concerns are widely summarized in review studies [2], [3].

One promising solution is the Thermoelectric Cooler (TEC), which utilizes the Peltier effect to generate cooling without the need for working fluids. When an electric current is applied, TEC modules absorb heat from one side (cold side) and release it on the opposite side (hot side). These characteristics make TECs widely used in portable cooling systems, food and medicine storage, medical devices, and electronic component cooling such as computer processors. The main advantages of TEC systems include their simple structure, absence of vibration, refrigerant-free operation, and ease of electronic control [4].

However, TEC-based cooling systems have an inherent drawback in the form of low thermal efficiency. This low efficiency is primarily caused by limitations in heat dissipation on the hot side of the module. If the heat from the hot side is not effectively removed, the module temperature will rise, reducing the temperature differential between the hot and cold sides and consequently decreasing cooling capacity [5]. In addition, increasing the electrical current supplied to the module generates Joule heating losses, which further degrade cooling performance [6].

To address these issues, a more effective heat dissipation system is required. One widely adopted innovation is the integration of a Water Cooling Block (WCB) and a heatsink–fan (HSF) assembly on the hot side of the thermoelectric module. This combination enables faster heat removal because the water inside the WCB has a high heat capacity and can absorb thermal energy efficiently [7], [8]. Meanwhile, the heatsink–fan accelerates air convection, allowing the heat absorbed by the coolant to be released rapidly into the environment. This integrated system has been proven to reduce the hot-side temperature and directly improve cooling performance and the Coefficient of Performance (COP). However, systematic and design-oriented comparisons of WCB versus compact HSF under identical TEC modules, boundary conditions, and operating-current sweeps particularly for cooler-box configurations remain limited, leaving the performance tradeoffs insufficiently quantified.

Several previous studies have demonstrated that water-based cooling significantly enhances TEC system efficiency [9], [10]. Research by Adeniji et al. reported that the use of a water cooling block could reduce hot-side temperature by more than 15 °C compared with natural air cooling [11]. Similarly, Sharma found that increasing the water flow rate in a WCB system improved cooling capacity by up to 25% before reaching thermal saturation [12]. These findings emphasize that effective heat dissipation design is a key factor in improving thermoelectric performance [13].

Although various experimental studies have been conducted, purely experimental approaches have limitations in explaining the complex interactions between electrical and thermal aspects within the system [14]. Therefore, a mathematical modeling approach is needed to describe system behavior comprehensively. Such an approach enables analysis of the relationships among electrical current, temperature difference, heat transfer rate, and COP without requiring repetitive physical testing. Mathematical models can also be used to determine optimal operating conditions and evaluate the effectiveness of additional heat dissipation components such as WCBs and heatsink–fans in improving overall system efficiency. Lumped-parameter, energy-balance TEC models are commonly used to predict T_c, T_h, Q_c, and COP and to identify optimum operating current, providing a justified basis for the present approach [15], [16].

This study specifically focuses on the mathematical modeling and thermal performance analysis of a Thermoelectric Cooler Box (TECB) equipped with a Water Cooling Block (WCB) and a heatsink–fan. Unlike prior work that often evaluates a single heat-rejection option or reports limited operating points, this study applies a unified model and Python-based current sweep to directly compare WCB and HSF for the TEC1-12706 under consistent assumptions, thereby making the performance tradeoffs (temperature distribution, Q_c, and COP) explicit for cooler-box design. The novelty of this research lies in combining mathematical modeling with Python-based numerical simulations to compare the efficiency of two heat dissipation systems (WCB and HSF) for the TEC1-12706 module, a topic that has received limited attention in previous literature [8], [17].

2. METHODS

The cooling system modeled in this study consists of a single thermoelectric (TEC) module installed between a cold plate and a hot-side heat rejection system (either a Water Cooling Block (WCB) or a heatsink–fan (HSF), depending on the configuration analyzed). On the hot side, heat generated by the module is transferred to the coolant water through conduction in the WCB (WCB configuration) or directly to the surrounding air through the heatsink–fan (HSF configuration). Meanwhile, the cold side of the module absorbs heat from the air inside the cooler box through a lumped/effective internal convection coefficient h_{box} [2], [3].The cooling process is driven by the Peltier effect, whereas the primary heat losses originate from Joule heating due to the applied electrical current and back-conduction of heat from the hot side to the cold side [15], [16]. The schematic design of the system, including the heat flow direction and the function of each component, is shown in Figure 1.

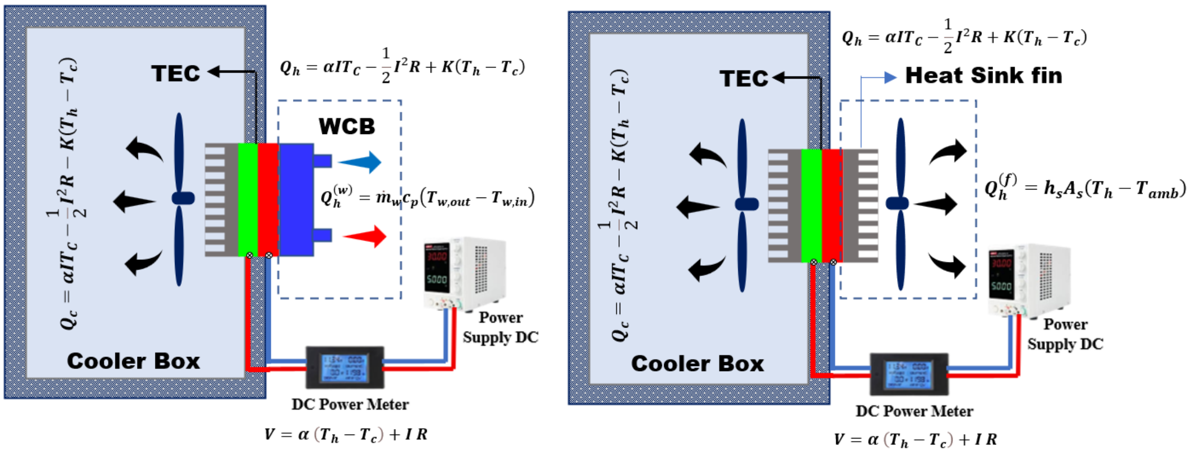

Figure 1. Schematic of the mathematical model of the Thermoelectric Cooler Box (TEC) equipped with a Water Cooling Block (WCB) and a heatsink–fan.

To simplify the calculation process, the present model adopts several assumptions. The thermoelectric (TEC) module material is considered homogeneous and isotropic. Heat transfer is assumed to occur only in one dimension, from the cold side to the hot side. The ambient temperature is maintained at 30 °C. Heat transfer through the WCB and heatsink is treated as a steady-state process, and the cooling effect due to natural convection is neglected on the hot-side external heat rejection path in comparison with forced convection generated by the fan. In contrast, heat transfer on the cold side is represented using the effective internal coefficient h_{box} (Table 1) to couple the box air to the cold surface. For each operating current, T_c and T_h are solved as steady-state values (quasi-steady current sweep), and transient cooling of the box air is not considered in this model.

The operating current in the simulation ranges from 1 A to 7 A, with increments of 1 A. For each current level, the cold-side temperature (T_c), hot-side temperature (T_h), absorbed heat load (Q_c), rejected heat (Q_h), and the coefficient of performance (COP) are calculated based on the ratio between cooling capacity and electrical input power.

The mathematical modeling of the Thermoelectric Cooler Box (TEC–WCB–Heatsink–Fan) system is derived from the energy balance on both the cold and hot sides of the thermoelectric module. The model incorporates the three dominant mechanisms governing TEC operation: the Peltier effect, thermal conduction, and Joule heating resulting from the applied electrical current [10], [18]. All thermal/electrical parameters and symbols used in the governing relations are defined with units in the corresponding parameter tables.

Table 1. Input data for the mathematical simulation of the TEC–WCB–Heatsink system.

No	Parameter	Symbol	Value	Unit	Description
1	Seebeck coefficient	α	0.045	V/K	Voltage generated per temperature difference across the TEC module
2	Internal electrical resistance	R_mod	2.5	Ω	Internal electrical resistance of the TEC module
3	Thermal conductivity of TEC module	K_th	0.5	W/K	Heat conduction between the hot and cold sides of the TEC
4	Ambient temperature	T_amb	30.0	°C	Temperature of the surrounding air
5	Initial temperature inside the box	T_box	25.0	°C	Initial air temperature inside the cooling chamber
6	Convective heat transfer coefficient (cold side)	h_box	5.0	W/m²K	Convective heat transfer coefficient on the cold side
7	Cold-side surface area	A_c	0.02	m²	Contact area between TEC cold side and cooler box
8	Heatsink convective coefficient	h_s	50.0	W/m²K	Convective heat transfer coefficient on the hot side
9	Heatsink surface area	A_s	0.03	m²	Heat transfer area on the hot side
10	Contact area of water block	A_wb	0.01	m²	Heat transfer area between water cooling block and TEC

11	Water mass flow rate	ṁ_w	0.15	kg/s	Mass flow rate of coolant in the water block
12	Water density	ρ_w	1000.0	kg/m³	Density of coolant (water)
13	Dynamic viscosity of water	μ_w	1×10⁻³	Pa·s	Dynamic viscosity of water at room temperature
14	Specific heat capacity of water	c_p	4182.0	J/kg·K	Heat capacity of water
15	Thermal conductivity of water	k_w	0.6	W/m·K	Thermal conductivity of water
16	Hydraulic diameter of coolant channel	D_h	0.01	m	Hydraulic diameter of the water block channel
17	Operating current range	I	1.0 – 7.0	A	Current range used in TEC performance simulation

The mathematical modeling of the Thermoelectric Cooler system (TEC–WCB–Heatsink–Fan) is developed based on the energy balance between the cold and hot sides of the TEC module. The relationship between the electrical and thermal parameters of the TEC is expressed through a series of equations (1–21), as presented in Tables 2 and 3. To avoid ambiguity, each equation is accompanied by explicit variable definitions; Eq. (20) is provided as an algebraic rearrangement of Eq. (2) for computational convenience, hence they are identical in form and outcome.

Table 2. Basic mathematical formulations for the Thermoelectric Cooler (TEC) module

Limitations	Calculations	No
Cold-side temperature	$T_c = T_h - \Delta T_0 + \beta I$	(1)
Hot-side temperature	$T_h = T_{amb} + Q_h R_{th,total}$	(2)
Temperature difference between the hot and cold sides	$\Delta T = T_h - T_c$	(3)
Cooling capacity at the cold side	$Q_c = \alpha I T_c - \frac{1}{2} I^2 R - K(T_h - T_c)$	(4)
Heat rejection rate at the hot side	$Q_h = \alpha I T_c - \frac{1}{2} I^2 R + K(T_h - T_c)$	(5)
Electrical voltage across the TEC module	$V = \alpha(T_h - T_c) + IR$	(6)
Total electrical power input	$P_t = VI = \alpha I(T_h - T_c) + I^2 R$	(7)
Coefficient of Performance (COP)	$COP = \frac{Q_c}{P_t}$	(8)
Optimum operating current	$I_{opt} = \frac{K(T_h - T_c)}{\alpha(T_h - T_c) + \frac{1}{2} R}$	(9)

Table 3. Heat transfer parameters of the Water Cooling Block (WCB)

Limitations	Calculations	No
Cooling water mass flow rate	$\dot{m}_w = \rho_w A_{ch} V_w$	(10)
Heat dissipated by the Water Cooling Block	$Q_h^{(w)} = \dot{m}_w c_{p,w}(T_{w,out} - T_{w,in})$	(11)
Heat dissipated by the heatsink–fan assembly	$Q_h^{(f)} = h_s A_s (T_h - T_{amb})$	(12)
Reynolds number of the cooling water flow	$Re = \frac{\rho_w u D_h}{\mu_w}$	(13)

Prandtl number of the coolant	$Pr = \frac{c_{p,w}\mu_w}{k_w}$	(14)
Nusselt number (Dittus–Boelter correlation)	$Nu = 0.023\, Re^{0.8} Pr^{0.4}$	(15)
Convective heat transfer coefficient of the WCB	$h_w = \frac{Nu\, k_w}{D_h}$	(16)
Convective thermal resistance of the WCB	$R_{\text{th,w}} = \frac{1}{h_w A_w}$	(17)
Convective thermal resistance of the heatsink–fan	$R_{\text{th,hs}} = \frac{1}{h_s A_s}$	(18)
Total thermal resistance on the hot side	$R_{\text{th,total}} = R_{\text{th,TEC}} + R_{\text{th,w}} + R_{\text{th,hs}}$	(19)
Hot-side temperature based on total thermal resistance	$T_h = T_{\text{amb}} + Q_h R_{\text{th,total}}$	(20)
Cold-side temperature derived from the box air temperature	$T_c = T_{\text{box}} + Q_c R_{\text{th,cold}}$	(21)

The mathematical formulations (1)–(21) described above constitute the foundation of the numerical model used to predict the temperature distribution, cooling capacity, and coefficient of performance of the Thermoelectric Cooler Box (TEC) system under two cooling configurations: the Water Cooling Block (WCB) and the heatsink–fan (HSF). All equations were implemented using Python programming, with operating current variations ranging from 1 to 7 A to obtain the thermal performance profile of the system. Each current point is treated as a steady-state operating condition (quasi-steady sweep), and transient responses are outside the present scope.

3. RESULTS AND DISCUSSION

3.1 Cold-Side Temperature Response Under Varying Electrical Current

Figure 2 illustrates the relationship between electrical current and the cold-side temperature (T_c) for the two cooling configurations, namely the Water Cooling Block (WCB) and the heatsink fan (HSF). The graph shows that increasing the current results in a decrease in cold-side temperature for both systems. However, the temperature reduction in the WCB configuration is significantly greater than in the HSF system [10], [11]. This phenomenon occurs because, in thermoelectric systems, higher current intensifies the Peltier effect, which governs heat transfer from the cold side to the hot side of the TEC module. As the current increases, more electrons transport thermal energy, resulting in stronger cooling on the cold side. Nevertheless, this beneficial effect is only maintained if the heat on the hot side (T_h) can be effectively dissipated to the environment. In the HSF configuration, heat rejection relies solely on forced-air convection, where air has relatively low specific heat capacity (C_p) and thermal conductivity compared with water. In contrast, the WCB system utilizes water as the coolant, enabling faster heat absorption through conduction and forced circulation. This mechanism helps maintain a stable and lower hot-side temperature (Th), thereby increasing the temperature difference ($\Delta T = T_h - T_c$). These results confirm that the effectiveness of heat removal on the hot side has a direct impact on cold-side cooling performance. Consequently, the WCB provides superior thermal stability for the TEC module, reduces the risk of overheating, and sustains optimal cooling performance over longer operating durations [19]. However, the larger ΔT produced by WCB also increases conductive heat leakage (back-conduction, $K\Delta T$) from the hot side to the cold side, which can reduce net Qc and COP even when Tc becomes lower (discussed later in Sections 3.2–3.3).

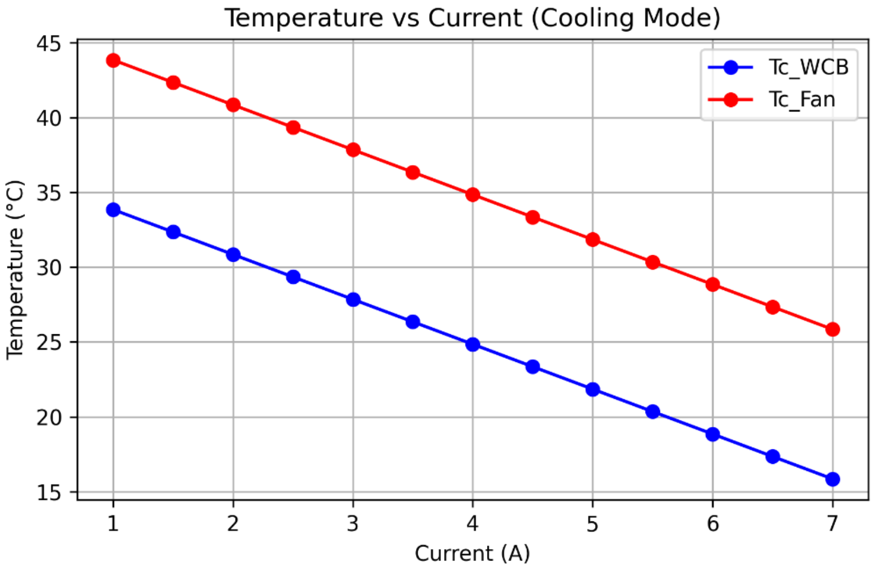

Figure 2. Relationship between electrical current and cold-side temperature ($T_{(c)}$ of WCB and $T_{(c)}$ of HSF).

3.2 Cooling Capacity Characteristics as a Function of Electrical Current

Figure 3 presents the relationship between cooling capacity (Q_c) and electrical current (I). In general, both the WCB and the HSF systems exhibit an increasing trend in Q_c as the current increases. This behavior aligns with the fundamental theory of the Peltier effect, where the cooling capacity is proportional to the applied current up to the optimum operating limit of the module. However, the simulation results show that the Q_c values of the HSF system are slightly higher than those of the WCB system across all current levels.

The relation of cooling capacity and current can be explained using the Peltier equation. At a given current, the net cooling capacity may be written as: $Q_c = \alpha I T_c - \frac{1}{2} I^2 R - K\Delta T$ where $\alpha I T_c$ is the Peltier cooling term, $\frac{1}{2} I^2 R$ is the Joule-heating penalty, and $K\Delta T$ represents back-conduction. The WCB system produces a lower cold-side temperature (T_c) due to its more effective hot-side heat dissipation. A lower T_c reduces the contribution of the $\alpha I T_c$ term in the Peltier cooling equation, resulting in a slightly lower Q_c compared with the HSF system [20], [21]. Nevertheless, the difference is relatively small (<10%) and does not indicate a substantial reduction in performance. Another factor influencing this behavior is back-conduction ($K\Delta T$). Since the WCB system maintains a larger temperature difference ΔT, conductive heat losses between the cold and hot sides become slightly higher, which further decreases the net Q_c [22], [23]. From a practical standpoint, these findings indicate that although the HSF system yields slightly higher cooling output, it does so at the cost of higher hot-side temperature and reduced thermal stability; moreover, achieving the same low T_c as WCB would typically require higher current and thus higher electrical power input. In contrast, the WCB system offers superior thermal stability and overall efficiency, even though its Q_c values are marginally lower.

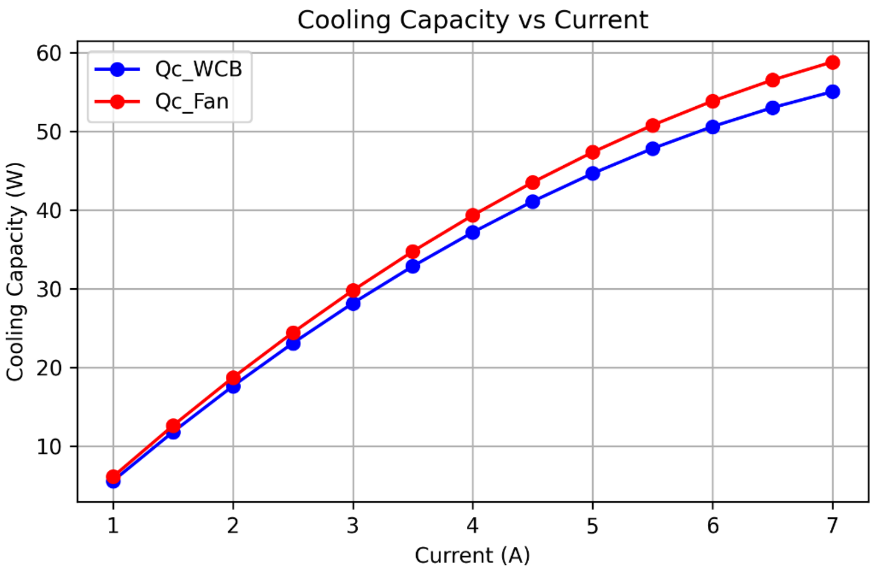

Figure 3. Variation of cooling capacity (Q_c) for WCB and HSF systems with electrical current.

3.3 Coefficient of Performance Trend with Increasing Electrical Current

Figure 4 shows the relationship between the Coefficient of Performance (COP) and the electrical current. Both systems exhibit similar characteristics: the COP increases at low currents, reaches a peak at approximately I = 3–4 A, and then decreases at higher currents. This behavior reflects the existence of an optimal operating point for the thermoelectric module. At low currents, an increase in current causes Qc to rise more rapidly than the electrical power input (Pt = V × I), leading to improved efficiency. However, at higher currents, power losses due to Joule heating (I^2R) become dominant, resulting in a reduction in COP [10]. Across the entire current range, the HSF system consistently achieves slightly higher COP values compared with the WCB system. This behavior is associated with the lower cold-side temperature (T_c) produced by the WCB configuration, which reduces the $\alpha I T_c$ term in the Peltier cooling equation, leading to a slightly lower net cooling capacity under the same operating current [20], [21]. In other words, although WCB increases ΔT and lowers T_c, the net Q_c can decrease because the $\alpha I T_c$ term drops while the back-conduction loss $K\Delta T$ increases; since $COP= Q_c/P_{in}$ and P_{in} is comparable at the same current, this slightly lower Q_c translates into a slightly lower COP. Even so, the performance difference remains small (approximately 5–7%), indicating that both systems operate within similar efficiency ranges. Despite having a slightly lower COP, the WCB configuration maintains superior thermal stability due to more effective heat rejection at the hot side. By keeping Th lower and more stable, WCB minimizes thermal accumulation and preserves a stronger temperature gradient across the TEC module, which contributes to long-term reliability and reduces thermal degradation [22], [23].

The maximum COP of the WCB system reaches approximately 0.78, while the HSF system peaks at around 0.83 within the 3–4 A range. These findings are consistent with previous studies reporting that water-based heat exchangers enhance hot-side heat removal, improve thermal uniformity, and optimize operational conditions for thermoelectric devices [24]. Liu et al. further demonstrated that COP is strongly dependent on hot-side fluid temperature, aligning with the present results that show improved performance stability in systems using water cooling [25]. This emphasizes the critical importance of efficient heat rejection in maximizing the performance of thermoelectric cooling systems [26]. Overall, the simulation results demonstrate that the TEC system equipped with a Water Cooling Block and a heatsink–fan provides a more balanced heat distribution between the hot and cold sides. The stable ΔT observed in the medium current range (approximately 2–4 A), along with the maximum COP occurring within this interval, indicates that the system can operate efficiently when the current is adjusted to its optimal value. These findings agree with earlier studies highlighting that enhanced hot-side cooling significantly improves thermoelectric efficiency [19], [27]. Therefore, the mathematical model developed in this study successfully represents the physical behavior of the TEC and can serve as a foundation for design optimization using CFD simulations or for future experimental validation. In real implementation, WCB is generally more suitable for long-duration operation, higher ambient temperatures, or applications prioritizing thermal stability and reliability (at the expense of added components such as pump/tubing), whereas HSF is more suitable for low-cost, compact, and portable systems where simplicity and ease of maintenance are primary requirements.

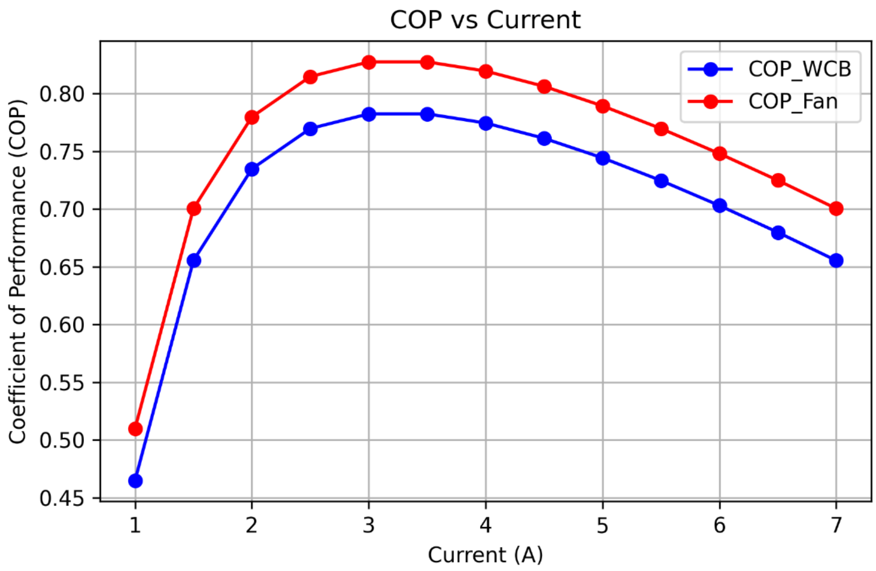

Figure 4. Comparison of COP between the WCB and HSF systems.

4. CONCLUSION

Based on the results of the mathematical modeling and numerical analysis conducted in this study, the following conclusions can be drawn:

1. Increasing the electrical current supplied to the thermoelectric module (TEC1-12706) leads to a rise in the hot-side temperature (T_h) and a decrease in the cold-side temperature (T_C), reaching an optimum point at approximately 4 A, where the maximum temperature difference (ΔT) is about 28 °C.
2. The Water Cooling Block (WCB) configuration is capable of maintaining a lower hot-side temperature, achieving 6–8 °C lower T_h compared with the Heatsink–Fan (HSF) system. This confirms that the water-cooling approach provides more effective heat rejection than air-based cooling.
3. The cooling capacity (Q_C) of the WCB system is slightly lower (<10%) than that of the HSF system due to increased back-conduction heat transfer resulting from the larger ΔT. Nevertheless, the WCB system demonstrates superior thermal stability, especially during sustained operation.
4. The maximum COP for both systems occurs at medium current levels (≈3–4 A), which represents the most efficient operating point before Joule heating (I^2R) becomes dominant.
5. Simulation results indicate that the HSF system achieves a slightly higher COP (about 5–7%) than the WCB system over the entire current range. However, the WCB configuration still provides better long-term stability, as its more effective hot-side cooling reduces thermal accumulation and maintains a stronger temperature gradient across the TEC module.
6. The mathematical model developed in this study successfully captures the physical behavior of the TEC system, including the interaction of Peltier cooling, Joule heating, back conduction, and hot-side heat removal. Therefore, it can serve as a foundation for design optimization, CFD-based investigations, or future experimental validation of water-cooled thermoelectric systems. From a design perspective, these results imply that selecting WCB versus HSF should be based on the target application: WCB is preferable when hot-side temperature control and long-duration stability are critical, while HSF is preferable when simplicity, compactness, and lower system complexity are prioritized, with the operating current ideally maintained near 3–4 A for efficient performance.

5. REFERENCES

[1] M. Mirmanto, S. Syahrul, M. Wirawan, I. M. A. Sayoga, A. T. Wijayanta, and I. Mahyudin, "Performance of a Thermoelectric Powered by Solar Panel for a Large Cooler Box," *Adv. sci. technol. eng. syst. j.*, vol. 5, no. 1, pp. 325–333, Feb. 2020, doi: 10.25046/aj050141.
[2] K. Zhu *et al.*, "A general White–Box strategy for designing thermoelectric cooling system," *InfoMat*, vol. 4, no. 11, p. e12324, Nov. 2022, doi: 10.1002/inf2.12324.
[3] Z. Xu, C. Li, H. Zhao, Y. Zheng, and J. Zhang, "Design and performance analysis of hot side heat sink of thermoelectric cooler device based on simulation and experiment," *Energy Science & Engineering*, vol. 11, no. 12, pp. 4463–4480, Dec. 2023, doi: 10.1002/ese3.1591.

[4] F. A. M. A. Ali, S. M. A. M. Reda, M. A. M. Hussein, S. K. Ayed, L. Jassim, and H. S. Majdi, "Thermoelectric-Driven Room Air Cooling via a Multi-U Shaped Heat Sink System," *IJHT*, vol. 41, no. 4, pp. 1000–1006, Aug. 2023, doi: 10.18280/ijht.410421.
[5] E. Yudiyanto, R. S. Setiabudi, A. Hardjito, S. Adiwidodo, and B. Pranoto, "Effect of Velocity and Type of Cooling Fluid on Peltier Heat Transfer for Car Cabin Cooling Applications," *JSAE*, vol. 5, no. 2, p. 76, Sep. 2022, doi: 10.31328/jsae.v5i2.4036.
[6] P. E. Ruiz-Ortega, M. A. Olivares-Robles, and C. A. Badillo-Ruiz, "Transient thermal behavior of a segmented thermoelectric cooler with variable cross-sectional areas," *Int J Energy Res*, vol. 45, no. 13, pp. 19215–19225, Oct. 2021, doi: 10.1002/er.7123.
[7] B. Pfeiffelmann, A. C. Benim, and F. Joos, "Water-Cooled Thermoelectric Generators for Improved Net Output Power: A Review," *Energies*, vol. 14, no. 24, p. 8329, Dec. 2021, doi: 10.3390/en14248329.
[8] N. T. Atmoko, A. Jamaldi, and T. W. B. Riyadi, "An Experimental Study of the TEG Performance using Cooling Systems of Waterblock and Heatsink-Fan," *AE*, vol. 5, no. 3, pp. 261–267, Jun. 2022, doi: 10.31603/ae.6250.
[9] Kennedy, K. Anwar, A. Muis, B. Basri, and M. Ilhamsyah, "Effect of thermoelectric placement on the commercial waterblock to the liquid cooling system performance," *J. Phys.: Conf. Ser.*, vol. 1763, no. 1, p. 012039, Jan. 2021, doi: 10.1088/1742-6596/1763/1/012039.
[10] Politeknik Negeri Bali, I. W. Sutina, A. Winarta, Politeknik Negeri Bali, I. N. A. A. Saputra, and Politeknik Negeri Bali, "Performance Analysis of Thermoelectric Cooler Box with Water Cooling Block (WCB) and Heat Sink Fan," *LOGIC*, vol. 25, no. 2, pp. 93–99, Jul. 2025, doi: 10.31940/logic.v25i2.93-99.
[11] A. P. Adeniji, R. Sule, E. I. Ogunwale, and W. A. Ayara, "Development and Performance Evaluation of Portable water-cooling system using thermoelectric peltier modules," *IOP Conf. Ser.: Earth Environ. Sci.*, vol. 1492, no. 1, p. 012024, Apr. 2025, doi: 10.1088/1755-1315/1492/1/012024.
[12] H. Sharma, G. Saxena, R. Randa, and R. S. Rajput, "Novel hybrid vehicle battery cooling system: Integrating Peltier-based heat sinks for control of thermal management," *Proceedings of the Institution of Mechanical Engineers, Part C: Journal of Mechanical Engineering Science*, vol. 239, no. 17, pp. 7135–7157, Sep. 2025, doi: 10.1177/09544062251343501.
[13] N. Numan, M. Mahdi, and M. Ahmed, "A Comparative Experimental Study Analysis of Solar Based Thermoelectric Refrigerator Using Different Hot Side Heat Sink," *ETJ*, vol. 40, no. 1, pp. 90–98, Jan. 2022, doi: 10.30684/etj.v40i1.2058.
[14] B. I. Robertson, Y.-H. Shin, and J.-W. Choi, "A Thermoelectric Temperature Control Module for a Portable Fluorescent Sensing Platform," *J. Electrochem. Soc.*, vol. 167, no. 14, p. 147505, Nov. 2020, doi: 10.1149/1945-7111/abc35d.
[15] E. Fang, X. Wu, Y. Yu, and J. Xiu, "Numerical modeling of the thermoelectric cooler with a complementary equation for heat circulation in air gaps," *Open Physics*, vol. 15, no. 1, pp. 27–34, Mar. 2017, doi: 10.1515/phys-2017-0004.
[16] L. Li *et al.*, "Performance Optimization of a Thermoelectric-Water Hybrid Cooling Garment," *Adv Materials Technologies*, vol. 9, no. 21, p. 2301069, Nov. 2024, doi: 10.1002/admt.202301069.
[17] Y. Ma, M. Zhao, J. Li, J. Wang, and L. Hu, "Cooling Effect of Different Land Cover Types: A Case Study in Xi'an and Xianyang, China," *Sustainability*, vol. 13, no. 3, p. 1099, Jan. 2021, doi: 10.3390/su13031099.
[18] T. N. Widianto and C. Mahendra, "Kinerja Susunan dan Jumlah Elemen Peltier pada TEC Alat Transportasi Ikan Segar," *JPBKP*, vol. 14, no. 1, p. 75, Jun. 2019, doi: 10.15578/jpbkp.v14i1.567.
[19] M. J. Dousti and M. Pedram, "Platform-dependent, leakage-aware control of the driving current of embedded thermoelectric coolers," in *International Symposium on Low Power Electronics and Design (ISLPED)*, Beijing, China: IEEE, Sep. 2013, pp. 311–316. doi: 10.1109/ISLPED.2013.6629315.
[20] Z. Tark, A. J. Hamed, and A. H. N. Khalifa, "Performance Study of the Thermoelectric Personal Cooler under Different Ambient Temperatures," *IJHT*, vol. 40, no. 1, pp. 53–62, Feb. 2022, doi: 10.18280/ijht.400107.
[21] T. Tanehira, Y. Furubayashi, A. Yamamoto, K. Yonemori, S. Miyoshi, and S.-I. Kuroki, "Calculation of Seebeck Coefficients for Advanced Heat Transfer Modules," *ECS Trans.*, vol. 80, no. 5, pp. 57–62, Aug. 2017, doi: 10.1149/08005.0057ecst.
[22] N. Wang *et al.*, "An Enhanced Thermoelectric Collaborative Cooling System With Thermoelectric Generator Serving as a Supplementary Power Source," *IEEE Trans. Electron Devices*, vol. 68, no. 4, pp. 1847–1854, Apr. 2021, doi: 10.1109/TED.2021.3059183.
[23] P. Kolber, D. Perczyński, and K. Peszyński, "Investigation of A Thermoelectric Cooling System Based on A Peltier Module Using A Temperature Chamber," presented at the Engineering Mechanics 2020, 2020, pp. 278–281. doi: 10.21495/5896-3-278.
[24] A. Żelazna and J. Gołębiowska, "A PV-Powered TE Cooling System with Heat Recovery: Energy Balance and Environmental Impact Indicators," *Energies*, vol. 13, no. 7, p. 1701, Apr. 2020, doi: 10.3390/en13071701.

[25] Z. B. Liu, L. Zhang, G. Gong, Y. Luo, and F. Meng, "Experimental study and performance analysis of a solar thermoelectric air conditioner with hot water supply," *Energy and Buildings*, vol. 86, pp. 619–625, Jan. 2015, doi: 10.1016/j.enbuild.2014.10.053.
[26] K. Roungbungrud, P. Chantawong, and J. Khedari, "Development of a Stand-Alone Thermoelectric Power Generator Using Heat of Refrigerant Leaving the Condenser and Self-Cooled by Condensate of a Split-Type Air Conditioning," *IJHT*, vol. 40, no. 3, pp. 737–742, Jun. 2022, doi: 10.18280/ijht.400311.
[27] S. B. Riffat and G. Q. Qiu, "Design and characterization of a cylindrical, water-cooled heat sink for thermoelectric air-conditioners," *Int. J. Energy Res.*, vol. 30, no. 2, pp. 67–80, Feb. 2006, doi: 10.1002/er.1124.

LOGIC
Journal of Engineering Design and Technology
Vol. 26 No. 1 March 2026 ; p. 39 - 47

p-ISSN : 1412-114X
e-ISSN : 2580-5649
http://ojs2.pnb.ac.id/index.php/LOGIC

EXPERIMENTAL AND CFD ANALYSIS OF A LABORATORY-SCALE PARALLEL FLOW SHELL AND TUBE HEAT EXCHANGER

1) Mechanical Engineering Study Program, Faculty of Engineering, Universitas Muhammadiyah Gresik, Indonesia
2) Department of Mechanical Engineering, Politeknik Negeri Malang, Indonesia

Correponding email [1)*] :
alvianihesthi@umg.ac.id

Alviani Hesthi Permata Ningtyas [1)*], Siti Duratun Nasiqiati Rosady [2)], Ilham Arifin Pahlawan [1)], Rilo Chandra Muhamadin [1)]

Abstract. A heat exchanger is a device that functions to change the temperature of a fluid by utilizing the heat transfer mechanism from a high-temperature fluid to a lower-temperature fluid. This study was conducted to design and analyze the performance of a shell and tube heat exchanger with a parallel flow configuration on a laboratory scale. The design process focused on determining the main dimensions and components, such as tube length and the ratio between shell and tube diameters, to ensure optimal operation for laboratory experiments. After the device was successfully fabricated, experiments were carried out to obtain temperature data of the hot and cold fluids at both the inlet and outlet. These experimental data were then compared with the results of numerical simulations using ANSYS Fluent software based on the Computational Fluid Dynamics (CFD) method. The simulation was used to visualize the flow pattern and temperature distribution within the heat exchanger, as well as to calculate heat transfer efficiency. The results showed good agreement between the simulation and experimental data, the deviation is 15%, where the inlet temperature of the hot fluid was 65°C and the outlet temperature was 38°C, indicating the validity of the numerical model used. From this study, it can be concluded that the combination of experimental design and CFD simulation analysis provides a more comprehensive understanding of the temperature distribution and efficiency of a shell and tube heat exchanger with a parallel flow configuration.

Keywords : heat exchanger; simulation; design; fabrication.

1. INTRODUCTION

Heat transfer is an essential element in various engineering processes, including in industries that utilize heating, cooling, and power generation systems[1]–[6]. One of the key tools that supports this process is the heat exchanger[7]–[13]The type of heat exchanger commonly used in industry is the shell and tube type, due to its ability to handle various types of fluids and high operating pressures. Hot fluid flows through the tubes, while cold fluid moves within the shell around the tubes. This system has several variations in fluid flow direction: parallel flow, counterflow, and crossflow[14]–[17]. The parallel flow configuration is characterized by fluids flowing from the inlet to the outlet side in parallel, both in the tubes and the shell. The main advantage of this design is its simplicity, but its drawback is the rapid decrease in temperature difference between the two fluids, resulting in relatively low heat transfer efficiency[17], [18]. A study by [11] discussed the design of shell and tube heat exchangers. In this research, the shell tube has an outer diameter of 300 mm and an inner diameter of 293.65 mm with a length of 1000 mm. The obtained heat transfer rate is 7117.5 watts. Based on TEMA standards and the application of HTRI, the required surface area is 8.27 m^2, while actual calculations show a surface area of 9.09 m^2. The research by [19]discusses a design with one shell pass and two tube passes. The tube length is 2.7 m with a diameter of 13 mm, while the shell measures 1.35 m in length and 70 mm in diameter. The material for the tube is copper with a conductivity of 385 W/mK, whereas the shell is made of aluminum with a conductivity of 205 W/mK. The results of this study show a maximum efficiency of 35.4040%. The research conducted by [14]focused more on the design of the heat exchanger dimensions. In that study, a tube length of 1.2 m, a shell length of 70 cm, and a total of 6 tubes were obtained. In the mixed temperature tests, the measured values ranged from 50°C to 25°C. Testing using CFD Ansys is often applied to understand temperature distribution and efficiency in heat exchangers [20]–[27]. The aim of this study is to design and evaluate the performance of a shell-and-tube type heat exchanger with parallel flow on a laboratory scale. This research includes the design of dimensions and main elements so that the device can operate optimally, experimental testing to obtain temperature data of hot and cold fluids, as well as numerical analysis using ANSYS Fluent based on CFD to visualize flow patterns and temperature distribution[28], [29]. The simulation results are then compared with experimental data to verify the numerical model and assess heat transfer efficiency, with the aim of obtaining a comprehensive understanding of the thermal performance of the heat exchanger.

2. METHODS

This research was conducted through three main stages: design, fabrication, and experimental testing of a laboratory-scale shell-and-tube heat exchanger with a parallel flow configuration. During the design stage, the primary geometric parameters were determined, including tube length, shell diameter, number of tubes, and material selection. These parameters were defined based on heat transfer considerations, structural integrity, and ease of assembly. The complete configuration was modeled using three-dimensional CAD software to ensure dimensional consistency and proper alignment of the parallel flow direction between shell- and tube-side fluids..

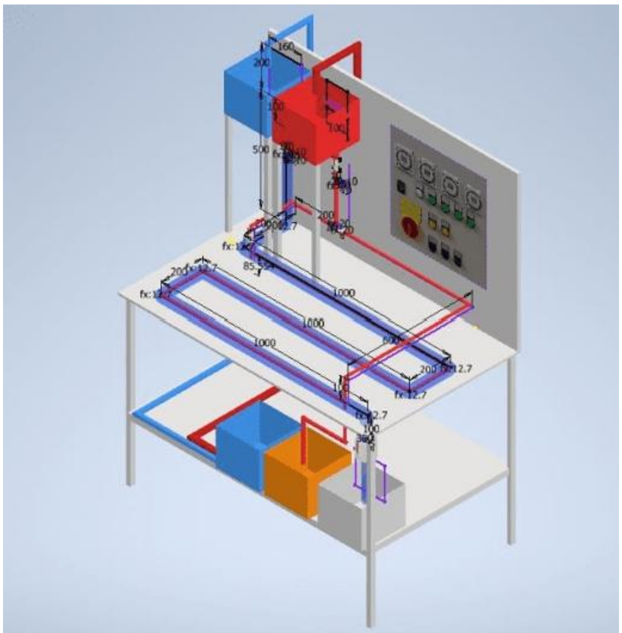

Figure 1. Heat Exchanger Design

Experimental testing was conducted using the dual-reservoir circulation system shown in Figure 1. The setup consists of two elevated tanks serving as hot- and cold-water supply reservoirs and two lower tanks for fluid collection and recirculation. Hot water was prepared in the upper reservoir using an electric heater prior to testing, while cold water was supplied from a separate reservoir to maintain controlled inlet conditions. The fluids were circulated through the shell-and-tube heat exchanger via a closed-loop piping system equipped with control valves, and the volumetric flow rate was maintained at 800 L/h as monitored by a calibrated flowmeter. After passing through the heat exchanger, both fluids were collected in the lower tanks and recirculated to ensure continuous operation.

Table 1. Shell and Tube Specifications

Description	Shell	Tube
Diameter	22 mm	6,35 mm
Length	3400 mm	3400 mm
Material Pipe	Acrylic	Aluminum

Temperature measurements at the hot and cold fluid inlets and outlets were obtained using calibrated K-type thermocouples installed at the respective pipe sections. The thermocouple readings were recorded manually at 5-minute intervals using a digital temperature display, while a stopwatch was used to ensure consistent time tracking throughout the 45-minute experimental duration. This procedure ensured systematic data collection while maintaining stable operating conditions for evaluating the thermal performance of the parallel-flow heat exchanger.

Although the system is referred to as a shell-and-tube heat exchanger, the laboratory-scale configuration used in this study consists of a single small copper tube in the inner section through which hot water flows, while cold water flows directly in contact with the outer surface of the inner tube within the surrounding cylindrical outer pipe. Geometrically, this arrangement more closely resembles a concentric (double-pipe) heat exchanger rather than a conventional multi-tube shell-and-tube system equipped with baffles for flow distribution. In the present study, no thermal insulation was applied to the outer surface of the external pipe, allowing heat transfer to occur primarily through conduction across the copper tube wall and convection on both fluid sides, with potential natural heat loss to the surrounding environment. The term “shell” is retained due to the presence of the external cylindrical enclosure; however, only a single tube pass is employed without the complex flow distribution characteristics typical of industrial shell-and-tube exchangers. This clarification is important to avoid ambiguity in interpreting flow distribution behavior, effective heat transfer area, and performance comparisons with industrial-scale shell-and-tube heat exchangers.

Both working fluids were modeled as incompressible water under steady-state and single-phase conditions. Thermophysical properties were assumed constant and evaluated at the respective mean bulk temperatures (ρ = 997 kg/m³, Cp = 4182 J/kg·K, k = 0.6 W/m·K, μ = 0.001 Pa·s). The realizable k–ε turbulence model with enhanced wall treatment was employed to accurately resolve near-wall thermal gradients. The computational mesh was refined in the boundary-layer region to maintain y^+ values below 5, ensuring appropriate resolution of the viscous sublayer and improved prediction of convective heat transfer coefficients. A conjugate heat transfer (CHT) approach was implemented by explicitly modeling the aluminum tube wall as a solid domain, allowing conductive heat transfer between the hot and cold fluid regions to be simultaneously solved with the governing energy equations. This approach improves thermodynamic consistency and provides a more realistic representation of the coupled convection–conduction mechanism within the heat exchanger.

.

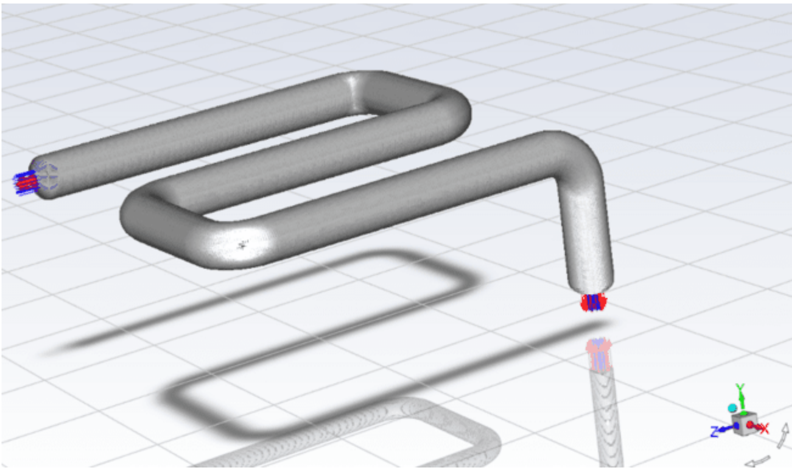

Figure 2. Meshing in ANSYS

Figure 2 shows the meshing results in ANSYS with inlet and outlet conditions, along with a total of 3,754,832 faces and 928,676 nodes. Figure 3 illustrates the schematic flow of fluid in the heat exchanger system with a parallel flow configuration. The cold fluid and hot fluid flow in opposite directions through two different paths, each marked by blue and red colors respectively. The cold fluid enters from the top left and exits at the bottom right, while the hot fluid also enters from the top left but exits at the bottom right through a different path. This schematic is equipped with temperature measurement points numbered 1 to 17, depicting the locations of temperature monitoring along the flow. This design allows for a more efficient heat transfer process through a consistent temperature difference between the two fluids. The realizable k–ε turbulence model with enhanced wall treatment was applied. Velocity inlet boundary conditions were specified according to the experimental flow rate (800 L/h) and measured inlet temperatures, while pressure outlet conditions were imposed at both exits. Convergence criteria were set to 10^{-6} for the energy equation and 10^{-4} for continuity and momentum equations. Mesh quality Ansys Metric in this simulation is 0.9 that means acceptable. The thermal performance of the heat exchanger was evaluated using the effectiveness–NTU method and the Log Mean Temperature Difference

(LMTD) approach[2]. The actual heat transfer rate was calculated from the energy balance:

$$Q = \dot{m}_h c_{p,h} (T_{h,in} - T_{h,out}) \tag{1}$$

$$Q = \dot{m}_c c_{p,c} (T_{c,out} - T_{c,in}) \tag{2}$$

where $\dot{m}$ is the mass flow rate (kg/s), c_p is the specific heat capacity (J/kg·K), and T represents fluid temperatures (°C or K).
The heat exchanger effectiveness (ε) is defined as:

$$\varepsilon = \frac{Q_{actual}}{Q_{max}} \tag{3}$$

where

$$Q_{max} = C_{min} (T_{h,in} - T_{c,in}) \tag{4}$$

and

$$C = \dot{m} c_p \tag{5}$$

$$C_{min} = \min\,(C_h, C_c) \tag{6}$$

The number of transfer units (NTU) is calculated as:

$$NTU = \frac{UA}{C_{min}} \tag{7}$$

where U is the overall heat transfer coefficient (W/m²·K) and $A$is the total heat transfer area (m²).
For a parallel-flow heat exchanger, the analytical effectiveness relation is:

$$\varepsilon = \frac{1 - \exp\,[-NTU(1 + C_r)]}{1 + C_r} \tag{8}$$

with

$$C_r = \frac{C_{min}}{C_{max}} \tag{9}$$

The overall heat transfer coefficient $U$was determined using the LMTD [1]method:

$$Q = UA\Delta T_{lm} \tag{10}$$

where the log mean temperature difference for parallel flow is:

$$\Delta T_{lm} = \frac{(T_{h,in} - T_{c,in}) - (T_{h,out} - T_{c,out})}{\ln\left(\frac{T_{h,in} - T_{c,in}}{T_{h,out} - T_{c,out}}\right)} \tag{11}$$

These formulations provide a rigorous thermodynamic basis for evaluating the experimental results and validating the CFD predictions of the parallel-flow shell-and-tube heat exchanger.

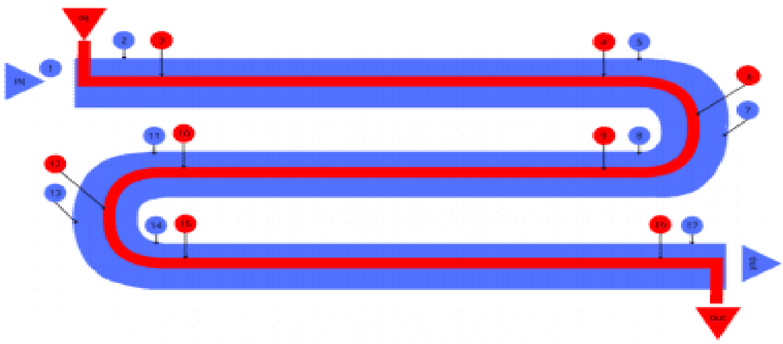

Figure 3. Fluid flow rate scheme

Figure 3 illustrates the schematic configuration of the parallel-flow heat exchanger. Both hot and cold fluids enter from the same axial direction and flow parallel along separate channels. Temperature measurement points (1–17) indicate monitoring locations used for experimental validation and numerical comparison. The red inner passage represents the hot fluid, while the surrounding blue domain corresponds to the cold fluid, separated by a solid wall that facilitates heat transfer primarily through conduction across the wall and convection within each fluid stream.

3. RESULTS AND DISCUSSION

The test results of the shell and tube type heat exchanger with a parallel flow configuration that has been completed, as shown in Figure 4. The testing was carried out to observe how well this device transfers heat by monitoring the temperature changes of the hot and cold fluids at the inlet and outlet at certain time intervals. The data in Table 2 show a significant temperature change in both fluids, indicating that the heat transfer process occurred as expected during the tests. These temperature changes were then analyzed to determine the effectiveness of the device, the thermal behavior of the system during operation, and serve as a basis for comparison with theoretical calculations and CFD simulation results in the following section.

Figure 4. Fabrication of heat exchanger

Figure 4 shows the heat exchanger that has been fabricated. The fabrication was carried out according to the design that had been calculated.

Table 2. Test result data

Time (m)	Temperature (°C)			
	Cold		Hot	
	Inlet	Outlet	Inlet	Outlet
5	19.3	26.3	54.8	45.7
10	20.2	25.9	59.7	44.6
15	19.6	25.4	59.6	43.2
20	22.3	27.6	65.6	42.2
25	21.1	26.1	69.3	38.4
30	20.1	26.9	54.7	38.3
35	22.8	27.4	55.6	37.6
40	23.6	26.5	62.4	36.7
45	20.8	26.3	67.3	45.7

Table 2 shows how the temperatures of cold water and hot water changed during testing from the 5th minute to the 45th minute. The cold water, which initially ranged from 19–23°C, appeared to rise to around 25–27°C as it exited the device, indicating that the cold water successfully absorbed heat. Meanwhile, the hot water entering at 54–69°C dropped to 37–46°C upon exit, showing that the heat transferred to the cold water. Although there were slight fluctuations in some data points, the overall pattern remained clear: the cold water became warmer, the hot water became cooler, indicating that the heat exchanger worked effectively.

Table 3. Calculated Thermal Performance Parameters

Parameter	Symbol	Equation	Value	Unit
Heat Capacity Rate	$C = \dot{m}c_p$	0.222×4180	927.96	W/K
Actual Heat Transfer Rate	Q_{actual}	$\dot{m}c_p(T_{c,out} - T_{c,in})$	5,010	W
Maximum Heat Transfer Rate	Q_{max}	$C_{min}(T_{h,in} - T_{c,in})$	37,000	W
Effectiveness	ε	Q_{actual}/Q_{max}	0.135	–
Temperature Difference 1	ΔT_1	$T_{h,in} - T_{c,in}$	39.89	°C
Temperature Difference 2	ΔT_2	$T_{h,out} - T_{c,out}$	14.88	°C
Log Mean Temperature Difference	ΔT_{lm}	LMTD formula	25.34	°C
Overall Heat Transfer Coefficient	U	$Q/(A\Delta T_{lm})$	2,916	W/m²K
Number of Transfer Units	NTU	UA/C_{min}	0.21	–
Capacity Ratio	C_r	C_{min}/C_{max}	1.0	–

Table 3 summarizes the calculated thermal performance parameters of the parallel-flow shell-and-tube heat exchanger under laboratory-scale operation. The heat capacity rate was determined as 927.96 W/K, resulting in an actual heat transfer rate of 5,010 W compared to a theoretical maximum of 37,000 W, yielding an effectiveness of 0.135. The measured terminal temperature differences (ΔT_1 = 39.89°C and ΔT_2 = 14.88°C) produced an LMTD of 25.34°C. Based on these values, the overall heat transfer coefficient was calculated as 2,916 W/m²K, with an NTU of 0.21 and a capacity ratio (C_r) of 1.0. A comparison with CFD simulation results can be seen in Figure 5 below.

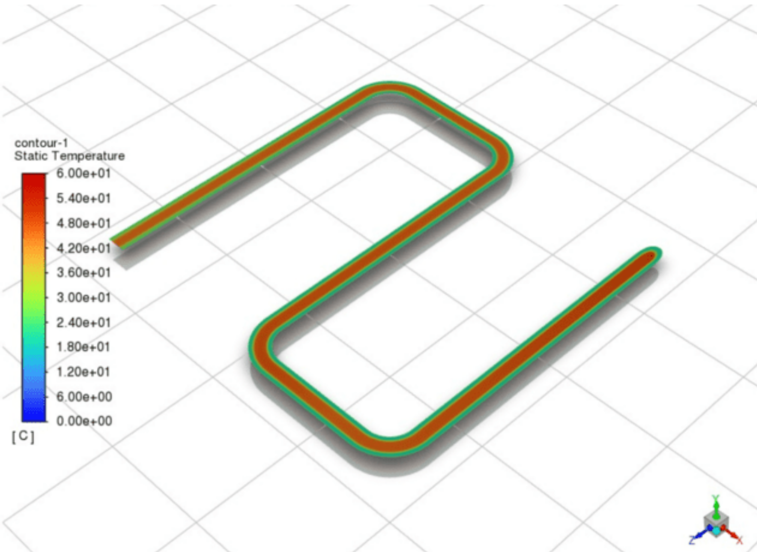

Figure 5. Temperature distribution in ANSYS software

Figure 5 shows the simulation results of the temperature distribution in a shell and tube type heat exchanger with a parallel flow configuration using ANSYS Fluent software. The color contours illustrate the decrease in temperature of the hot fluid from around 60°C at the inlet side (red color) to about 19.3°C at the outlet side (blue color). The uniform color gradient pattern indicates that an effective heat transfer process occurs along the fluid flow path. Experimental test results show that the heat transfer process in the shell and tube type heat exchanger with a parallel flow configuration is effective, as indicated by significant temperature changes in both the hot and cold fluids at each observation interval. The inlet temperature of the hot fluid ranges from 54.8°C to 69.3°C, while its outlet decreases to the range of 36.7–45.7°C. Meanwhile, the temperature of the cold fluid increased from 19.3C to about 27.6°C by the end of the test. The average temperature difference between the hot and cold fluids indicates that the conduction mechanism through the tube wall and convection on both sides of the fluid are working simultaneously and efficiently. Numerical simulations using ANSYS Fluent show a stable flow pattern and temperature distribution consistent with experimental results. The model, using the standard k-epsilon turbulence and second-order upwind discretization, is capable of accurately representing heat transfer phenomena. Simulation results indicate a temperature difference of 38°C at the hot fluid outlet and 26°C at the cold fluid outlet, with only about a 15.7% deviation from experimental results. The temperature contour from the simulation shows a linearly decreasing temperature gradient along the flow direction, indicating that the heat transfer rate is dominated by forced convection mechanisms.

The temperature contour presented in Figure 5 indicates localized regions where the hot-fluid temperature approaches the lower temperature range. It is important to emphasize that these values correspond to local minima within the computational domain rather than the mass-averaged outlet temperature. The bulk outlet temperature predicted numerically was approximately 38°C, which is in close agreement with experimental measurements and remains thermodynamically consistent with parallel-flow heat exchanger theory. Since no external heat loss was imposed in the numerical model, the reduction in hot-fluid temperature corresponds directly to the heat absorbed by the cold fluid, satisfying overall energy conservation. Furthermore, considering the relatively low NTU value (0.21) and effectiveness (0.135), the moderate outlet temperature difference observed is physically reasonable and aligns with established heat exchanger performance relations for parallel-flow configurations.

4. CONCLUSION

This study successfully designed and evaluated a laboratory-scale shell-and-tube heat exchanger with a parallel-flow configuration using experimental testing and CFD simulation in ANSYS Fluent. The results showed that the hot-fluid temperature decreased from approximately 65°C to around 38–41°C, while the cold-fluid temperature increased to about 26–27°C, confirming effective heat exchange. Thermal analysis yielded an average heat transfer rate of 5.01 kW, effectiveness (ε) of 13.5%, overall heat transfer coefficient (U) of 2916 W/m²K, and NTU of 0.21, indicating moderate thermal performance under the tested conditions. The deviation between experimental and numerical results was approximately 15.7%, demonstrating good model validation. For future research, it is recommended to vary the mass flow rate and compare other flow configurations, such as counter flow and cross flow, to obtain a broader range of heat transfer characteristics. Additionally, the use of tube materials with different thermal conductivities and variations in the number of baffles can be analyzed to optimize system efficiency. Further validation can be conducted by expanding the simulation domain and using more complex turbulence models, such as Realizable k-ε or k-ω SST, so that the simulation results more closely approximate real conditions.

5. ACKNOWLEDGEMENT

I would like to thank DPPM UMG for their assistance in completing this research.

6. REFERENCES

[1] K. P. Im, R. Allifia, E. Dia, P. Sari, and D. Pratiwi, "Pengaruh Laju Alir Fluida Panas dan Fluida Dingin terhadap besarnya Transfer Panas pada Alat Heat Exchanger," *Semin. Nas. Sains dan Teknol. Terap. X*, pp. 5–11, 2022.
[2] D. D. Saputra *et al.*, "Perancangan Alat Penukar Kalor Untuk Pemanas Air dengan Memanfaatkan Kondensat Panas Bumi Dieng PT XYZ," pp. 1855–1861, 2024.
[3] Suwarso, Y. Mariah, Nuradi, and S. Atti, "Perawatan Penukar Panas / Heat Exchanger Untuk Meningkatkan Kinerja Mesin Pendingin pada Kapal Niaga." pp. 11586–11597, 2024.
[4] F. S. D. Anggoro, "Rancang Bangun Helical Fin Pada Penukar Panas Double Pipe RANCANG BANGUN FIN TIPE HELICAL PADA PENUKAR PANAS DOUBLE PIPE Fajar Septiawan Dwi Anggoro I Made Arsana Abstrak," vol. 10, no. 2015, pp. 35–40, 2022.
[5] M. I. Kamil and D. A. Sari, "Komparasi Desain Alat Penukar Panas Tipe Air-Cooled," *J. Teknol.*, vol. 16, no. 2, pp. 180–186, 2023.
[6] S. Zhou, S. Yan, W. Zhang, H. Li, P. Niu, and Y. Shi, "Study on the heat discharging performance for a horizontal latent heat thermal energy storage exchanger with movable inner tube ☆," *J. Energy Storage*, vol. 152, no. PB, p. 120783, 2026, doi: 10.1016/j.est.2026.120783.
[7] F. Lubis and S. Lubis, "Analisis Baffle Cut Pada Alat Penukar Kalor Shell and Tube Pada Susunan Tabung Segi Empat," vol. 3, no. 1, pp. 39–44, 2021.
[8] F. Achmad *et al.*, "Efek laju alir dan arah aliran terhadap analisis performa alat penukar panas tipe shell and tube heat exchanger menggunakan SCADA," vol. 17, pp. 148–157, 2023, doi:

10.22146/jrekpros.77376.
[9] K. Astawa, I. G. T. P. Surya, and I. G. N. P. Tenaya, "Analisis Efektivitas Perpindahan Panas pada Alat Penukar Panas Jenis Water to Water," vol. 6, no. 1, pp. 26–30, 2022.
[10] Y. E. Pardede, "Analisa Laju Perpindahan Kalor Pada Alat Penukar Panas Kondensor Pembangkit Listrik Tenaga Uap (PLTU) di . PT XYZ," 2023.
[11] Y. Siswanto, K. W. Wirakusuma, and A. B. Pratama, "Rancang bangun alat penukar panas tipe pipa ganda kajian aliran berlawanan arah," vol. 05, no. 01, pp. 114–121, 2024.
[12] R. Yuniarti, F. Achmad, Y. L. Listyadevi, and L. Angraini, "JURNAL INTEGRASI PROSES Website : http://jurnal.untirta.ac.id/index.php/jip PENGARUH TEMPERATUR DAN ARAH ALIRAN TERHADAP EFEKTIVITAS PENUKAR PANAS NTU (Ɛ -NTU) PADA ALAT PENUKAR PANAS TIPE PLATE AND FRAME 1 Program Studi Teknik Kimia , Institut Teknologi Sumatera Jl . Terusan Ryacudu , Way Huwi , Kec . Jati Agung , Kabupaten Lampung Selatan , Lampung 2 Program Studi Teknik Kimia , Universitas Jenderal Achmad Yani Jl . Terusan Jenderal Sudirman , Cimahi , Jawa Barat 3 BRIN LIPI UPT Balai Pengolahan Mineral Lampung Jalan Ir . Sutami Km . 15 , Tanjung Bintang , Sindang Sari , Kabupaten Lampung Selatan , Lampung," vol. 11, no. 1, pp. 32–39, 2022.
[13] W. Ohoirenan, E. A. Rettob, and H. Dumatubun, "Analisis Perpindahan Panas Pada Aliran Searah (Current Flow) Dengen Pemanfaatan Pemanas Hieter Sistem Heat Exhanger," vol. 6, no. 1, pp. 54–56, 2025.
[14] C. Anuntasethakul and D. Banjerdpongchai, "Design of Supervisory Model Predictive Control for Building HVAC System with Consideration of Peak-Load Shaving and Thermal Comfort," *IEEE Access*, vol. 9, pp. 41066–41081, 2021, doi: 10.1109/ACCESS.2021.3065083.
[15] H. Kim, D. Sumiyoshi, and Y. Choi, "Development of flow rate and equipment simulation model for commercial building HVAC&R system by data-driven method," *J. Build. Eng.*, vol. 44, 2021, doi: 10.1016/j.jobe.2021.103303.
[16] Ahmad Maksum, Gun Gun Ramdlan Gunadi, Faiz Irza Ramadhan, and Candra Damis Widiyawaty, "Desain Fully Welded Plate Heat Exchanger untuk Pemanfaatan Asap Pirolisis dengan Metode Computational Fluid Dynamic (CFD)," *J. Mek. Terap.*, vol. 5, no. 1, pp. 8–15, 2024, doi: 10.32722/jmt.v5i1.6268.
[17] H. Yoel, N. Sinaga, B. Yunianto, and M. F. Soetanto, "Heat Transfer Intensification by Means of Convex-Strip Around Tube in Fin and Tube Heat Exchanger with Field Synergy Principle," *Int. J. Heat Technol.*, vol. 40, no. 4, pp. 1069–1078, 2022, doi: 10.18280/ijht.400425.
[18] A. Aziz, P. D. Rey, P. Studi, T. Mesinfakultas, S. Dan, and T. Universitas, "DESAIN DAN RANCANG BANGUN ALAT PENUKAR KALOR (HEAT EXCHANGER) JENIS SHELL DAN TUBE," vol. 03, no. 1, pp. 53–60, 2021.
[19] Farel H. Napitupulu :, "Rancang Bangun Alat Penukar Kalor Shell And Tube Dengan Satu Laluan Cangkang Dan Dua Laluan Tabung Sebagai Pemanas Air TALENTA Conference Series Rancang Bangun Alat Penukar Kalor Shell And Tube Dengan Satu Laluan Cangkang Dan Dua Laluan Tabung Sebagai Pem," vol. 1, no. 2, 2018.
[20] R. Nanda and N. Ruhyat, "CFD Study on Wire Mesh Inserts Enhancing Heat Transfer in Double Pipe Heat Exchanger," vol. 9, no. 1, pp. 36–49, 2025.
[21] A. Ponikarov, "Modeling of heat exchangers in ANSYS CFX for the digital twins development," vol. 03021, 2024.
[22] M. N. Ramli and N. Mustaffa, "RESEARCH PROGRESS IN MECHANICAL AND RPMME Efficiency Analysis of Full Rotation Counter Flow of Shell and Tube Heat Exchanger using CFD Tool," vol. 5, no. 1, pp. 444–451, 2024.
[23] W. M. Rosni, A. Adam, M. H. Jumaidi, and E. F. Gornica, "Double Straight Tube Counter-Flow Heat Exchanger for Optimum Heat Transfer by Numerical Simulation," vol. 6, no. 2, pp. 1–9, 2024.
[24] B. Jalaali and E. Kumolosari, "Simulasi aliran dua fase pada campuran air-minyak di pipa horizontal dengan parameter termal," *Angkasa J. Ilm. Bid. Teknol.*, vol. 13, no. 2, pp. 113–122, 2021, doi: 10.28989/angkasa.v13i2.1042.
[25] C. Suárez, A. Iranzo, J. A. Salva, E. Tapia, G. Barea, and J. Guerra, "Parametric investigation using computational fluid dynamics of the HVAC air distribution in a railway vehicle for representative weather and operating conditions," *Energies*, vol. 10, no. 8, 2017, doi: 10.3390/en10081074.
[26] P. P. Jati and A. Widyaparaga, "Simulasi CFD Dinamika Kecepatan Gelombang Aliran Stratified Wavy Dua Fasa Minyak-Air pada Pipa Horizontal," *J. Mech. Des. Test.*, vol. 3, no. 1, p. 1, 2021, doi: 10.22146/jmdt.56417.
[27] E. I. Epelle and D. I. Gerogiorgis, "A multiparametric CFD analysis of multiphase annular flows for oil and gas drilling applications," *Comput. Chem. Eng.*, vol. 106, pp. 645–661, 2017, doi: 10.1016/j.compchemeng.2017.08.011.
[28] J. Zhong, Y. Wang, M. Li, G. Pei, and S. Tang, "Heat transfer characteristics of the fin-tube three-fluid

heat exchanger in cold warehouse with cold storage," *Energy*, vol. 347, no. October 2025, p. 140362, 2026, doi: 10.1016/j.energy.2026.140362.

[29] S. Edhy *et al.*, "Results in Engineering Computational fluid dynamic simulation of earth air heat exchanger : A thermal performance comparison between series and parallel arrangements," *Results Eng.*, vol. 24, no. September, p. 102932, 2024, doi: 10.1016/j.rineng.2024.102932.

LOGIC
Journal of Engineering Design and Technology
Vol. 26 No. 1 March 2026 ; p. 48 - 60

p-ISSN : 1412-114X
e-ISSN : 2580-5649
http://ojs2.pnb.ac.id/index.php/LOGIC

PROTOTYPE DESIGN OF BATTERY CHARGING SYSTEM WITH THE USE OF REPEATED WATER CYCLE AT PICOHIDRO POWER PLANT

1) Department of Electrical Engineering, Faculty of Science and Engineering, Nusa Cendana University, Kupang, Indonesia

Corresponding email [1)*] :
Frans.likadja@staf.undana.ac.id

Marianus Nofu [1)], Frans J. Likadja [1)*], Almido H. Ginting [1)]

Abstract. Pico Hydro Power Plants are small-scale hydropower systems with capacities below 5 kWs that have significant potential as renewable energy sources, particularly in remote areas. However, their implementation is often constrained by fluctuations in water discharge during the dry season, which lead to a decline in system performance. This study aims to design and experimentally evaluate a prototype battery charging system utilizing a repeated water cycle in a Pico Hydro Power Plants to enhance energy supply sustainability. The experimental method was employed by developing a system consisting of a water pump, Pelton turbine, DC generator, smart valve, solar charge controller (SCC), time relay, solar panels, and batteries as energy storage. Experimental testing was conducted by analyzing generator output under various water head and discharge conditions and comparing it with the pumped water discharge within a closed-loop cycle. The results indicate that at a head of 3.9 m, the generator produced an output of 1.7 V and 2.4 A, resulting in a battery charging time of 22.7 hours, whereas at a higher head of 5.42 m, the charging time was reduced to 11.01 hours. In addition, the solar panel system was able to supply the initial load during the system startup process before the pico hydro system is fully operated. Although the proposed system still exhibits limitations in charging time efficiency, the prototype demonstrates good conceptual and functional system integration, indicating strong potential for further development through design optimization to improve overall system efficiency and performance.

Keywords : Picohydro Power Plant, *Water Pump, Smart Valve, Solar Panels, Pelton Turbine, DC Generator, Relay Time, Battery*

1. INTRODUCTION

The increasing demand for sustainable energy and the growing awareness of environmental degradation have accelerated the global transition from fossil-based energy sources to renewable energy technologies [1], [2]. Conventional fossil fuels are associated with significant environmental impacts, including air pollution, greenhouse gas emissions, and long-term ecological degradation [3]. Consequently, renewable energy systems are increasingly promoted as environmentally friendly alternatives capable of supporting sustainable development.

Despite their advantages, renewable energy sources usually had challenges related to intermittency and resource availability [4]. Solar photovoltaic systems experience power fluctuations due to weather conditions and diurnal cycles [5], geothermal power plants are constrained by high capital costs, regulatory limitations, and location-specific requirements [6], while conventional hydropower systems are often suffer from reduced water discharge during dry seasons. These limitations are inhibitting the continuity and reliability of renewable energy supply, particularly in remote or off-grid areas.

Pico-hydropower plants represent a promising solution for decentralized electricity generation due to their simple construction, low environmental impact, and suitability for small-scale applications [7], [8]. However, the performance of pico-hydropower systems is highly dependent on continuous water availability. During periods of low discharge, such as the dry season, power generation capability decreases significantly, limiting their effectiveness as a reliable energy source [9]. Previous studies on pico-hydropower systems have predominantly focused on turbine design optimization [10], [11], electrical performance enhancement [12], [13], or hybridization with other renewable sources while relatively,only a little attention has been given to addressing water availability constraints through integrated system-level approaches.

To address this research gap, this study proposes a prototype pico-hydropower system employing a repeated water cycle combined with battery energy storage and time-based control. The proposed system utilizes two reservoirs with different elevations, an automatic valve, and a water pump to circulate water continuously in a closed-loop configuration. A time-based control strategy is implemented to regulate the alternating operation of the pump and turbine, ensuring that energy consumption and energy generation do not occur simultaneously. This approach aims to enhance operational continuity and improve energy sustainability, particularly during periods of limited natural water discharge.

Therefore, the objective of this study is to design and experimentally evaluate the performance of a battery charging system for a pico-hydropower plant using a repeated water cycle. The evaluation focuses on system feasibility, operational continuity, and electrical performance under varyated head and water discharge conditions.

2. METHODS

This study was conducted by designing and experimentally testing a pico-hydropower plant prototype based on a repeated water cycle system. The system was designed to utilize water energy in a circulatory manner, in which the generator output was used to supply electrical loads during nighttime operation while simultaneously recharging the battery as an energy storage. Experimental testing was carried out to evaluate system performance under specific head and water discharge conditions.

The system consisted of a solar panel, solar charge controller (SCC), battery, water pump, Pelton turbine, DC generator, automatic valve (smart valve), CN101A digital time relay, double time delay relay (TDR) modules, a buck–boost DC converter, and a diode for unidirectional current protection. The DC generator used in this study had a nominal power rating of 250 watt with an operating voltage of 12 Volt DC, selected according to the characteristics of small-scale pico-hydropower systems and the experimental conditions. The Pelton turbine converted the kinetic energy of the water flow into mechanical energy, which was subsequently converted into direct current (DC) electrical energy by the DC generator. Water flow regulation toward the turbine was controlled using a 12 V DC solenoid valve (smart valve). Energy storage was provided by a 12 V battery with a capacity of 6,5 Ah, while the generator output voltage was regulated using a buck–boost converter before being supplied to the SCC and the load.

The system operated automatically based on time-based control, with the CN101A digital time relay serving as the main control unit. During the initial stage, the solar panel charged the battery through the SCC until a fully charged condition was reached. When the time reached 18:00, the CN101A relay activated the pico-hydropower system and shifted the energy source from the solar panel to the battery to support nighttime operation.

To prevent a simultaneous operation between the pump and the turbine and to improve system efficiency, a time-based control strategy employing two independent time delay relay (TDR) modules was implemented. The first TDR controlled the operation of the water pump, while the second TDR controlled the opening and closing of the automatic valve. During the filling phase, the water pump was activated for 1 minute and 54 seconds to transfer water from the lower reservoir to the upper reservoir, while the automatic valve remained closed to prevent water flow toward the turbine. Conversely, during the discharge phase, the automatic valve was opened for 22 seconds to allow water to flow from the upper reservoir to the Pelton turbine, while the water pump was deactivated. This operating scheme ensured that energy consumption by the pump did not occur simultaneously with the energy generation process of the turbine.

The mechanical energy produced by the Pelton turbine is being converted into DC electrical energy by the generator and utilized to supply the load while simultaneously recharging the battery. A diode was installed to ensure unidirectional current flow and to prevent reverse current from flowing back to the generator. After passing through the turbine, the water was collected in a secondary reservoir and subsequently pumped back to the primary reservoir using a 12 V DC water pump, enabling continuous operation in a closed-loop water cycle until 05:00. At this time, the CN101A relay deactivated the pico-hydropower system, and the system returned to battery charging mode using the solar panel.

The control system applied in this study was classified as an open-loop control system, as it did not utilize feedback sensors such as water level or flow rate sensors. The time-based control approach was selected to simplify the prototype design and to focus the study on evaluating the feasibility and performance of the pico-hydropower system that uses a repeated water cycle concept. Overall system of this pico-hydro power plant can be seen in

Figure 1 below.

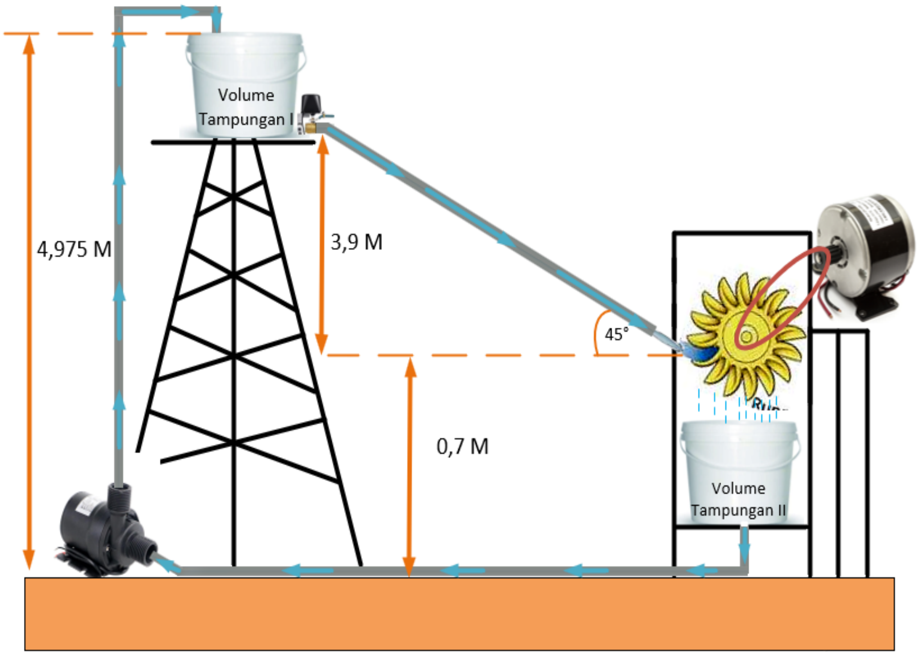

Figure 1. Building model of a picohydro power plant with repeated water cycle

3. RESULTS AND DISCUSSION

3.1 Solar Panel Input and Output Analysis

The output power testing of the 30 WP x 2 solar panel was done on May 8, 2025 with the following results:

Table 1. Solar Panels Output

Time	Voltage (V)	Current (A)	Power (Watt)	Sunlight Intensity (LUX)	Temperature (°C)
08:30AM	21,07	0,795	16,75065	65280	27°C
09:00AM	20,88	1,037	21,65256	99690	29°C
09:30AM	20,42	0,297	6,06474	15920	31°C
10:00AM	20,58	2,159	44,43222	175700	31°C
10:30AM	20,69	1,571	32,50399	173100	31°C
11:00AM	20,19	2,671	53,9749	177000	30°C
11:30AM	20,27	2,568	52,05336	182500	30°C
12:00AM	19,67	1,829	35,97643	125600	30°C
12:30AM	19,48	0,43	8,3764	21370	32°C
13:00AM	20,53	1,739	35,70167	170800	32°C
13:30AM	20,83	1,94	40,4102	173800	33°C
14:00AM	19,47	2,093	40,75071	145900	33°C
14:30AM	19,45	1,108	21,5506	92040	32°C
15:00AM	19,61	0,916	17,96276	85230	33°C
15:30AM	19,87	0,758	15,06146	128400	32°C
16:00AM	19,72	0,429	8,45988	81000	32°C
16:30AM	17,12	0,038	0,65056	2823	32°C
Average	19,99	1,316	27,605	112714,88	31,17°C

The measurements were conducted using a photovoltaic panel installed at a fixed tilt angle of 10° and oriented toward the north. The measurement results presented in Table 1 indicate significant power fluctuations within relatively short time intervals. For instance, at 09:00, the output power was recorded at 21.65 W, then dropped sharply to 6.06 W at 09:30, before increasing rapidly to 44.43 W at 10:00. A similar fluctuation pattern was also observed at 12:30, followed by a significant increase at 13:00. This behavior reflects the intermittent nature of photovoltaic power generation under real field operating conditions.

These power fluctuations were not caused by load variations, but were primarily attributed to the variability of solar radiation received by the photovoltaic module. During the morning to late morning period, rapidly moving cloud cover (passing clouds) caused sudden decreases and increases in the solar radiation incident on the panel. This phenomenon is reflected in the measured light intensity data, which also exhibit significant variations over the same period intervals.

It should be noted that the output current of the photovoltaic panel is highly sensitive to changes in solar radiation, whereas the output voltage remains relatively stable. This trend is evident in the measurement data, where extreme power fluctuations are mostly caused variations in current rather than voltage. This observation matched with the theoretical characteristics of photovoltaic modules, in which the output power is directly related to the photocurrent generated by solar radiation.

The observed power fluctuations shows one of the primary challenges of photovoltaic systems, which is their intermittent and unstable nature, which emphasized the need for mitigation strategies to enhance system reliability in practical applications. The data related to the solar panel output can be seen in the graph below:

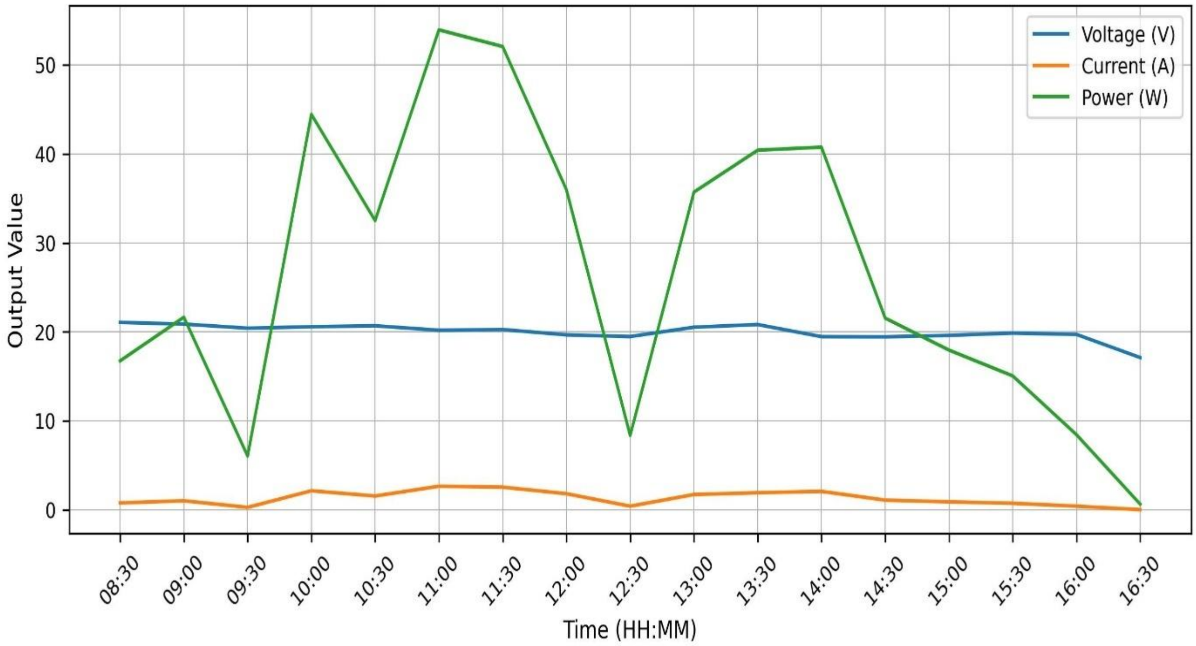

Figure 2. Solar Panels Output Graph

3.2. Energy Testing of Falling Water

3.2.1. Water discharge

Water discharge is the volume of water that passes through a cross-sectional area in one unit of time [14]. In this test, the volume of the water reservoir at the top is equal to the volume of water below. The reservoir used is in the shape of a tube with a radius of 15 cm and a height of 7.5 cm. Based on the existing data, the volume of the reservoir is calculated as follows:

$$V\ \text{Tube} = \pi . r^2 t \qquad (1)$$

Then Tube volume = 3.14 x 152 x 37.5= 0.02649 m^3.

The period required to empty the reservoir in a full state with a height of 3.9 meters is 22 seconds. After calculating the volume and period required for emptying the reservoir, the flow rate can be calculated using the following equation

$$Q = \frac{V}{t};\ \text{or}\ Q = Av \qquad (2)$$

water flow rate(Q) = 0.02649/22= 0.0012 m^3/s.

3.2.2. Water Flow Speed

The speed of the water flow out of the water reservoir depends on the area of the sluice gate used. The sluice gate used in this test is circular in shape with a diameter of 20 mm. The equation for calculating the sectional area of the circle is as follows

$$A = \pi r^2 \tag{3}$$

Then the area of the sluice gate is:
A = 3.14 x 10 x 10= 0.000314 m^2.
After determining the area of the sluice, the flow speed can be calculated based on the following equation:

$$v = \frac{Q}{A} \tag{4}$$

the value of the water flow speed is:

0.0012/0.000314= 3.8216m/s

The flow speed on a nozzle with a diameter of 15mm can be calculated using the principle of continuity:

$$\mathrm{v_1 A_1 = v_2 A_2} \tag{5}$$

V2 = 0.001199/0.000176 = 6.812m/s

3.2.3. Water Power Analysis

The power generated by the flowing water can be calculated using the following equation:

$$\mathrm{P = \rho\, g\, Q\, H} \tag{6}$$

P = 1000 x 9,8 x 0,0012 x 3,9 = 45,864 Watt

3.3. Turbine and Generator Analysis

3.3.1. Generator Analysis

This test is an experiment on a DC generator to see the output. In this test, a torque turbine transmission system was used using belts and pully. Before conducting the test, an analysis was carried out to see the amount of power that can be generated by the generator using equation 2.4 with the following analysis results:

$$\mathrm{P = \rho.g.Q.H.\eta g.\eta t} \tag{7}$$

P = 1000 x 9,8 x 0,0012 x 3,9 x 0,85 x 0,78 = 0,0304 kWatt

The output of the generator this time is 1.7 Volts and also 2.4 A. The output power itself can be calculated as follows

P = V.I = 1,7 x 2,4 = 4,08 Watt.

$$\eta = \frac{P\ out}{P\ in} \times 100\% \tag{8}$$

$$\eta = \frac{4{,}08}{45{,}86} \times 100\% = 8{,}9\%$$

Based on the calculation results, the overall system efficiency is relatively low, reaching only 8.9%. This value indicates that several aspects of the system are contributing to the poor energy conversion performance. These aspects include the generator characteristics, the mechanical energy transmission system between the turbine and the generator, and the turbine performance itself.

The low generator output voltage of 1.7 V indicates that the generator is not operating at its optimal rotational speed. In a pico hydro power generation system, the generator performance is strongly influenced by rotational speed (RPM). In principle, the magnitude of the electromotive force (EMF) generated is proportional to the rotor speed. If the RPM is low, the generated voltage will also be low. This condition suggests a possible mismatch between the generator specifications and the relatively low head condition of 3.9 meters. The generator used likely requires a higher rotational speed to reach its nominal voltage.

Furthermore, the mechanical transmission system using a belt and pulley plays an important role in determining the final rotational speed delivered to the generator. If the pulley ratio is not designed to significantly increase the RPM, the turbine rotation will not be sufficient to meet the generator’s speed requirements. An inadequate transmission ratio can cause the generator to operate far below its maximum efficiency point, resulting in low electrical power output.

Under a head condition of 3.9 meters, the system falls into the low-to-medium head category. Therefore, the selection of turbine type becomes a critical factor. Pelton turbines are generally more effective for higher head applications, whereas for low-head conditions, crossflow or propeller turbines tend to be more suitable because they can utilize relatively low pressure and discharge more efficiently. If the selected turbine type is not well matched to the available head and discharge characteristics, the conversion of water potential energy into mechanical shaft energy will not occur optimally.

Thus, the low overall efficiency is not caused by a single factor, but rather by the cumulative energy losses occurring in the turbine, mechanical transmission system, and generator. Optimization of these three components has significant potential to improve the overall system performance

For comparison, tests were carried out using different discharges and heights to see the output voltage and current coming out of the generator. The test results are shown in the table 2:

Table 2. Table of Generator Output At Different Heights and Discharges

Height	Water Discharge	Voltage	Current
3,9 m	0,0008	0,626 V	0,776 A
3,9 m	0,0012	1,7 V	2,4 A
5,4 m	0,0012	2,5 V	2,973 A

3.3.2. Turbine Analysis

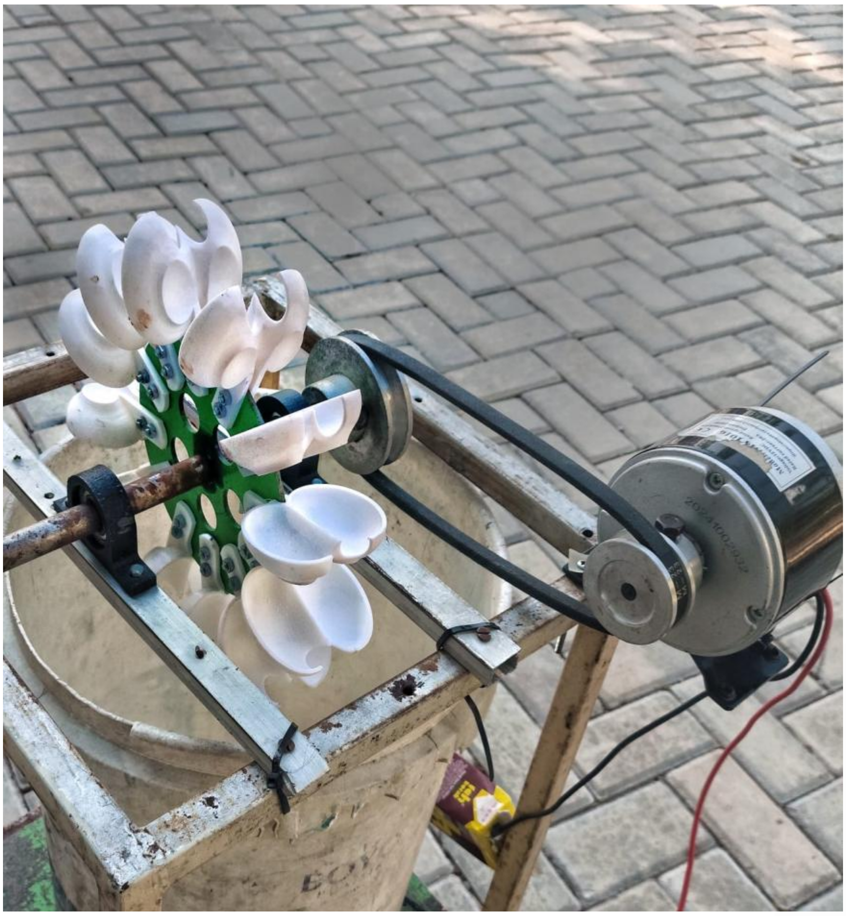

Figure 3. Turbine & Generator DC

In this study, a pelton turbine with 10 spoons was used like figure 3. The transmission system used is 3.5 inches on the turbine and 2 inches on the generator. Here's the Turbine Analysis:

A. Turbine Power

$$Pt = \rho.g.Q.H.\eta t \tag{9}$$

Pt = 1000 x 9,8 x 0,0012 x 3,9 x 0,85 = 0,03898kWatt

B. Speed Type of Turbine

$$n_s = n \cdot \frac{P^{\frac{1}{2}}}{H^{\frac{5}{4}}} \tag{10}$$

n = 458,3 rpm

P = V x I = 1,7 x 2,4 = 4,08 Watt = 0,00408 kW

$\sqrt{P} = \sqrt{0{,}00408} = 0{,}0639$

$N_s = \frac{458{,}3\ x\ 0{,}0639}{5{,}49} = 5{,}34$

Based on the calculation results, the specific speed (Ns) obtained is 5.3. This value is considered very low when compared to the general classification of water turbines. Theoretically, turbines with low specific speed values fall into the impulse turbine category, which are typically designed for high-head and low-discharge conditions. Therefore, the obtained Ns value indicates that the operating characteristics of the system tend to resemble those of a high-head impulse turbine.

However, the actual system condition only provides a head of 3.9 meters, which falls into the low-to-medium head category. This mismatch is an important indication that the turbine is not operating under optimal design conditions. Physically, the very low Ns value results from the combination of low output power (4.08 W) and relatively low rotational speed (458.3 rpm) compared to the available head. In fact, with a theoretical water power potential of approximately 45.9 W, the system should be capable of producing higher mechanical power and rotational speed if the energy conversion process were operating efficiently.

The low Ns value indicates that the water energy is not being fully converted into mechanical shaft power. This condition may be caused by several factors, such as a turbine design that is not well suited for low-head conditions, incomplete energy absorption by the turbine blades, or generator loading that restricts the increase in rotational speed. As a result, the mechanical power transmitted to the generator reduced, leading to low voltage and electrical power output.

Thus, the specific speed value of 5.3 does not merely classify the turbine characteristics, but also serves as an indicator that the system is operating far from its optimal operating point. The mismatch between turbine characteristics, available head conditions, and the loading system contributes significantly to the overall low system efficiency of 8.9%.

The test results with different discharges and altitudes for comparison in looking at turbine power and also the type speed of the test conducted are shown in table 3:

Table 3. Turbine Power Comparison Table And Type Speed At Different Discharge And Height

Height (m)	Water Discharge	Power (kW)	Speed Type Of Turbine
3,9	0,0008	0,000486 kW	1,54
3,9	0,0012	0,00408 kW	5,34
5,4	0,0012	0,00743	7,5

3.4. Cross-Section Pipe Analysis

The type of pipe used in this study is a 1/2 dim pvc pipe with a diameter of 18mm. 2 cross-sectional pipes are used, which are a cross-section of water falling towards the turbine and the pipe connected to the pump. Here are some analyses based on the cross-sectional pipe used

3.4.1. Reynold Number

If it is known that the diameter of the reservoir pipe used is 20mm = 0.02m and the kinematic viscosity value of water in a temperature of 30° = 0.804 x 10-6, as well as the water flow velocity that has been calculated beforehand, then by using the equation of 2.25, the value of the Reynolds number can bee calculated as follows [15]:

$$Re = \frac{VD}{\gamma} \tag{11}$$

Re = 3,8216 x 0,02 / 0,804x10-6 = 9506,46

3.4.2. Mayor Losses

Major losses or losses of water friction with pipe walls need to be taken into account to see how much energy is lost [16]. To determine the magnitude of the loss due to friction or head major, we can used the following analysis:

$$H_{L(Mayor)} = f\,\frac{lv^2}{D.2.g} \qquad (12)$$

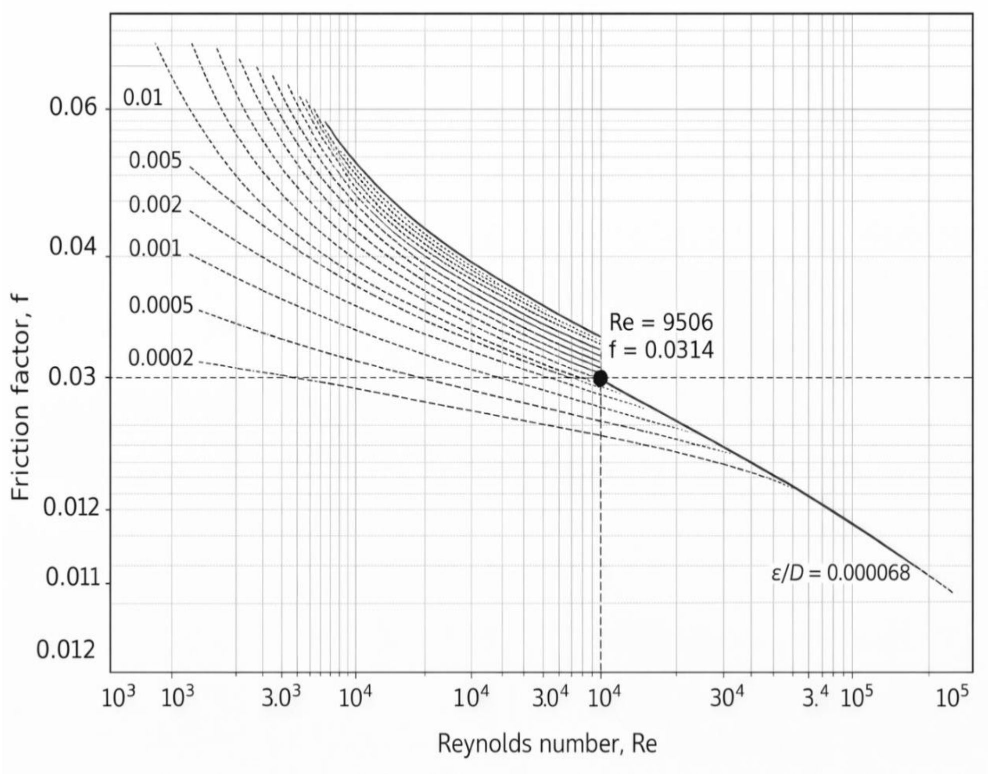

Figure 4. F value at the Moddy Chart cut-off point

Based on the image 4, the cut-off point representing the value of f is 0.0314. The value of Major losses is:

$$H_l = 0{,}0314\ x\ \frac{3{,}9\ x 3{,}8216\ ^2}{0{,}02\ x\ 2\ x\ 9{,}8} = 4{,}56\ m$$

3.4.2. Minor Losses

Minor losses are head losses caused by pipe turning, pipe shrinkage and the presence of nozzles. With turns, reductions and nozzles, it will affect the water power used [17]. To find out the magnitude of minor losses, we can used the following analysis:

$$H_{L(Minor)} = K\,\frac{v^2}{2g} \qquad (13)$$

A. Minor Losses due to 45° turns

With the value of the minor losses coefficient 45° elbow= 0,4. The value of $H_{L(Minor)}$=

HL= 0,4 x (1,512/2 x 9,8) = 0,0465 m

B. Minor Losses Pipe to Tank

With the value of the minor losses coefficient Pipe to Tank= 1. The value of $H_{L(Minor)}$=

HL= 1 x (1,512/2 x 9,8) = 0,1163 m

C. Minor Losses Tank to Pipe

With the value of the minor losses coefficient Tank to Pipe= 0,5. The value of HL(Minor)=

HL= 0,5 x (1,512/2 x 9,8) = 0,0581m

3.5. Cycle of Ups and Downs of Water

To maintain the sustainability cycle of the water cycle continuously, it is necessary to pay attention to several things, including:

3.5.1. Pump Capacity and Pressure

In order to maintain the water sustainability cycle, the water discharge pumped from the bottom to the top is sufficient to compensate for the falling water discharge. Also, the pump pressure must also be considered

3.5.2. Loss of Pressure

The pressure loss is related to major and minor losses that will be analyzed later. Friction of the water flow with the pipe, the turn of the pipe or the overshok for a change in size can increase the possibility of pressure loss. One thing that should not be forgotten is the size of the pipe, which would be better balanced to match the water discharge fluctuations.

3.5.3. Control System

Integrated automatic control in regulating the pump, as well as the sluice gate is needed to maintain the stability of the water discharge in the cycle. Figure 5 illustrates the condition when the pico-hydropower system begins its operation. At this stage, the energy stored in the battery is used to supply the entire control circuit and system loads. The system operation is regulated by the CN101A digital time relay, which works as the main timer controller. When the time reaches 18:00, the CN101A relay automatically activates the pico-hydropower system and ensures that the energy source is switched to the battery to support nighttime operation.

To prevent simultaneous operation of the pump and the turbine and to improve overall system efficiency, a time-based control strategy was implemented using two independent Time Delay Relay (TDR) modules. The first TDR module controls the operation of the water pump, while the second TDR module regulates the opening and closing of the automatic valve (solenoid valve).

The system operates in two primary phases: the filling phase and the discharge phase. During the filling phase, the water pump is activated for 1 minute and 54 seconds to transfer water from the lower reservoir to the upper reservoir. During this period, the automatic valve remains closed to prevent water from flowing toward the turbine. Consequently, electrical energy is consumed solely for the pumping process, and no power generation occurs.

Conversely, during the discharge phase, the pump is deactivated and the automatic valve is opened for 22 seconds. Under this condition, water flows from the upper reservoir to the Pelton turbine, thereby generating electrical energy. This operating scheme ensures that energy consumption by the pump does not occur simultaneously with the turbine’s power generation process. The time-sequenced operation prevents load conflict and enhances the overall efficiency and operational stability of the system. The Charging process with generator can be seen in the figure 6.

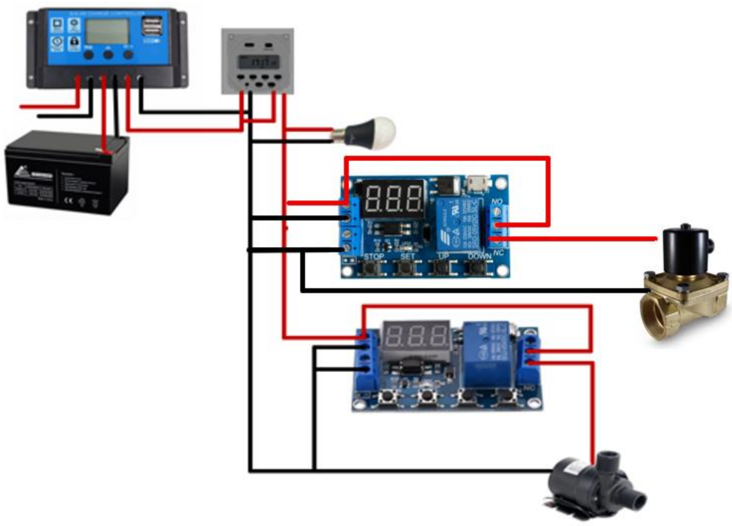

Figure 5. Control System In Load Manuvering

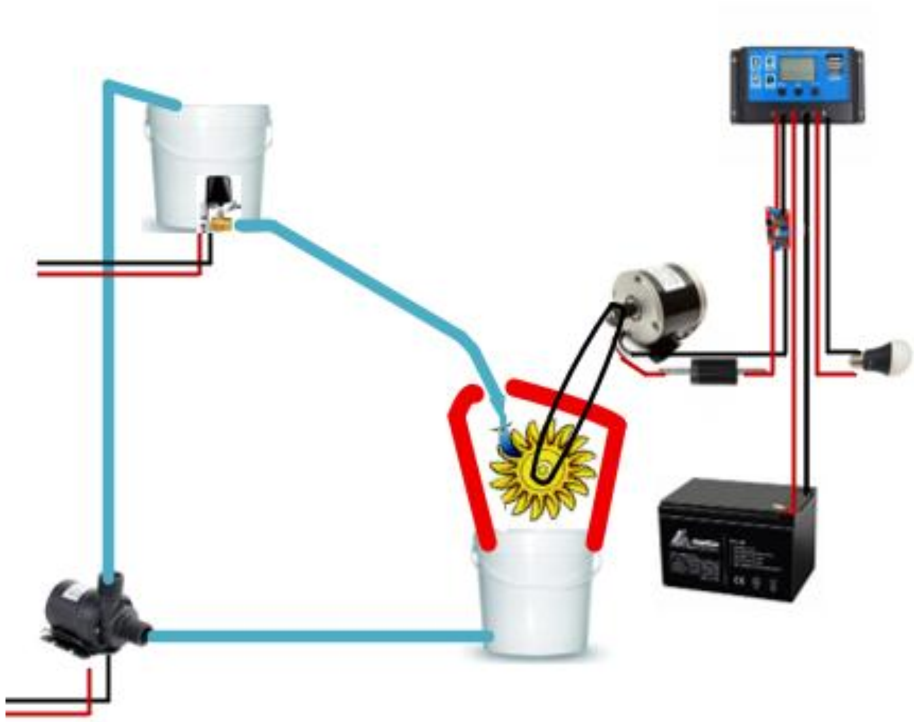

Figure 6. Charging with generator

3.6. Battery Charging Time Analysis

First, the battery discharge process is carried out to see the battery's ability to discharge the load. It is discharged for 6 hours using the load of the DC Pump without increasing the water with variable current between 0.313 A to 0.347 with the data in the table 4.

Table 4. Discharge Battery

Time	Current (A)	Voltage Battery (V)
08:15	0.313	12.58
09:00	0.33	12.48
09:45	0.347	12.36
10:30	0.32	12.22
11:15	0.34	12.1
12:00	0.325	11.98
12:45	0.313	11.9
13:30	0.33	11.84
14:15	0.347	11.8

After the battery discharge process is carried out to the battery voltage of 11.8V (SoC = ±30%), testing is carried out by carrying out the battery charge process.

3.6.1. Charging battery with solar panels

This process occurs during the day where the battery is charged first using a 2x30 WP solar panel. The charging process is shown in the table 5:

Table 5. Charging Baterry With Solar Panel

Voltage Baterry(V)	Current(A)	(W)	Charging Time
11.67	2.55	29.7585	13:00
11.8	2.49	29.382	13:11
11.92	2.6	30.992	13:23
12.03	2.5	30.075	13:34
12.15	2.58	31.347	13:45
12.28	2.45	30.086	13:56
12.38	2.6	32.188	14:08
12.42	2.42	30.0564	14:13
12.5	2.45	30.625	14:23
12.64			14:42

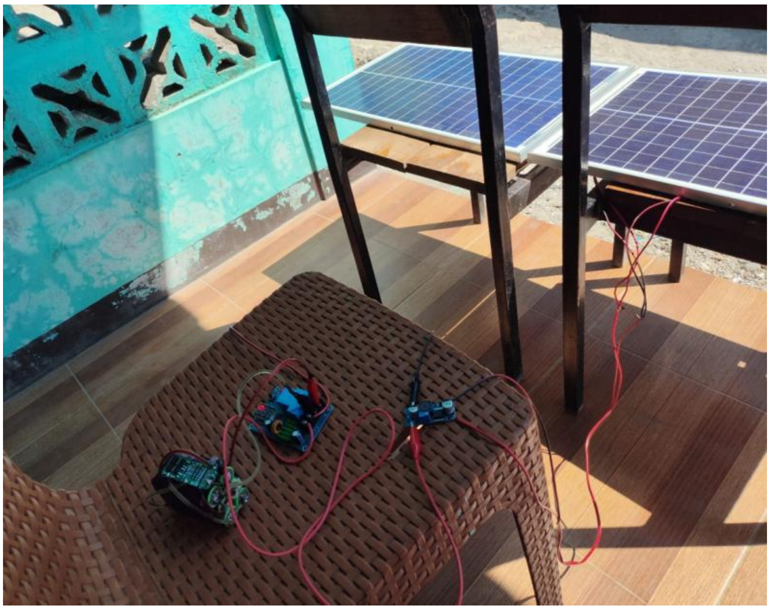

Figure 7. Charging Battery

3.6.2. Load maneuvering

When the time shows 18.00, the battery load turns on when the CN101A time relay starts to activate so that the load maneuver process from the solar panel to the water generator occurs. The maneuver begins with the pump raising water from the lower reservoir to the top by using the energy from a fully charged battery, which when the water rises to the upper reservoir the water will flow from the water reservoir through the smart valve to the cross-sectional pipe and then fall into the pelton turbine. For the pump and smart valve are controlled using a time delay relay (TDR).

3.6.3. Charging battery with Generator

2 tests were carried out at different heights to see the output of the generator to charge the battery with the following results:

A. Generator output at height of 3.9 m
   - Generator Voltage: 1,6 V – 1,7 V
   - Maximum Voltage of Generator: 1,767 V

- Generator current: 2,25 A – 2,42 A
- Peak Current: 2,427 A

Because the voltage is too low, a step up module is needed which is supported by the concept of power retention to get a charging voltage of 13.8 volts. In the use achieve the charging voltage is as follows:

$$P = V.I \tag{14}$$

P = 1,7 x 2,4 = 4,08 Watt

After getting power, we can analyze how much current can be used for charging, with the following analysis:

$$P = (V.I)\eta \tag{15}$$

I = (4,08/13,8) x 0,97 = 0,286 A

After the large charging current is obtained, the charging time, by [18] can be analyzed as follows:

$$h = \frac{Ah}{I} \tag{16}$$

h = 6,5/0,286 = 22,727 H

B. Generator output at height of 5.4 m

- Generator Voltage: 2,5 V - 2,6 V
- Maximum Voltage of Generator: 2,635 V
- Generator current: 2,9 A – 3,01 A
- Peak Current: 3,01 A

Because the voltage is too low, a step up module is needed which is supported by the concept of power retention to get a charging voltage of 13.8 volts. In the use achieve the charging voltage is as follows:

$$P = V.I$$

P = 1,635 x 3,1 = 7,931 Watt

After getting power, we can analyze how much current can be used for charging, with the following analysis:

$$P = (V.I)\eta$$

I = (7,931/13,8) x 0,97 = 0,59 A

After the large charging current is obtained, the charging time can be analyzed as follows:

$$h = \frac{Ah}{I}$$

h = 6,5/0,59
h = 11,01 H

4. CONCLUSION

This study successfully designed and implemented a time-based controlled pico-hydropower generation system integrated with a solar panel and battery as an energy storage unit. The system operation was controlled using a CN101A digital time relay as the main timing controller, along with two Time Delay Relay (TDR) modules to alternately regulate the operation of the water pump and the automatic valve.

The two-phase control strategy, consisting of a filling phase and a discharge phase, effectively prevented simultaneous operation of the pump and the turbine, ensuring that energy consumption and power generation did not occur at the same time. The system operated automatically according to the predefined time sequence, demonstrating the successful implementation of time-sequencing-based energy management.

However, experimental results indicate that the overall system efficiency remains relatively low at 8.9%. The specific speed (Ns) value of 5.3 suggests that the turbine's operating characteristics tend to resemble those of a high-head impulse turbine, while the actual system operates at a head of 3.9 meters, which falls within the low-to-medium head category. The mismatch between turbine characteristics, mechanical transmission system, and generator specifications is identified as the primary factor contributing to the low energy conversion performance.

Therefore, further optimization is required in terms of turbine selection, mechanical transmission ratio, and generator characteristics to better match the available head and discharge conditions. Future development is expected to improve system efficiency and enhance the feasibility of small-scale pico-hydropower systems with automated control strategies.

5. REFERENCES

[1] P. Lingkungan and Y. Berkelanjutan, "Green_Accounting_DAMPAK_TRANSFORMASI_ENERGI_HIJAU_," vol. 6, no. 1, pp. 1–9, 2025.

[2] B. A. S. Putri, G. V. A. Saroy, and R. K. Rajib, “Pendekatan peran hukum dalam mendorong transisi energi terbarukan,” Jurnal Multidisiplin Ilmu Akademik, vol. 1, no. 3, pp. 230–235, 2024, doi: 10.61722/jmia.v1i3.1402.

[3] H. Tjiwidjaja and R. Salima, “Dampak energi fosil terhadap perubahan iklim dan solusi berbasis energi hijau,” Jurnal Wilayah, Kota dan Lingkungan Berkelanjutan, vol. 2, no. 2, pp. 166–172, 2023, doi: 10.58169/jwikal.v2i2.625.

[4] F. M. Noor and A. F. Rahman, “Studi penerapan integrasi sumber energi baru terbarukan dengan smart grid dan sistem pengendalian SCADA,” Proceedings of the Industrial Research Workshop and National Seminar, vol. 14, no. 1, pp. 526–532, 2023, doi: 10.35313/irwns.v14i1.5440.

[5] Siregar et al., “Pengaruh penggunaan teknologi superconducting magnetic energy storage (SMES) dalam sistem pembangkit energi listrik berbasis tenaga surya,” Jurnal Media Informatika, vol. 6, no. 2, pp. 1545–1550, 2025, doi: 10.55338/jumin.v6i2.6533.

[6] E. Elfina and Z. Judge, “Kepastian hukum jaminan investasi energi terbarukan panas bumi dalam pengembangan energi di Indonesia,” Jatijajar Law Review, vol. 2, no. 2, pp. 82–98, 2023, doi: 10.26753/jlr.v2i2.1156.

[7] B. Edi, S. Atifoqkymin, and M. Fitri, “Tinjauan literatur: kinerja turbin screw Archimedes pembangkit listrik tenaga pikohidro (PLTPH) pada aliran air dengan head rendah,” Al-Jazari: Jurnal Ilmiah Teknik Mesin, vol. 9, no. 2, pp. 102–113, 2024, doi: 10.31602/al-jazari.v9i2.15853.

[8] D. Hamdani and M. L. Edypoerwa, “Study and design of picohydro power plant for low-head and low-flow application,” ELKOMIKA: Jurnal Teknik Energi Elektrik, Teknik Telekomunikasi, dan Teknik Elektronika, vol. 13, no. 2, pp. 200, 2025, doi: 10.26760/elkomika.v13i2.200.

[9] M. I. Malik, W. Widyantoro, A. I. Rabbika, Y. Yanti, and Y. Yadi, “Analisis potensi pembangkitan listrik tenaga nano hydro di saluran irigasi Desa Cintaraja Tasikmalaya,” Jurnal Teknik Elektro UNIBA (JTE UNIBA), vol. 9, no. 1, pp. 540–547, 2024, doi: 10.36277/jteuniba.v9i1.393.

[10] H. Haryadi, A. Mahmudi, Sugianto, and D. Setiawan, “Studi pengaruh debit dan jenis runner terhadap efisiensi turbin vorteks PLTPH,” Jurnal PERMADI: Perancangan, Manufaktur, Material, dan Energi, vol. 5, no. 2, pp. 66–77, 2023, doi: 10.52005/permadi.v5i2.121.

[11] C. Flow, “5) , 1-5),” vol. 6, pp. 16–25, 2024.

[12] U. Amri, “Rancang bangun pembangkit listrik tenaga piko hidro (PLTPH) (analisis daya beban output pada generator),” Jurnal Tektro, vol. 5, no. 1, pp. 100, 2021, doi: 10.30811/tektro.v5i1.2803.

[13] U. Amri, Z. Zulfikar, and M. Mahalla, “Rancang bangun pembangkit listrik tenaga piko hidro (PLTPH) (analisis daya beban output pada generator),” Jurnal Tektro, vol. 5, no. 1, pp. 100, 2021, doi: 10.30811/tektro.v5i1.2803.

[14] N. P. V. Fitriyani, “Analisis Debit Air di Daerah Aliran Sungai (DAS),” *Ilmuteknik.org*, vol. 2, no. 2, pp. 1–10, 2022.

[15] M. Dzailani, “Analisis pengaruh sudut belokan terhadap head losses penstock di PLTA Timo 3×4 MW,” 2023.

[16] F. Mujahid, “Pengaruh head losses mayor dan minor pada sistem instalasi turbin Pelton skala mikro,” vol. 1, pp. 1–9, 2021.

[17] A. Minor, L. Alat, U. Aliran, and F. Skala, “Jurnal Dinamis Laboratorium,” vol. 10, no. 2, pp. 7–19, 2022.

[18] Y. N. Hilal, P. Muliandhi, and E. N. Ardina, “Analisa balancing BMS (battery management system) pada pengisian baterai lithium-ion tipe INR 18650 dengan metode cut off,” Simetris: Jurnal Teknik Mesin, Elektro dan Ilmu Komputer, vol. 14, no. 2, pp. 367–374, 2023, doi: 10.24176/simet.v14i2.9852.

LOGIC
Journal of Engineering Design and Technology
Vol. 26 No. 1 March 2026 ; p. 61 - 70

p-ISSN : 1412-114X
e-ISSN : 2580-5649
http://ojs2.pnb.ac.id/index.php/LOGIC

COMBUSTION TEMPERATURE ANALYSIS ON CO EMISSIONS IN A SIMPLE LIGHTWEIGHT BRICK-BASED INCINERATOR

(Case Study in Banjar Mukti, Singapadu Village, Sukawati District, Gianyar)

Made Ardikosa Satrya Wibawa [1)*], I Made Anom Adiaksa [1)], I Made Agus Putrawan [1)], I Wayan Suma Wibawa [1)], Anak Agung Gede Pradnyana Diputra [1)], I Wayan Agus Rantia Dana [1)]

1) Mechanical Engineering Department, Politeknik Negeri Bali, Bukit Jimbaran, Kuta Selatan, Badung, Indonesia

Correponding email [1)*] :
ardikosa_satrya@pnb.ac.id

Abstract. Residual waste management at the community level remains a significant environmental problem, particularly for mixed organic and inorganic waste. The use of a simple incinerator made from lightweight bricks is a practical solution due to its low construction costs and ease of operation. However, incomplete combustion can produce harmful gas emissions such as carbon monoxide (CO). This study aims to analyze the effect of combustion temperature on CO levels produced by a simple three-level incinerator using wood fuel. The incinerator design consists of an ash chamber on the lower level, a wood combustion chamber on the middle level, and a waste combustion chamber on the upper level with a volume capacity of 0.384 m^3. The residual waste burned is 10 kg per cycle consisting of a mixture of organic and inorganic waste. Data collection was carried out 20 times by measuring the combustion temperature and CO levels using a gas analyzer. The results show an inverse relationship between combustion temperature and CO levels. Increasing the combustion temperature results in a more complete oxidation process, resulting in a significant decrease in CO levels. This study demonstrates that controlling combustion temperature is an important parameter in improving combustion efficiency and reducing harmful gas emissions in small-scale incinerators..

Keywords : incinerator, combustion temperature, carbon monoxide, lightweight brick, emission analysis.

1. INTRODUCTION

Waste management is an increasingly complex environmental issue as the population and human activity increase. Non-recyclable residual waste often presents a major challenge due to limited processing facilities, particularly in rural areas or settlements with limited infrastructure. Open burning remains a widely used method for waste reduction due to its practicality and affordability. However, this method has negative environmental impacts due to the harmful gas emissions it produces. [1], [2], [3].

One of the main pollutant gases produced from incomplete combustion is carbon monoxide (CO). CO gas is formed as a result of incomplete oxidation reactions due to limited combustion temperature, oxygen supply, and uneven heat distribution. High CO concentrations can pose a health risk to the public due to its toxic nature and ability to inhibit oxygen distribution in the human body. Therefore, controlling combustion parameters is a crucial aspect in designing an environmentally friendly waste incineration system. [4], [5], [6].

An incinerator is a waste processing technology that works through a thermal combustion process to significantly reduce waste volume. On a community scale, the use of simple incinerators made from lightweight bricks offers considerable potential due to their low construction costs, ease of construction using local materials, and superior heat retention compared to open combustion. Lightweight bricks have thermal insulation properties that help stabilize temperatures in the combustion chamber, potentially increasing combustion efficiency and reducing harmful gas emissions. [7], [8].

Several previous studies have shown that increasing combustion temperature significantly impacts the quality of the combustion products. Higher temperatures tend to result in a more complete oxidation process, thereby reducing CO levels in combustion smoke. However, most research focuses on industrial-scale incinerators or complex combustion systems, while studies on simple, lightweight brick incinerators at a community scale are still relatively limited, particularly in real-world settings. [4], [9], [10]. [1], [11], [12].

In the Banjar Mukti area of Singapadu Village, Sukawati District, Gianyar, residual waste management is still carried out in a simple manner, requiring appropriate technological solutions that are easy to implement and still consider environmental aspects. Based on these conditions, this study was conducted to analyze the effect of combustion temperature on carbon monoxide (CO) levels produced by a simple incinerator made from lightweight bricks with a multi-stage combustion design.

This research is expected to provide a scientific contribution to the development of community-scale incinerator technology and serve as a technical reference for efforts to reduce hazardous gas emissions by controlling combustion temperatures. Furthermore, the research findings are expected to serve as a basis for developing more efficient, safe, and environmentally friendly waste incineration systems at the community level.

This research contributes scientifically to the field of small-scale waste incineration technology by analyzing the relationship between combustion temperature and carbon monoxide (CO) emission levels in a simple lightweight brick incinerator. Scientifically, this study enriches the current limited understanding of community-scale incinerator operational parameters, particularly in simple incinerator designs commonly used in rural areas.

The results are expected to demonstrate that controlling combustion temperature is a key factor in suppressing the formation of CO gas, one of the harmful emissions resulting from incomplete combustion. Therefore, this research can serve as a scientific reference in the development of more efficient, safe, and environmentally friendly waste incineration systems.

The use of lightweight bricks in incinerator construction is essential due to their excellent thermal insulation properties, which enable the system to maintain a more stable combustion temperature. This temperature stability plays a significant role in achieving a more complete combustion process and has the potential to reduce the formation of harmful gas emissions. In addition, lightweight bricks are relatively easy to obtain, cost-effective, and can be applied locally by communities without requiring complex technology. These characteristics make lightweight brick incinerators a practical and appropriate technological solution for community-scale implementation, particularly in areas with limited access to advanced waste management systems.

From a practical perspective, this research is expected to provide direct benefits to the community by offering simple technical guidance on operating incinerators to achieve more optimal combustion conditions and minimize emissions. It also supports community-based waste management initiatives that are safer for the environment and contributes to reducing the negative impacts of open burning practices that are still commonly carried out. Furthermore, the findings of this study can serve as a scientific basis for village governments or environmental managers in designing small-scale waste management systems that are more environmentally friendly.

Overall, this research not only contributes to the advancement of scientific knowledge in the field of waste incineration technology but also demonstrates strong applicability in supporting sustainable environmental management at the community level.

2. METHODS

2.1 Research Location

The research was conducted in Banjar Mukti, Singapadu Village, Sukawati District, Gianyar Regency, Bali. The research location was chosen because it is a residential area that still uses conventional waste burning methods (open burning), making it suitable for the implementation and testing of a community-scale incinerator. The environmental conditions of the research location allow for direct observation of combustion performance with variations in temperature and emissions..

2.2 Incinerator Design

The incinerator used in this study is a simple structure constructed from lightweight bricks with a three-level vertical combustion configuration. This design aims to enhance heat distribution and improve combustion efficiency by functionally separating the combustion zones within the system. The bottom section serves as an ash collection chamber, which functions as both an accumulation area for combustion residues and an air inlet to support the combustion process. The middle section operates as the primary combustion chamber for firewood, which acts as the main heat source, while the top section is utilized as the waste incineration chamber with an effective capacity of 0.384 m³.

The implementation of a multi-level design enables the formation of a natural draft system, allowing airflow to circulate more effectively and resulting in a more stable and uniform combustion process. Lightweight bricks were selected as the primary construction material due to their good thermal insulation properties, which help retain heat within the combustion chamber, as well as their local availability and suitability for small-scale applications [8], [12].

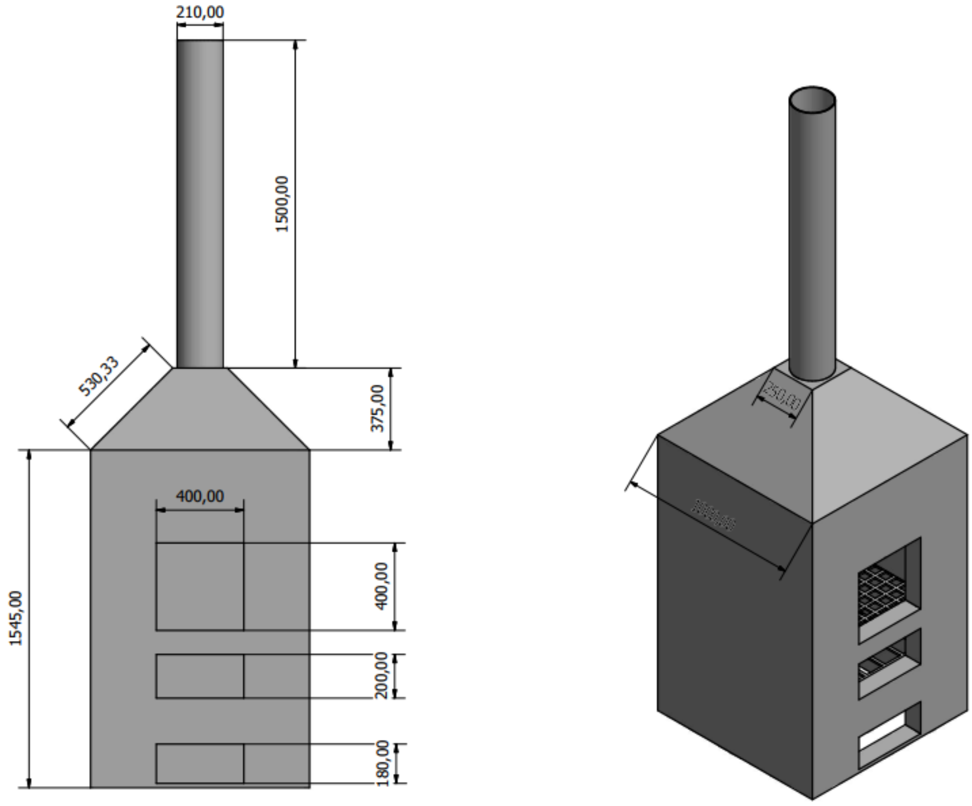

Figure 1. Simple incinerator design made from lightweight bricks

Figure 2. Existing image of a simple incinerator made from lightweight bricks and the combustion process as well as measuring temperature and CO levels.

2.3 Materials and tools

The materials and equipment used in this study include firewood as the primary fuel for combustion and mixed residual waste (organic and inorganic) with a mass of 10 kg for each combustion cycle. A gas analyzer was utilized to measure carbon monoxide (CO) concentration, while a high-temperature thermometer was used to monitor the combustion chamber temperature. A stopwatch was employed to control the data collection intervals. Prior to use, all measuring instruments underwent a simple calibration process to ensure data consistency during the experiment.

Carbon monoxide (CO) concentration measurements were conducted using a portable gas analyzer based on an electrochemical sensor. The device has a measurement range of 0–5000 ppm, with an accuracy of ±5% of the reading and a resolution of 1 ppm. Measurements were taken at the gas sampling point located in the incinerator chimney to obtain representative combustion gas concentrations. The sampling point was positioned approximately 30 cm horizontally from the chimney outlet and at a height of about 1.5 m above ground level. The probe was aligned with the flue gas flow direction to minimize turbulence, and each measurement was carried out for 30–60 seconds until a stable reading was obtained. Data were recorded periodically throughout the combustion process.

Each combustion cycle was performed using 10 kg of waste, with an average operating time ranging from 45 to 60 minutes depending on waste characteristics and flame stability. The combustion process consisted of three stages: an initial ignition phase of approximately 10 minutes, a main combustion phase lasting 30–40 minutes, and a final combustion and initial cooling phase of about 10 minutes. Temperature and CO concentration measurements were primarily recorded during the main combustion phase, as this stage represents the most intensive oxidation process.

The mixed waste used in this study had an average moisture content of approximately 20–30%, determined through initial weighing and simple air-drying based on the physical condition of the material prior to combustion. Moisture content is a critical parameter, as higher moisture levels can reduce combustion temperature and increase CO emissions due to incomplete combustion..

2.4 Research Variables

This study employed combustion temperature as the independent variable and carbon monoxide (CO) concentration as the dependent variable. Several parameters were controlled to ensure experimental consistency, including waste mass (10 kg), fuel type (firewood), combustion chamber volume (0.384 m^3), and environmental conditions during testing. These control variables were maintained constant to ensure that variations in CO emissions were primarily influenced by changes in combustion temperature.

2.5 Testing Procedures

The experimental procedure was conducted systematically, beginning with cleaning the incinerator to remove any residue from previous combustion cycles. Firewood was then placed in the middle combustion chamber and ignited until a stable flame was achieved. Subsequently, residual waste was gradually introduced into the upper combustion chamber to ensure even heat distribution. The combustion process was allowed to continue until the system reached its operating temperature.

Temperature measurements were taken at a consistent observation point to maintain data reliability, while CO concentration was measured at the chimney outlet using the gas analyzer. Data were recorded periodically throughout the combustion process. To obtain representative results, the experiment was repeated 20 times under similar conditions.

2.6 Data Collection Method

Data were collected through direct experimental observation, with temperature and CO concentration measured simultaneously. Each measurement was taken after the combustion process reached relatively stable conditions to avoid the influence of the initial ignition phase. Repeated testing was performed to improve data reliability and reduce experimental errors caused by variations in fuel distribution and waste composition..

2.7 Data analysis

The collected data were analyzed quantitatively to examine the relationship between combustion temperature and CO concentration. A descriptive and trend analysis approach was applied to identify patterns in emission changes as temperature increased. The results were then presented in the form of tables and graphs to facilitate interpretation and discussion.

3. RESULTS AND DISCUSSION

3.1 Experimental Test Results

Based on the characteristics of the lightweight brick incinerator, its waste capacity of 10 kg/cycle, and the recorded combustion temperature range of 220–608°C, firewood requirements can be estimated using a small-scale combustion energy approach. The initial temperature (220–350°C) requires the greatest energy supply to raise the combustion chamber temperature. Once the temperature exceeds approximately 400°C, the waste begins to burn more steadily, reducing the need for additional fuel.

The average firewood requirement is approximately 3–5 kg per combustion cycle. This value is considered efficient for community-scale incinerators because the lightweight brick walls help retain heat, resulting in lower fuel consumption compared to thin metal construction.

Test results show a decreasing trend in CO concentration as combustion temperature increases, indicating more complete combustion. However, evaluating compliance with emission standards requires converting the data to mg/Nm³ and standardized laboratory testing. The total cost of constructing a simple incinerator using lightweight bricks is 7.5 million rupiah.

Table 1. Shows The Results Of Measurements Of Combustion Temperature And CO Levels During Testing.

No	Combustion Temperature (°C)	CO levels (ppm)
1	220	1315
2	242	1298
3	264	1280
4	281	1265
5	302	1247
6	322	1230
7	341	1218
8	365	1201
9	385	1188
10	402	924
11	422	915
12	443	903
13	464	892
14	488	880
15	501	872
16	525	864
17	547	858
18	563	851
19	586	845
20	608	840

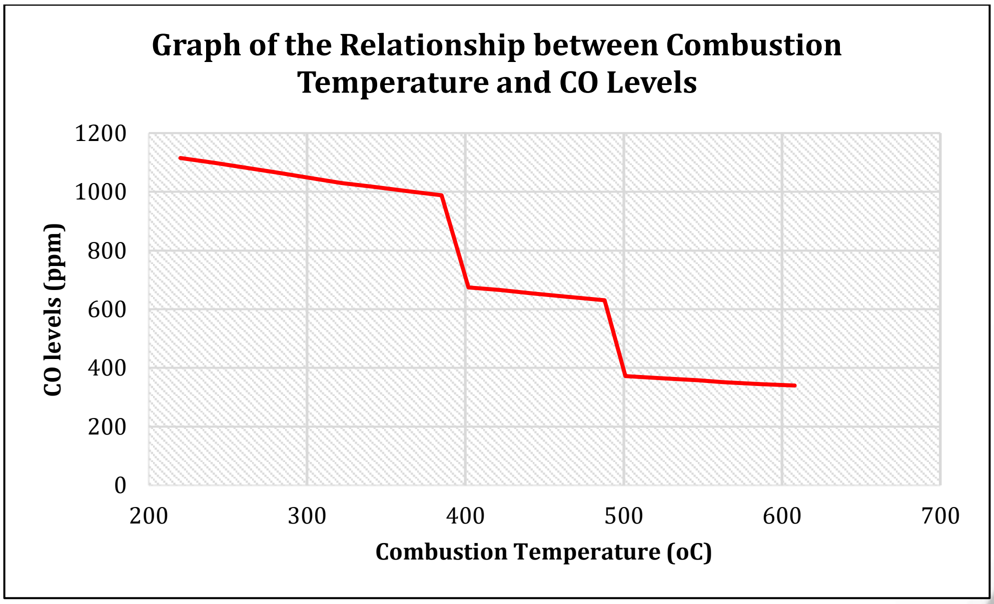

Figure 3. Graph of the Relationship between Combustion Temperature and CO Levels

3.2 Equality

The equation used in combustion analysis is as follows:

Heat energy from combustion:

$$Q = m \ x \ c \ x \ \Delta T \tag{1}$$

with:
Q = heat energy (J)
m = mass (kg)
c = specific heat (J/kg·K)
ΔT = temperature changes (K)

Estimated combustion efficiency:

$$\eta = \frac{T_{actual}}{T_{maks}} \times 100\% \tag{2}$$

dengan:
η = combustion efficiency (%)
T_{actual} = temperature measurement results (°C)
T_{maks} = maximum theoretical temperature (°C)

The test was conducted 20 times, with the main parameters being combustion temperature and carbon monoxide (CO) levels. The measurement results show a variation in combustion temperature from 220°C to 600°C, with a tendency for CO concentration to decrease as the combustion temperature increases.

Table 1 shows that the highest CO values were recorded at low temperatures (220–280°C), while the lowest CO values were obtained at high temperatures (500–600°C). This pattern indicates that combustion performance is significantly influenced by thermal conditions within the combustion chamber.

In general, the experimental results show a negative (inverse) relationship between combustion temperature and CO levels, indicating increased oxidation efficiency at high temperatures.

3.2 Analysis of the Relationship between Combustion Temperature and CO Emissions

Carbon monoxide is a product of incomplete combustion that forms when the carbon oxidation reaction does not proceed completely. At low temperatures, the activation energy of the chemical reaction is not optimally achieved, so the combustion reaction only results in partial oxidation [4],[6] as represented in Equation (3). As the temperature increases, the kinetic energy of the particles increases, resulting in a higher frequency of collisions between molecules. This condition accelerates further oxidation reactions [9],[10] as shown in Equation (4). As a result, the measured CO concentration decreased significantly. This phenomenon is clearly visible in the test data, where increasing the temperature from 300°C to 500°C reduced the CO level by almost 60%. [4], [9], [7].

In addition, high temperatures increase the turbulence of the airflow within the combustion chamber, resulting in a more homogeneous mixture of fuel and oxygen. This increased homogeneity of the mixture contributes to more complete combustion.

$$C + \frac{1}{2}O_2 \rightarrow CO \tag{3}$$

$$CO + \frac{1}{2}O_2 \rightarrow CO_2 \tag{4}$$

3.3 Analysis of Combustion Stages in an Incinerator

During the experimental process, combustion in the incinerator can be classified into three main phases based on temperature characteristics and reaction behavior. In the initial stage, known as the drying phase (temperatures below 250°C), the supplied heat energy is primarily used to evaporate the moisture content present in the waste. At this stage, the oxidation process is still limited, which may lead to unstable combustion conditions and incomplete reactions.

As the temperature increases to the range of 250–400°C, the process enters the pyrolysis phase, during which organic materials begin to thermally decompose into volatile gases. These gases are not fully oxidized due to insufficient temperature and mixing conditions, which can result in the formation of incomplete combustion products.

At temperatures above 450°C, the system reaches the intense combustion phase, where volatile gases undergo more complete oxidation. In this phase, combustion reactions become more stable and efficient, leading to a significant reduction in incomplete combustion products. Therefore, this stage represents the optimum operating condition of the incinerator, where thermal efficiency and emission performance are improved.

3.4 Effect of Multi-Stage Design on Combustion Stability

The three-level configuration of the incinerator plays a significant role in enhancing the thermal stability of the combustion process. The bottom ash chamber functions as both a residue collection area and an air inlet, enabling a natural draft that ensures a continuous supply of oxygen to the combustion zones. The middle chamber, which is used for firewood combustion, serves as the primary heat source and provides a stable and sustained temperature during operation. The generated heat is then transferred upward to the waste combustion chamber through natural convection, promoting more effective thermal utilization.

This structured distribution of combustion zones improves overall system performance by enhancing heat retention in the upper chamber, reducing thermal energy losses, and ensuring a more uniform combustion process. As a result, temperature fluctuations within the incinerator can be minimized, leading to more stable operating conditions. These improvements contribute directly to the reduction of CO emissions observed during the experimental testing.

3.5 Thermal Characteristics of Lightweight Bricks

Lightweight bricks have relatively low thermal conductivity, reducing heat loss to the surrounding environment. This thermal insulation property plays a crucial role in maintaining a high combustion chamber temperature even when the fuel supply is inconsistent. [13], [14], [15], [16], [17], [18].

Good heat retention allows thermal energy to be stored longer in the combustion chamber, allowing the oxidation reaction to continue. This is one of the main reasons why CO levels decrease in the high-temperature phase. [13], [19].

In addition, the use of lightweight bricks also increases operational safety because the outer surface temperature of the incinerator is relatively lower compared to conventional materials.

3.6 Combustion Efficiency Analysis

Based on the data trends obtained, increasing combustion temperatures can be used as an indicator of increased combustion efficiency. At high temperatures, most of the carbon content in the waste is oxidized to CO_2, resulting in a decrease in the CO fraction. [9], [7], [10].

Conceptually, combustion efficiency can be associated with a system's ability to produce maximum heat with minimal emissions. In this study, the temperature range of 500–600°C indicated the most efficient combustion conditions because:

- Stable temperature
- More homogeneous flame
- Low CO emissions
- More complete combustion of residues

3.7 Practical Implications for Waste Management

The research results show that operating a simple incinerator can still produce relatively clean combustion if the operating temperature is maintained within the optimal range. This is important for community-scale applications because:

- Reduce the impact of air pollution
- Increase the efficiency of waste volume reduction
- Improve the safety of the surrounding environment

Thus, temperature control can be used as the main parameter in operating a lightweight brick incinerator on a community scale.

1.8 Comparison of Research Results with Previous Studies

To evaluate the position of the results of this study, a comparison was made with several previous studies that discussed small-scale incinerators, the relationship between combustion temperature and CO emissions, and the use of lightweight brick materials as thermal insulation.

a. Comparison with Small-Scale Incinerator Studies

Several previous studies have shown that the performance of small-scale incinerators is significantly influenced by operating temperature, waste moisture content, and combustion chamber design.

A study by Nyoti et al. on small-scale incinerators showed that high operating temperatures can improve combustion quality and reduce exhaust emissions, while low temperatures produce denser smoke and higher emissions. [20]

The results of this study show a similar pattern, where increasing the temperature from 220°C to 608°C resulted in a decrease in CO concentration from 1315 ppm to 840 ppm. This indicates that the lightweight brick incinerator can achieve combustion performance comparable to that of other small-scale incinerators studied. The results of this study are similar to previous studies in showing that high temperatures increase combustion efficiency and reduce emissions.

b. Comparison of the Relationship between Combustion Temperature and CO Emissions

Other studies on incinerator emission performance have shown that increasing operating temperature significantly reduces combustion gas emissions. Emission evaluation studies on small-scale incinerators report that high temperatures result in more complete combustion and lower CO emissions compared to low-temperature conditions. [21]

Your study showed a significant change when the temperature exceeds approximately 400°C, where CO levels drop sharply (1188 → 924 ppm). This phenomenon indicates the existence of a critical temperature for optimal combustion, the condition where carbon oxidation occurs most completely. The results of this study are more informative because they show a clear temperature transition point, not just a general trend of decreasing CO.

c. Comparison with the Study of Lightweight Bricks as Thermal Insulation

Material studies show that lightweight bricks have low thermal conductivity, making them effective as heat insulation materials. Research on lightweight mortar and materials indicates a thermal conductivity of <0.2 W/(m·K), which contributes to better heat retention. Other studies on lightweight bricks also report that lightweight materials can improve thermal insulation and reduce heat energy loss during the heating process. [22] [23]

In this study, the use of lightweight bricks allowed the combustion chamber temperature to increase steadily to >600°C with relatively low firewood consumption (±3–5 kg/cycle). This demonstrates good thermal insulation performance, preventing energy from being easily lost to the environment. The results of this study are consistent with the literature that lightweight bricks increase thermal efficiency. Practically, the incinerator maintained a stable temperature without additional insulation.

Overall, the results of this study confirm previous findings that increasing combustion temperature contributes to reduced CO emissions. However, this study adds value through the implementation of a lightweight brick incinerator that demonstrates high temperature stability in a simple, community-scale system. Thus, this study not only confirms existing scientific trends but also provides a more relevant, applicable approach for low-cost waste treatment technologies.

4. CONCLUSION

Based on the research results, it can be concluded that combustion temperature has a significant influence on the carbon monoxide (CO) levels produced by a simple incinerator made from lightweight bricks. Increasing the combustion temperature reduces CO concentrations due to a more complete oxidation process. The most effective combustion conditions occur in the temperature range of 500–600°C, where CO emissions are lowest and combustion is more stable.

The multi-level incinerator design improves combustion stability through better heat distribution and air supply, while the lightweight brick material plays a role in heat retention, thus increasing combustion efficiency. The results of this study indicate that temperature control is a key factor in reducing harmful gas emissions in small-scale incinerators.

Overall, a simple incinerator made from lightweight bricks has the potential to be a practical and environmentally friendly waste management solution at the community level. Further research is recommended to evaluate other emission parameters and optimize the air supply system to improve combustion performance.

5. ACKNOWLEDGEMENT

The authors would like to express their gratitude to the community of Banjar Mukti, Singapadu Village, for their support during the research. They also express their gratitude to the Bali State Polytechnic for their academic support and research facilities.

6. REFERENCES

[1] Matee, V.E. and Manyele, S.V. (2015) Performance of a Large-Scale Medical Waste Incinerator in a Referral Hospital. Engineering, 7, 676-690. http://dx.doi.org/10.4236/eng.2015.710059

[2] P.-T. Cai, T. Chen, B. Chen, Y.-C. Wang, Z.-Y. Ma, and J.-H. Yan, “The impact of pollutant emissions from co-incineration of industrial waste in municipal solid waste incinerators,” Fuel, vol. 352, 2023, Art. no. 129027, doi: 10.1016/j.fuel.2023.129027.

[3] Muhammad Bilal Ahmad et al., "Investigation on co-combustion behavior of domestic waste and sewage sludge using TG-FTIR-Py-GC/MS: Thermal behavior and gaseous pollutants emission," *J. Energy Inst.*, vol. vol.118, 2025, doi: https://doi.org/10.1016/j.joei.2024.101933.
[4] J. R. Jian Tang, Xiaoxian Yang, Wei Wang, "Evaluating Municipal Solid Waste Incineration Through Determining Flame Combustion to Improve Combustion Processes for Environmental Sanitation," *Sustainability*, vol. 17, 2025, doi: https://doi.org/10.3390/su17198872.
[5] H. Zongkuan Liu, Zhou, Lei Zhong, Lijia Wei, "Enhanced combustion of ammonia engine based on novel air-assisted pre-chamber turbulent jet ignition," *Energy Convers. Manag.*, vol. 276, 2023, doi: https://doi.org/10.1016/j.enconman.2022.116526.
[6] Yuxin Chen et al., "Interval energy flow calculation method for electricity-heat-hydrogen integrated energy system considering the correlation between variables," *Energy*, vol. vol 263, 2023, doi: https://doi.org/10.1016/j.energy.2022.125678.
[7] S. Xia, J. Cai, Ning Wu, Jing Xiao, Haoyu Hu, Y. Chen, Xu Chen, X. Yang, Haiping Wang, dan H. Chen, "Synthesis and formation mechanism of biomass-based mesoporous graphitic carbon," *Fuel Process. Technol.*, vol. 209, 2020, doi: https://doi.org/10.1016/j.fuproc.2020.10654.
[8] H. Z. Yifei Ma, Pinjing He, "Improving the method for calculating carbon emissions from waste incineration: confirmed with carbon-14 testing of flue gas," *Carbon Res.*, vol. 3, 2024, doi: https://doi.org/10.1007/s44246-024-00162-9.
[9] Prysathryd Sarabhorn et al., "Community-scale co-incineration of pre-sorted MSW with wood pellet using a decoupling gasifier and integrated burner for syngas combustion," *J. Clean. Prod.*, vol. 487, 2025, doi: https://doi.org/10.1016/j.jclepro.2024.144588.
[10] Dongmin Shin et al., "Intelligent Combustion Control in Waste-to-Energy Facilities: Enhancing Efficiency and Reducing Emissions Using AI and IoT," *Energies*, vol. 17, no. Combustion stability and pollutant formation in biomass and waste burning systems, 2024, doi: https://doi.org/10.3390/en17184634.
[11] W. W. Jian Pu, Tiao Zhang, Wen-li Zhou, Jian-hua Wang, "Overall thermal performances of backward film cooling with simulated surface thermal barrier coatings at various walls," *J. Environ. Chem. Eng.*, vol. vol.32, 2022, doi: https://doi.org/10.1016/j.csite.2022.101876.
[12] Qingsong Ji et al., "Design and evaluation of a wind turbine-driven heat pump system for domestic heating in Scotland," *Sustain. Energy Technol. Assessments*, vol. 52, 2022, doi: https://doi.org/10.1016/j.seta.2022.101987.
[13] and rapaisri S.-A. Erawin Thavorn, "The development of supplier comparison using lower process capability index for Weibull distribute on model," *Eng. Appl. Sci. Res.*, vol. 48, hal. 295–306, 2021, doi: https://doi.org/10.14456/easr.2021.32.
[14] and A. J. D. Dileep Kumar, Morshed Alam, "settingsOrder Article Reprints Open AccessEditor's ChoiceArticle Investigating the Influence of Thermal Conductivity and Thermal Storage of Lightweight Concrete Panels on the Energy and Thermal Comfort in Residential Buildings," *Buildings*, vol. 13, 2023, doi: https://doi.org/10.3390/buildings13030720.
[15] Tianhe Long et al., "Numerical simulation of diurnal and annual performance of coupled solar chimney with earth-to-air heat exchanger system," *Appl. Therm. Eng.*, vol. 214, 2022, doi: https://doi.org/10.1016/j.applthermaleng.2022.118851.
[16] Alessandra Martucci et al., "Low-Power Laser Powder Bed Fusion Processing of Scalmalloy," *Materials (Basel).*, vol. 15, 2022, doi: https://doi.org/10.3390/ma15093123.
[17] A. Saleh et al., "Multiple logistic regression based prediction of heat flow direction in an intake incline of shallow depth by integrating thermal flywheel effect: A case study," *Appl. Therm. Eng.*, vol. 213, 2022, doi: https://doi.org/10.1016/j.applthermaleng.2022.118765.
[18] Mengze He et al., "Completion of Waste Heat Recovery and CO2 Conversion Simultaneously Based on the Flue Gas Chemical Recuperative Cycle: A Review," *Energies*, vol. 18, 2025, doi: https://doi.org/10.3390/en18020232.
[19] Furong Cao et al., "Room Temperature Strengthening and High-Temperature Superplasticity of Mg-Li-Al-Sr-Y Alloy Fabricated by Asymmetric Rolling and Friction Stir Processing," *Materials (Basel).*, vol. 16, 2023, doi: https://doi.org/10.3390/ma16062345.
[20] N. S. G. Mugo, "Flue gas emissions and performance evaluation of small-scale solid waste incinerators at Njokerio and Ng'ondu in Njoro, Kenya," Journal of Engineering Research and Reports, vol. 18, pp. 50–66, 2020.
[21] G. O. O. S. G. M. Nyoti, D. M. Nyaanga, and S. F. Owido, "Performance evaluation of flue gas emissions and small-scale solid waste incinerator from Egerton University and its environs, Kenya," Research and Development in Engineering Research, vol. 5, 2023. [Online]. Available: https://stm.bookpi.org/RADER-V5/article/view/11085
[22] J. L. Parracha, "Performance of lightweight thermal insulating mortars applied on brick substrate specimens and prototype wall," Construction and Building Materials, vol. 364, Art. no. 129964, 2023, doi:

10.1016/j.conbuildmat.2022.129964.
[23] M. M. Ahmed et al., "Development of bio-based lightweight and thermally insulated bricks: Efficient energy performance, thermal comfort, and CO_2 emission of residential buildings in hot arid climates," Journal of Building Engineering, vol. 91, 2024.

LOGIC
Journal of Engineering Design and Technology
Vol. 26 No. 1 March 2026 ; p. 71 - 78

p-ISSN : 1412-114X
e-ISSN : 2580-5649
http://ojs2.pnb.ac.id/index.php/LOGIC

A NUMERICAL STUDY OF CORRUGATED SIERPINSKI CARPET ON SOLAR DRYER

Lohdy Diana [1)*], Arrad Ghani Safitra [1)], Eli Novita Sari [2)], Firman Yunan Saputra [1)], Ar Rayyan Ikhsan Syahputra[1)], Muhammad Yusuf Febrian Putra [1)], Mutia Ayu Agustina [1)]

1) Power Plant Engineering, Politeknik Elektronika Negeri Surabaya, Jl. Raya ITS, Surabaya, East Java, Indonesia
2) Manufacturing Engineering Technology, Politeknik Negeri Banyuwangi, Banyuwangi, Indonesia

Correponding email [1)*] :
lohdydiana@pens.ac.id

Abstract. Solar dryers have problems with low heat transfer performance and uneven temperature distribution, resulting in low efficiency. The efficiency of solar dryers depends on the design of the absorber plate, namely how much it can absorb solar heat. This study applies a Siepinski carpet with a complex structure and large dimensions, resulting in iterations called fractals. This study aims to improve the efficiency of solar dryers as an alternative to the negative impact of falling tomato prices, to determine the effect of the Siepinski Carpet Corrugated fractal distance on the performance of solar dryers in terms of heat transfer, to compare corrugated absorber plates with 3 siepinski carpet corrugated based on variations in the fractal ratio (RF), namely the ratio of the fractal center distance to the fractal length RF = 1, RF = 0.75, and RF = 0.6, on the performance of solar dryers, as well as to determine the distribution of temperature, pressure, and air flow velocity in the collector using the Computational Fluid Dynamics (CFD) simulation method. This study used simulation methods that was conducted in a laboratory. In conclusion, the fractal ratio strongly influences airflow behavior and temperature distribution, where overly dense or overly open configurations enhance heat transfer, while intermediate obstruction can reduce thermal performance. Among the cases studied, RF = 1 and RF = 0.6 provide more effective and consistent heat transfer compared to RF = 0.75.

Keywords : Solar Dryers, Sierpinski Carpet, performance

1. INTRODUCTION

Indonesia is known as an agrarian country with a population that depends on the agricultural sector, supported by a tropical climate and mountains that enrich the soil [1]. The agricultural sector contributes around 13% to the national GDP and will absorb 29% of the workforce by 2022, making it the backbone of the rural economy [BPS 2025 data][2], [3], [4], [5]. However, farmers often suffer losses due to drastic price drops during abundant harvests, as in the cases of Lampung and Bandung where production costs are not covered [6], [7]. This is particularly relevant to Indonesian agriculture, where tomatoes are one of the main commodities with an annual production of 1.2 million tons, but 20-30% are lost post-harvest due to decay and price fluctuations [8][9][10]. Dependence on fresh harvests exacerbates the instability of farmers' incomes, so post-harvest processing such as drying can be a solution to extend shelf life, increase selling value, and support national food security [11].

Conventional sun-based drying is still dominant among Indonesian farmers, but this method is dependent on weather, unhygienic, and difficult to control temperature and humidity, resulting in inconsistent dried product quality. Solar dryers were then developed as an efficient and environmentally friendly solution, utilizing Indonesia's solar radiation potential of 4.8 kWh/m² per day [12]. The performance of dryers is greatly influenced by the design of the heat-absorbing plate, where the application of fractal structures such as Sierpinski Carpet Corrugated (SCC) has been proven to increase efficiency by 32-85% through expanded contact area and more even air flow distribution [13][14][15][16][17].

The Sierpinski Carpet fractal structure is a two-dimensional pattern formed through recursive iteration: starting from a whole square, a square hole is then created in the center (1/9 of the area is lost), and the process is repeated on the sub-squares up to a certain fractal level, resulting in a fractal dimension of approximately 1.89

[18]. This pattern creates a corrugated surface that increases the surface area by 2-3 times compared to a flat plate, facilitating even heat distribution and an optimal laminar-turbulent airflow pattern. Relevant research such as the study by Koch and Löhndorf (2020) on fractal heat exchangers shows a 40% increase in heat transfer thanks to self-similar geometry, while CFD simulations by Wang et al. (2022) on SCC solar air heaters prove 75% thermal efficiency at a fractal ratio of 0.6. The advantages of the Sierpinski Carpet structure include: large surface area for optimal convection, uniform airflow distribution that reduces hotspots, lightweight and inexpensive production using corrugated metal sheets, and scalability for small-scale applications. Its disadvantages include: fabrication complexity at high iterations that increases costs (up to 20% more expensive), potential dust accumulation in fractal gaps that clogs the flow, and sensitivity to variations in the fractal ratio (FR) where an FR that is too small (<0.5) actually reduces air velocity by up to 15%.

This study developed the Sierpinski Carpet Corrugated Solar Air Heater (SCCA-SAH) to improve tomato drying efficiency, supporting the production of high-value products such as Torakur—date-flavored tomatoes sold for up to Rp60,000/kg [19][20][21]. Experimental methods and CFD simulations were used to analyze the effect of varying fractal ratios (RF = 1, 0.75, 0.6) on heat distribution, efficiency, air velocity, and drying rate [22][23]. This development is expected to reduce losses for Indonesian farmers and encourage agricultural product diversification.

2. SIMULATION METHODS

This chapter provides a comprehensive explanation of the design, including the data collection techniques, location, and timeframe. It also explains the procedures for impartial data processing and assessment to achieve the stated objectives: to determine the distribution of air temperature, air pressure, and air flow velocity within the collector using Computational Fluid Dynamics simulation. This research employed a mixed method, consisting of qualitative and quantitative methods. The quantitative method involved data collection based on research into the decline in tomato selling prices in Indonesia after harvest. The qualitative method utilized ANSYS Fluent software simulations is a Computational Fluid Dynamics (CFD)-based simulations software widely used to analyze fluid flow and heat transfer through three main stages: pre-processing, processing, and post-processing. In the pre-processing stage, the geometry is created in Space Claim with specific dimensions shown in Figure 1(a) and RF variations, then important parts are named and an enclosure is formed to define the flow domain before the simulation proceeds shown in Figure 1(b).

The next step is meshing, which divides the geometric domain into small elements for numerical discretization. Mesh quality greatly affects simulation accuracy, so the size and type of mesh must be adjusted to the complexity of the geometry, where the configuration for each RF variation is shown in Figure 1(c). Numerical calculations were performed using CFD with a k-ε turbulence model and SIMPLE algorithm for pressure-velocity coupling. A three-dimensional steady-state model was used to analyze the effect of RF on heat transfer and flow. The flow regime is assumed to be laminar is selected due to its suitability for internal flow and heat transfer analysis. The light intensity on the upper wall is assumed to be 585 W/m^2. A second-order discretization scheme is applied to the momentum and energy equations to improve numerical accuracy. Convergence criteria are defined based on residual values, with continuity and momentum residuals set to 10^{-4} to ensure physically stable and meaningful solutions in all RF configurations.

The next step is to determine the boundary conditions, including inlet velocity, outlet pressure, temperature, and wall conditions to match the actual conditions. Once all parameters have been determined, the solution process is carried out iteratively until a convergent solution is obtained. Once convergence is achieved, the simulation results are saved and analyzed using the post-processing feature. Post-processing involves analyzing and visualizing the simulation results. This stage is used to obtain an overview of fluid flow, air pressure distribution, air temperature distribution, and air flow velocity, in accordance with the research objectives using the Computational Fluid Dynamics (CFD) method. The dimension, material, and simulation parameter setting can be seen in Tables 1.

3. RESULT AND DISCUSSION

The temperature contour distribution of the three fractal ratio variations shows quite clear differences in heat transfer characteristics. At RF=0.6, it shows that a denser fractal structure increases air mixing, thereby reducing hot spots, but also lowering the maximum temperature increase. This results in a highest temperature peak of 389.7 K with a temperature deviation of 56 K, indicating a higher heating zone and sharper temperature contrast as well as increased local heat transfer but with a less uniform distribution. The differences between these three variations indicate a trade-off between increased heating efficiency and uniformity of heat distribution, so the choice of fractal ratio must be tailored to the system design requirements. Based on the reinterpretation that RF=1 represents the densest fractal distance, the experimental results show a pattern consistent with leading literature studies. An overly dense fractal configuration causes a significant increase in pressure drop and flow resistance, thereby reducing the air mass flow rate and ultimately decreasing heat transfer performance, as reflected in the lowest outlet temperature showing a lower temperature deviation of 54.9 K, indicating a more uniform thermal distribution, but very little heat transferred. These findings are consistent with the principle in thermal engineering that states that optimization of heat sink geometry must balance between increasing surface area and pressure loss [13].

Figure 2 shows the grid indenpendency for simulation to ensure stability. The results indicate that the air outlet temperature generally increases as the number of cells rises, showing improved resolution of heat transfer with finer discretization. A significant increase is observed when the cell number is raised from 5,000 to 18,000, suggesting that coarse meshes tend to underpredict the outlet temperature. Beyond this range, the temperature variation becomes smaller, indicating that the solution starts to converge. The case with 7,000 cells shows a temperature comparable to higher cell counts, implying that this mesh density already provides a reasonable balance between accuracy and computational cost.

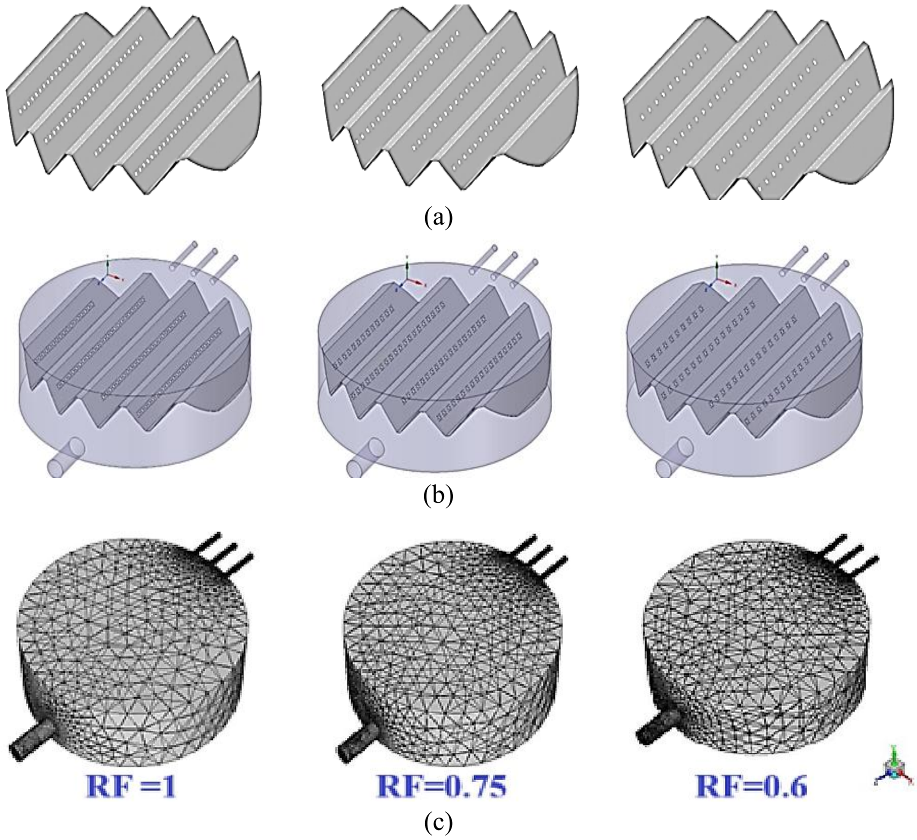

Figure 1. (a) Corrugated Sierpinski Carpet Model, (b) Solar Collector Model, (c) Meshing

Table 1. Dimension, Material, and Simulation Parameter Setting.

Parameter	Settings
Dimension	0,975 mm
Modelling	3D
Material	Aluminum
Boundary Condition	
Inet:	Velocity inlet: 0,5 m/s
Outlet:	Pressure outlet
Top Wall	Heat Flux 585 w/m^2
Bottom and Cover Wall	Adiabatic
Algorithm	SIMPLE
Residual	10-e4
Energy	ON
Temperature inlet	300K
Discretization	First Order

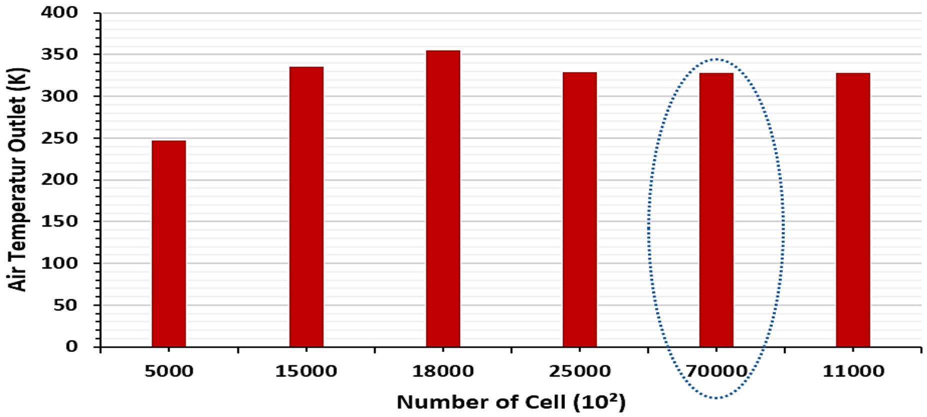

Figure 2. Grid Independency

3.1 Temperatur Distribution

Figure 3 shows the temperature distribution, it shows three distinct behaviors that reflect how the fractal absorber geometry reshapes the heat pickup along the dryer. The RF = 1 curve (blue, triangles) showing a sharp temperature increase of about 34 K in the first third of the channel length, starts cooler near the inlet 300 K, then exhibits a sudden jump around the first third of the channel and remains at a higher plate 334K until 336 K downstream a signature of strong local heat accumulation caused by dense obstacles that trap air and create recirculation zones with long residence times. The RF = 0.75 trace shows in red color, results in an output temperature that is 10-15% lower in the range of 320-330 K and a decrease in efficiency of around 15-15.5%, which indicates less than optimal thermal interaction due to excessively smooth flow. The RF = 0.6 series. It shows the most even, steadily increasing temperature toward the outlet and reaches comparable or slightly higher outlet temperatures, which suggests that the more open fractal spacing promotes beneficial mixing: enough turbulence to enhance surface-to-air heat exchange without producing severe local hot spots or excessive flow resistance. These trends match the simulation observations that fractal spacing controls the trade-off between maximum heating and uniformity as shown in Figure 4. That the fractal ratio (RF) significantly affects thermal behavior within the channel. The RF = 1 configuration produces higher but locally accumulated temperatures due to increased flow obstruction. RF = 0.75 exhibits strong thermal gradients and non-uniform heating. In contrast, RF = 0.6 provides the most uniform temperature distribution, indicating balanced convection–conduction heat transfer and improved thermal stability.

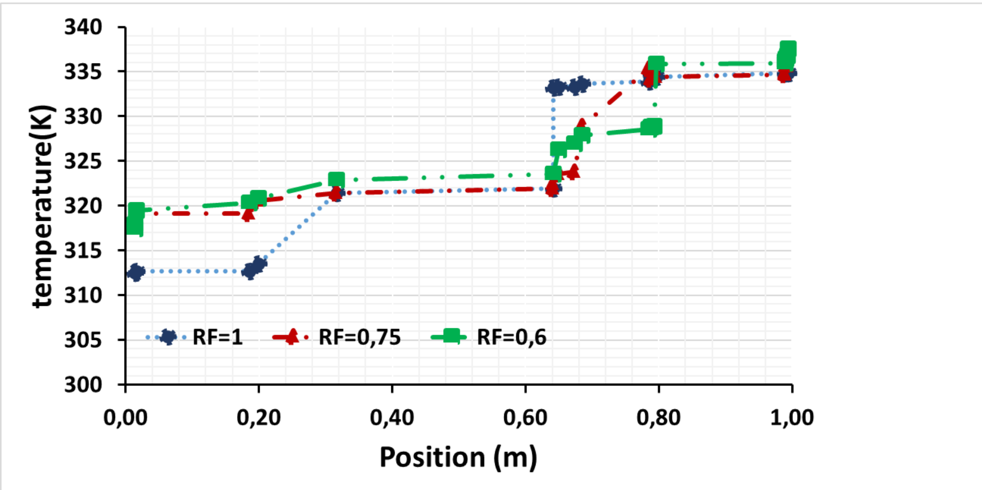

Figure 3. Air Temperature Distribution in Middle Line.

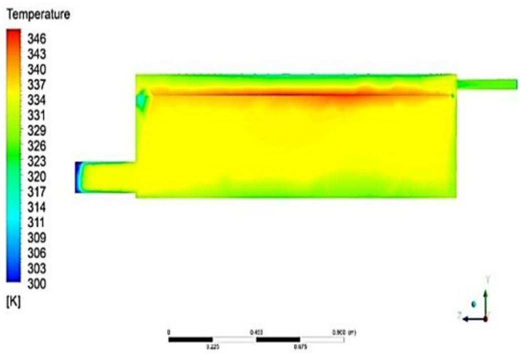

(a)

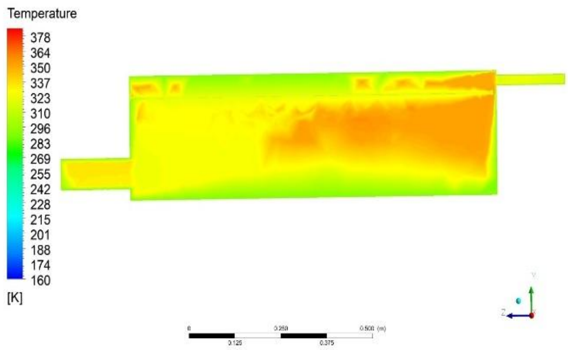

(b)

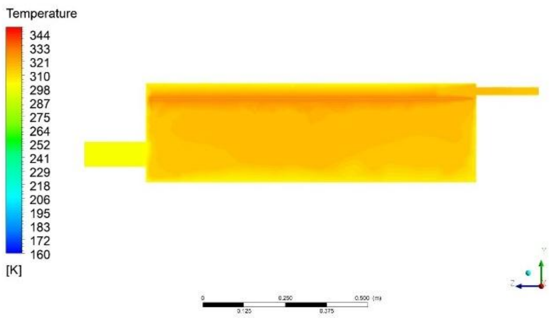

(c)

Figure 4. Contour (a) RF=1, (b) RF=0,75, (c) RF=0,6

3.2 Velocity Distribution

The velocity is shown in Figure 5, the chart explains the temperature patterns by revealing how the fractal layout reorganizes the airflow. For RF = 1 the velocity stays modest through the inlet region then accelerates sharply near the downstream constrictions, producing the large peaks seen at the far right; this acceleration follows flow through narrow passages created by dense fractal elements and explains why temperature jumps occur where the air is rapidly compressed and heated locally. RF = 0.75 shows a mid-channel velocity rise (around 0.3–0.5 m) and then a decline toward the outlet — a behavior consistent with moderate obstruction that momentarily boosts convective transport but then allows the flow to slow and re-mix, producing steadier, lower peak temperatures. RF = 0.6 begins with a relatively high inlet velocity that drops and smooths out downstream, indicating an initially open inlet that quickly converts momentum into distributed mixing; this pattern sustains continuous convective transfer and yields a gradual, uniform temperature increase. In short, the velocity plots reveal the hydrodynamic mechanisms acceleration, recirculation, residence time by which fractal spacing controls both local heating and overall thermal performance.

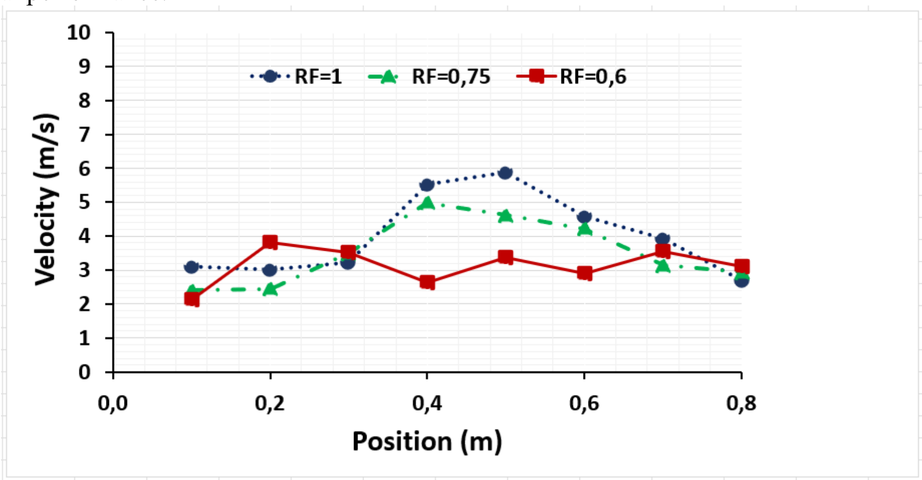

(b)

Figure 5. Air Velocity Distribution in Middle Line.

3.3 Average Temperature and Heat Transfer Efficiency

Table 2. Average Temperature and Heat Transfer Efficiency

Variation	Average Temperature Outlet (K)	Heat Transfer Efficiency (%)
RF=1	328,43	17,14
RF=0,75	326,66	5,46
RF=0,6	328,00	16,72

Based on Table 2, variations in the RF parameter have a noticeable influence on both the average outlet temperature and the heat transfer efficiency as shown below :

$$\Delta T = \frac{Number\ of\ Temperature\ Data}{Total\ Temperature\ Data} \tag{1}$$

$$\eta = \frac{Qactual}{Qmax} \tag{2}$$

At RF = 1, the average outlet temperature reaches 328.43 K, accompanied by the highest heat transfer efficiency of 17.14%. This condition indicates that the system operates near its optimal thermal performance, where the heat exchange process is relatively effective. When the RF value is reduced to 0.75, the average outlet temperature decreases to 326.66 K. More significantly, the heat transfer efficiency drops sharply to 5.46%. This substantial reduction suggests that, under this condition, the heat transfer mechanism becomes less effective, possibly due to unfavorable flow characteristics or reduced turbulence intensity that limits thermal energy exchange. Further reduction of RF to 0.6 results in an increase in the average outlet temperature to 328.00 K, which is comparable to the value observed at RF = 1. The heat transfer efficiency also recovers to 16.72%, approaching the maximum efficiency recorded in this study. This trend indicates that lower RF does not necessarily lead to poorer thermal performance, and that certain RF conditions can enhance heat transfer by improving flow behavior and thermal interaction within the system. Overall, the results demonstrate that the relationship between RF, outlet temperature, and heat transfer efficiency is non-linear. While RF = 1 and RF = 0.6 provide relatively high efficiencies, RF = 0.75 represents a less favorable operating condition. These findings highlight the importance of selecting an appropriate RF value to achieve optimal heat transfer performance.

4. CONCLUSION

1. The variation in fractal ratio (RF) directly shapes how heat is distributed along the channel. A denser configuration (RF = 1) showed a sharp temperature increase of about 30–35 K in the first third of the channel, accompanied by a higher axial temperature gradient compared to other configurations., while more open arrangements (RF = 0.75 and RF = 0.6) allow the air to move more smoothly, resulting in a gentler and more uniform rise in temperature.
2. These heating differences are largely driven by how each fractal layout alters the airflow pattern. When the geometry creates too much resistance, the flow becomes unstable, accelerating and decelerating abruptly, which leads to uneven heating. But when the obstruction is balanced, the airflow stays steady and well-mixed, enabling the thermal energy to be carried more consistently throughout the channel.
3. The heat transfer efficiencies were obtained at RF = 1 and RF = 0.6, with values of 17.14% and 16.72%, respectively, accompanied by relatively high outlet temperatures. In contrast, the RF = 0.75 condition produced a noticeably lower outlet temperature and a substantial decrease in heat transfer efficiency, indicating less effective thermal interaction.
4. The limitation of this simulation lies in the reliance on a first-order approach and intricate parameter settings, which may not completely represent actual operating conditions. Further studies should explore more advanced modeling techniques.

5. ACKNOWLEDGEMENT

This research was funded by the Directorate of Research and Community Service, Direktorat Penelitian dan Pengabdian Masyarakat (DPPM) and supported by the Electronics Engineering Polytechnic Institute of Surabaya, Politeknik Elektronika Negeri Surabaya (PENS).

REFERENCES

[1] Q. Ayun, S. Kurniawan, and W. A. Saputro, "Perkembangan Konversi Lahan Pertanian Di Bagian Negara Agraris," *Vigor J. Ilmu Pertan. Trop. Dan Subtrop.*, vol. 5, no. 2, pp. 38–44, 2020, doi: 10.31002/vigor.v5i2.3040.

[2] T. Pertumbuhan and E. Dalam, "PRESPEKTIF ISLAM (STUDI PADA KABUPATEN TULANG," pp. 205–212, 2024.

[3] S. Sulawesi, "Jurnal Polimesin," vol. 23, no. 3, 2025.

[4] S. F. Purba, A. Yulianti, S. Astana, and R. D. Djaenudin, "The contribution of agricultural crop production towards the economic growth of Indonesia ' s agricultural sector," vol. 34, 2023.

[5] J. Publikasi *et al.*, "Evaluasi Kinerja Sektor Pertanian dalam Kontribusinya terhadap Pendapatan Nasional dengan Pendekatan Metode Produksi," 2025.

[6] R. Sanusi Putri, "Petani Tomat Buang Hasil Panen karena Harga Jeblok dari Rp 4.000 jadi Rp 600 per Kg, Respons Kementan?," Tempo. Accessed: Jul. 02, 2025. [Online]. Available: https://www.tempo.co/ekonomi/petani-tomat-buang-hasil-panen-karena-harga-jeblok-dari-rp-4-000-jadi-rp-600-per-kg-respons-kementan--225861

[7] R. Harmoni, "Harga Anjlok, Petani Di Lembang Biarkan Tomat Membusuk," TV Harmoni. Accessed: Jul. 02, 2025. [Online]. Available: https://tvharmoni.com/2024/08/01/harga-anjlok-petani-di-lembang-biarkan-tomat-membusuk/

[8] Saptana *et al.*, "Competitiveness analysis of fresh tomatoes in Indonesia: Turning comparative advantage into competitive advantage," *PLoS One*, vol. 18, no. 11 November, pp. 1–29, 2023, doi: 10.1371/journal.pone.0294980.

[9] A. Jarman *et al.*, "Postharvest Biology and Technology Postharvest technologies for small-scale farmers in low- and middle-income countries : A call to action," *Postharvest Biol. Technol.*, vol. 206, no. September, p. 112491, 2023, doi: 10.1016/j.postharvbio.2023.112491.

[10] T. Molelekoa, E. M. Karoney, N. Siyoum, and J. K. Gokul, "Quality and Quantity Losses of Tomatoes Grown by Small-Scale Farmers Under Different Production Systems," pp. 1–21, 2025.

[11] S. Soekarno, T. D. Septian, I. Indarto, N. P. Lestari, and R. Nadzirah, "Uji Kinerja Multi Seeds Smart Dryer (MSSD) Pada Kacang Hijau (Vigna Radiata)," *Rona Tek. Pertan.*, vol. 17, no. 2, pp. 94–106, 2024, doi: 10.17969/rtp.v17i2.34808.

[12] et al Barata, L. O. A., "Performance evaluation of a standalone solar PV system: a case study in Kendari, Southeast Sulawesi, Indonesia," *Jural Polimesin*, vol. 23, 2025, doi: http://dx.doi.org/10.30811/jpl.

[13] C. Prasopsuk, K. Sutthivirode, and T. Thongtip, "Performance Enhancement of a Solar Air Heater Equipped with a Tree-like Fractal Cylindrical Pin for Drying Applications: Tests Under Real Climatic Conditions," *Energies*, vol. 18, no. 9, 2025, doi: 10.3390/en18092230.

[14] S. Dryer, U. Flat, and P. A. Plates, "Journal of Engineering," vol. 31, no. 8, pp. 200–226, 2025.

[15] Y. Gao *et al.*, "The Effect of Geometric Parameters on Flow and Heat Transfer Characteristics of a Double-Layer Microchannel Heat Sink for High-Power Diode Laser," 2022.

[16] L. Nguyen and M. Ha, "Heat transfer and flow characteristics in horizontal spiral coils with flat tubes and rectangular ribs : CFD and optimization," *Int. J. Thermofluids*, vol. 26, no. January 2025, p. 101072, 2027, doi: 10.1016/j.ijft.2025.101072.

[17] C. C. By, "Fractal Geometry as an Effective Heat Sink," 2022, doi: 10.5545/sv-jme.2022.28.

[18] J. B. Pascual-Francisco, O. Susarrey-Huerta, L. I. Farfan-Cabrera, and R. Flores-Hernández, "Creep Properties of a Viscoelastic 3D Printed Sierpinski Carpet-Based Fractal," *Fractal Fract.*, vol. 7, no. 8, 2023, doi: 10.3390/fractalfract7080568.

[19] A. D. K. Eko Suharyono, dan Wiharso, "Analisis pendapatan bersih dan kelayakan pengolahan tomat (Solanum lycopersicum) menjadi torakur (tomat rasa kurma) di Kecamatan Bumijawa Kabupaten Tegal," *AGROMEDIA Berk. Ilm. Ilmu-ilmu Pertan.*, vol. 40, no. 2, pp. 68–75, 2022, doi: 10.47728/ag.v40i2.381.

[20] kumparanFOOD, “Foto: Produksi Tomat Rasa Kurma di Kabupten Semarang Saat Bulan Ramadhan,” Kumparan Food. Accessed: Jul. 04, 2025. [Online]. Available: https://kumparan.com/kumparanfood/foto-produksi-tomat-rasa-kurma-di-kabupaten-semarang-saat-bulan-ramadan-24ctmUkgFST

[21] N. S. G. Destyana, M. Ferichani, and E. W. Riptanti, “Strategi Pengembangan UKM TORAKUR (Tomat Rasa Kurma) di Kecamatan Bandungan Kabupaten Semarang,” *Agrista*, vol. 5, no. 1, pp. 214–224, 2017.

[22] A. Kibishov, G. A. Kilic, N. Rustamov, and N. Genc, “Thermal Analysis of Radiation Heat Transfer of Improved Fractal Solar Collectors,” *Appl. Sci.*, vol. 14, no. 23, 2024, doi: 10.3390/app142311155.

[23] M. A. Amraoui and K. Aliane, “Three-dimensional analysis of air flow in a flat plate solar collector,” *Period. Polytech. Mech. Eng.*, vol. 62, no. 2, pp. 126–135, 2018, doi: 10.3311/Ppme.11255.

[24] Z. Men and W. Chen, “Heat Transfer Enhancement of Controllable Aspect Ratio Fractal Channel,” 2023.

LOGIC
Journal of Engineering Design and Technology
Vol. 26 No. 1 March 2026 ; p. 79 - 85

p-ISSN : 1412-114X
e-ISSN : 2580-5649
http://ojs2.pnb.ac.id/index.php/LOGIC

KINETICS OF BIODEGRADATION OF CASSAVA STARCH - COFFEE GROUNDS BIOPLASTICS IN SOIL AND AQUEOUS MEDIA

1) Mechanical Engineering Department, Politeknik Negeri Bali, Bali, Indonesia
2) Pharmacy Study Program, Faculty of Mathematics and Natural Sciences, Universitas Udayana, Bali, Indonesia
3) Department of Materials Engineering, Faculty of Industrial Technology, Institut Teknologi Sumatera

Corresponding email [1)*] :
komangwidhi@pnb.ac.id

Komang Widhi Widantha[1*], Risa Nurin Baiti [1], I Wayan Padma Yogi Asana [1], Ni Luh Wisma Eka Yanti [2], Anisa Fitri [3]

Abstract. Starch-based bioplastics have emerged as sustainable substitutes as a result of the buildup of plastic waste. However, high costs and technical flaws frequently restrict their industrial application. While previous studies have explored agricultural fillers, there is a scarcity of kinetic modeling that evaluates biocomposite degradation across diverse disposal scenarios. The purpose of this work is to examine the biodegradation kinetics of bioplastics made from cassava starch and reinforced with spent coffee grounds (SCG) at different concentrations (0%, 10%, 20%, and 30%). Over the course of 28 days, biodegradation tests were carried out in three different settings: acidic solution, tap water, and soil burial. The findings demonstrated that adding SCG greatly sped up the degradation process, with weight loss peaking at 55.3% in soil burial for the 30% SCG formulation. The degradation rate constant (*k*) gradually rose with increasing SCG content in all media, according to kinetic analysis based on a first-order model. Microbial enzymatic activity in soil produced the highest (*k*) value, which was 0.0283 days^{-1}. Acidic solution also promoted faster degradation (0.0253 days^{-1}) through acid-catalyzed hydrolysis than tap water (0.0189 days^{-1}). These findings provide a clear practical guide for the packaging industry to control how fast a product breaks down by simply adjusting the coffee waste content. This research offers a realistic way for businesses to recycle coffee waste into functional packaging that disappears safely after use, supporting a cleaner environment.

Keywords : Biodegradation, Bioplastics, Coffee, Green Materials, Kinetics

1. INTRODUCTION

Indonesia's plastic waste crisis has reached a critical stage, with estimates indicating a 30% increase in the flow of plastic debris between 2017 and 2025 [1]. The development of biodegradable polymers has become a crucial strategy in the fight against this environmental danger, offering a sustainable substitute for traditional plastics derived from petroleum. Despite being essential for packaging, adoption is frequently impeded by high material costs that outweigh the advantages for the environment. In order to balance sustainability with the "waste-to-wealth" concept, using cassava by-products like peels shows great promise as an inexpensive source that can address technical limitations like sensitivity to moisture and retrogradation processes [2]. According to Darni and Utami [3], these starch-based materials are made to decompose organically without encountering the usual problems with structural integrity. Furthermore, these bioplastics exhibit high ecological safety; research indicates they are non-toxic to the soil upon degradation and can even actively promote the growth of tested plant species [4].

Because it can be recycled and processed in a variety of ways, starch is a great option for the production of bioplastics, which can help cut pollution by providing a sustainable substitute for plastics made from fossil fuels. Its film characteristics are determined by the amylose-to-amylopectin ratio, with higher amylose levels providing greater stiffness and strength [5]. Cassava starch is very popular in Indonesia because it is inexpensive and has good film-forming properties. Research shows that tapioca-based biopolymers frequently produce the best, smoothest, and most flexible results when compared to other starch types [6]. However, its natural brittleness and propensity to absorb moisture frequently restrict its industrial use in architectural and food packaging applications [7, 8]

Beyond technical performance, economic considerations usually take precedence over environmental concerns among consumers. Thus, employing cassava by-products in a "waste-to-wealth" strategy offers a methodical way to produce materials at a reasonable price while tackling issues like retrogradation. It has been shown that incorporating natural fibers and nanoparticles enhances mechanical stiffness and water barrier properties while also accelerating the soil's biodegradation process in order to get around these limitations. [9]. The goal of this engineering and design collaboration is to identify the best material components for a more environmentally friendly future so that these sustainable substitutes can rival traditional synthesized polymers. [6, 7].

Organic fillers have drawn a lot of interest as a cutting-edge waste management technique to enhance the quality of bioplastics. The growing popularity of coffee culture in Indonesia, particularly in places like Bali, has resulted in a significant waste product known as spent coffee grounds (SCG) [10]. Apart from SCG, other waste materials such as coffee flour, mucilage, husk, and silverskin possess tremendous potential for the production of environmentally friendly containers through various methods such as laboratory-scale solvent casting and large-scale extrusion [11]. The use of these agricultural waste materials for the production of additives is extremely beneficial for the creation of a circular economy and industrial symbiosis, which is environmentally friendly and results in a lower carbon footprint compared to other fillers such as commercial metal oxide fillers [12, 13]. While further increasing the filler concentration tends to diminish mechanical properties, it also speeds up the rate of degradation [14].

SCG offers polyphenols and lignocellulosic components that can strengthen the starch matrix chemically [15]. Prior research has shown that adding fillers made from coffee waste can significantly increase flexibility, with increases in elongation at break of up to 106% at low loading levels (1–5% weight percentage); however, this is frequently accompanied by a decrease in Young's modulus and maximum tensile stress [16]. Despite these advantages, the mechanical and barrier properties of bioplastics remain major hurdles to their commercial realization in food packaging [17]. The material's stiffness may be negatively impacted by excessive loading, even though these fillers significantly change the active and physical characteristics needed for protective purposes. In order to improve composite performance and guarantee scalable, affordable, and sustainable industrial applications, waste fillers must be modified or pre-treated to maximize interfacial adhesion [11, 12, 18]

The effects of these composites on the environment during disposal are still a major worry, even with advancements in mechanical reinforcement. The composition of the polymer, environmental factors like temperature, pH, and ultraviolet (UV) radiation, as well as the presence of chemical additives, all interact intricately to drive biodegradation rates [19]. Understanding these factors is paramount because when a polymeric product is released into the environment, it undergoes degradation that may lead to the formation of microplastics if the process is not fully completed [20]. Starch-based bioplastics have shown notable degradation, achieving up to 74% weight loss within 120 days, while also changing soil bacterial dynamics, in contrast to traditional plastics like oxo-LDPE, which may exhibit only a slight weight reduction [21]. Changes in the soil microbial community are brought about by this degradation process, particularly an increase in the number of bacteria that can use plastic materials and those that participate in nitrogen cycling, which appear at particular points during the burial period [21]. It is essential to investigate biodegradation kinetics in order to predict the duration of full assimilation and ensure that no toxic residues remain. Thus far, there has been limited focus on kinetic modeling of SCG-reinforced bioplastics under various real-world environmental conditions.

This study aims to investigate the biodegradation kinetics of bioplastics derived from coffee grounds and cassava starch over a 28-day observation period. The study specifically examines degradation rate constants in three distinct environments in order to model different disposal scenarios. By monitoring weight loss intervals, this study aims to clarify how SCG concentrations affect the environmental lifespan and decomposition efficiency of these sustainable packaging materials.

2. METHODS

The traditional markets in Bali, Indonesia, provided the cassava starch used in this study, ensuring the use of a readily available, renewable raw material representative of local resources. To increase the sustainability of the bioplastic production process and utilize post-consumer organic waste, SCG, a natural filler, was collected from local coffee shops. Upon collection, the SCG were first washed thoroughly with distilled water to remove residual sugars, oils, and soluble impurities that could interfere with film formation or biodegradation behavior. The cleaned SCG were then oven-dried at a controlled temperature of 60 °C for 24 hours to eliminate moisture content while preventing thermal degradation of the lignocellulosic components. After drying, the SCG were mechanically sieved to obtain a uniform particle size of 250 µm, which was selected to promote homogeneous dispersion within the starch matrix and improve interfacial interaction.

Solution casting was used to create bioplastic films. After being dissolved in distilled water for about fifteen minutes to reach the proper consistency, 30% glycerol was used to plasticize the cassava starch. The mixture was heated (70–80°C) under stirring until gelatinization occurred. Subsequently, SCG was added at various concentrations (0%, 10%, 20%, and 30% wt%). The homogeneous solution was cast into molds and dried at room temperature for 48 hours. The resulting films were cut into 4 x 4 cm specimens. Degradation behavior was evaluated in three media: soil, water, and acidic solution. For soil burial, samples were buried at a depth of 5 cm in garden soil with a pH of 6.7 and a moisture content of 32%. For tap water and acidic tests, films were fully immersed, with media replaced weekly to ensure consistency. To create the acidic solution, concentrated acetic acid was diluted with distilled water until a pH of 4.0 was reached, simulating an acidic environment. Every experiment was carried out at room temperature.

The samples from every environment were meticulously extracted at pre-established intervals of 3, 7, 14, and 28 days. Before being analyzed, the recovered samples were allowed to air-dry at room temperature for a full day after being gently rinsed with distilled water to get rid of any surface residues or adhered soil particles. The dried samples were then weighed using an analytical balance to determine weight loss as an indicator of biodegradation progress. The weight loss percentage was calculated using the equation:

$$WL = \frac{W0 - Wt}{W0} x\ 100\%$$

where W0 is the initial weight and Wt is the weight after the specified degradation period.

3. RESULTS AND DISCUSSION

3.1 Results

The visual appearance of the bioplastic films is significantly impacted by the concentration of SCG, as shown in Figure 1. The film's ability to retain high transparency and a smooth, homogeneous surface at 10% loading indicates excellent compatibility and uniform filler dispersion within the starch matrix. Higher opacity and a darker hue are the results of increasing the SCG content to 20%. At this stage, localized agglomeration and minor surface irregularities start to show, indicating that the matrix is starting to reach its limit for consistent filler integration. The film becomes primarily opaque and visually heterogeneous at the maximum loading of 30%. There is noticeable particle clustering, which results in structural discontinuities and a rougher texture.

Figure 1. Visual appearance of cassava starch-based bioplastic films reinforced with varying concentrations of spent coffee grounds (SCG): (left) B1 with 10% wt, (center) B2 with 20% wt, and (right) B3 with 30% wt.

Over the course of 28 days, the biodegradation of bioplastics made from cassava starch and coffee grounds was assessed in three different media: soil, acidic solution, and water. The percentage of weight loss for each formulation (0%, 10%, 20%, and 30%) was monitored at intervals of 3, 7, 14, and 28 days to determine the degradation profile. The comprehensive results of the weight loss measurements are summarized in Table 1, while the visual progression of the degradation is illustrated in Figure 2.

Table 1. Percentage of weight loss of bioplastic samples in various degradation media over 28 days.

Degradation Medium	Sample Code	SCG Content (%)	3 Days (%)	7 Days (%)	14 Days (%)	28 Days (%)
Tap Water	B0	0	4.2	9.3	13.1	21.3
	B1	10	7.4	14.2	19.2	33.2
	B2	20	7.7	16.1	22.4	38.8
	B3	30	7.2	15.4	23.4	36.5
Acidic solution	B0	0	8.4	17.2	24.1	40.1
	B1	10	8.8	18.3	25.5	42.3
	B2	20	8.9	18.5	25.8	42.4
	B3	30	9.2	20.1	27.7	49.5
Soil Burial	B0	0	10.2	21.8	29.2	50.4
	B1	10	9.3	21.7	28.4	44.9
	B2	20	10.5	22.6	32.4	51.9
	B3	30	10.9	22.9	36.8	55.3

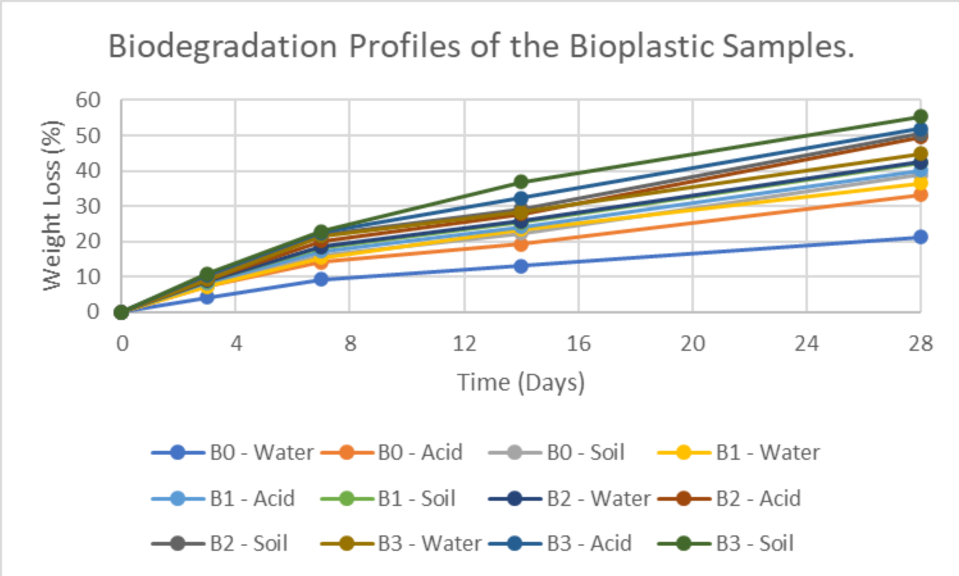

Figure 2. Biodegradation profiles of bioplastic samples in various environmental media over 28 days.

Over the course of the 28-day observation period, all bioplastic formulations showed a progressive increase in weight loss, as shown in Figure 2. With a maximum weight loss of 50.4% in soil, the control samples continuously displayed the lowest degradation rates across all media, as shown by the lower trajectories on the graph. On the other hand, the degradation process was considerably accelerated by the addition of SCG. This pattern is evident in Figure 2, where samples with 30% SCG had the greatest weight loss across all environments, peaking at 55.3% in soil at the conclusion of the investigation.

The degradation environment, specifically microbial activity, moisture, and pH, had a major impact on the rate of decomposition. Regardless of SCG concentration, soil burial consistently displayed the highest weight loss values, followed by acidic solution, while tap water displayed the lowest rates. Figure 2 illustrates this hierarchy by demonstrating that, in contrast to the aqueous media, the soil burial curves maintain a steeper incline. For instance, at 20% SCG loading, the weight loss after 28 days was 51.9% in soil, 42.4% in acidic solution, and 38.8% in water. These results, supported by both the tabular and graphical data, indicate that both filler concentration and the nature of the medium are primary determinants of the biodegradation behavior of these biocomposites.

3.2 Discussion

Effect of Spent Coffee Grounds (SCG) on Biodegradation

The findings unequivocally show that adding SCG speeds up the weight loss of bioplastics made from cassava starch. The disruption of the starch matrix's continuity by the SCG particles is the primary cause of this phenomenon. Higher SCG loadings cause more filler agglomeration, which results in micro-voids and interfacial gaps between the filler and the polymer matrix, as the morphological analysis shows. The surface area available for enzymatic and hydrolytic attack is increased by these structural discontinuities, which make it easier for moisture and microbes to enter the inner layers of the film. However, an unexpected trend occurred in tap water, as the 30% SCG sample (B3) degraded slower than the 20% sample (B2). This most likely occurred as a result of the coffee's natural oils repelling water and its denser particles filling the pores more firmly, offering momentary protection in neutral environments. Unlike inorganic reinforcements like bentonite, which tend to stabilize the bioplastic and slow down the degradation rate by increasing material integrity, organic fillers like SCG and coffee skin fibers actively promote decomposition. Previous studies on cassava-based bioplastics reinforced with coffee skin fibers reported significant biodegradation values ranging from 32.9% to 68.9%, underscoring the effectiveness of coffee-derived waste as a natural degradant [22].

Additionally, coffee grounds' hydrophilic lignocellulosic components improve water absorption and serve as a catalyst in the early phases of degradation. Recent research indicates that 10% filler content (B1) provides the best balance by slightly improving mechanical properties while enhancing degradation, whereas higher filler levels (B2 and B3) further increase biodegradability at the expense of tensile strength and flexibility. [14]. This rapid weight loss in soil within 28 days is consistent with observations of starch-based films lacking high-integrity stabilizers, which typically undergo rapid fragmentation after the initial stages of burial [23].

Comparative Analysis of Degradation Media

The study's degradation rates were consistently grouped in a hierarchy, with the soil environment having the largest impact, followed by acidic solutions and tap water. In the soil environment, the formulation containing 30% SCG experienced the greatest weight loss, peaking at 55.3%. This rapid decomposition is attributed to the synergistic effect of biotic and abiotic factors; specifically, the diverse community of soil-dwelling bacteria and fungi secretes amylase and other extracellular enzymes that hydrolyze starch polysaccharides into simpler sugars for microbial metabolism. This pattern is consistent with earlier studies on bioplastics based on starch, which reported higher weight loss in soil (up to 63%) compared to aquatic environments such as river water (54%), with significantly higher degradation rate constants observed in soil media [25].

A low pH environment actively promotes the hydrolysis of glycosidic bonds within the starch chain by acid, as evidenced by the higher rate of degradation seen in acidic solution compared to tap water in aqueous environments. This chemical cleavage increases the matrix's solubility and fragmentation susceptibility by reducing the polymer's molecular weight. On the other hand, tap water loses weight the slowest of all the environments tested because it lacks the concentrated microbial activity present in soil as well as the accelerated chemical reactivity of an acidic medium. The kinetic calculations of Syuhada [25] corroborate these findings, confirming that the superior availability of biological degradants in soil usually results in a higher rate of biodegradation than in water-based media.

Biodegradation Kinetics

A first-order kinetic model was used to assess the quantitative analysis of the degradation process. Deep insight into how the material composition and the external environment affect the bioplastic's lifespan can be gained from the rate constant (k), which shows the rate of weight reduction over time.

Table 2. Calculated first-order degradation rate constants (k) for SCG-reinforced bioplastics in different media.

Degradation Medium	Sample Code	SCG Content (%)	Rate Constant (k) (days^{-1})
Tap Water	B0	0	0.0082
	B1	10	0.0157
	B2	20	0.0177
	B3	30	0.0189
Acidic solution	B0	0	0.0136
	B1	10	0.0175
	B2	20	0.0236
	B3	30	0.0253
Soil Burial	B0	0	0.0168
	B1	10	0.0188
	B2	20	0.0240
	B3	30	0.0283

The data in Table 2 reveals a significant correlation between the filler concentration and the degradation velocity. In all tested media, the rate constant (k) increases progressively as the SCG content rises from 0% to 30%. In tap water, for instance, the k value nearly doubles from the control (0.0082 days^{-1}) to the 10% SCG variation (0.0157 days^{-1}). This suggests that adding even a small amount of coffee grounds significantly changes the starch matrix, making it more porous and more likely to absorb moisture. This pattern is in line with research by Amer [24], who found that while pure synthetic polymers stay the same, weight loss and water absorption rise with increasing starch or organic content.The kinetic behavior is also significantly influenced by the surrounding circumstances. The Soil Burial medium consistently had the highest k values, with the B3 sample reaching its peak at 0.0283 days^{-1}. This faster soil decomposition is consistent with research by Syuhada [25], which found that soil weight loss was significantly higher (63%) than in aquatic environments, such as river water (54%), and that this was backed by higher degradation rate constants in soil media. The high rate in soil is caused by microbial enzymatic secretion, especially amylase, which actively breaks down starch chains into glucose units that can be metabolized.

Furthermore, the acidic solution medium yielded higher k values than tap water. The acidic environment promotes acid-catalyzed hydrolysis of the glycosidic bonds. The results indicate that the B3 sample degraded considerably more quickly in acidic solution (0.0253 days^{-1}) than in neutral water (0.0189 days^{-1}). This confirms that a lower pH environment provides a chemical "shortcut" for polymer chain scission. However, the design of these bioplastics must consider the specific filler type; as noted by Oblitas [26], while organic fillers generally aid decomposition, certain structural components like cellulose can sometimes slow down the degradation rate compared to pure starch controls.

In summary, this study demonstrates that by merely varying the quantity of coffee grounds added, we can regulate the rate at which the bioplastic decomposes. In plain water, the material is fairly durable, but once it is buried in the ground, it breaks down rapidly. However, this degradability is closely linked to the material's initial mechanical properties. Widantha [14] asserts that the inclusion of SCG affects both flexibility and tensile strength. A moderate filler loading of 10% (B1) was found to reinforce the structure, achieving a peak tensile strength of 2.37 MPa and a slight improvement in elongation to 32%. In contrast, higher filler concentrations (20% and 30%) led to a significant decline in tensile strength (down to 1.18 MPa) and a sharp reduction in ductility (dropping to 14% elongation). As supported by Amer [24] and Oblitas [26], this weakening of the structural matrix at higher SCG loadings not only restricts polymer chain mobility but also creates more entry points for environmental degradation agents. The B3 sample has the highest rate of degradation (0.0283 days^{-1}) and the lowest mechanical strength, which can be explained by this dual effect. While a high SCG content is best suited for applications requiring quick composting, these results demonstrate that biocomposites are a flexible and sustainable alternative to traditional packaging technologies, emphasizing the need to find a balance for packaging that demands greater mechanical durability.

4. CONCLUSION

This study concludes that the addition of SCG effectively accelerates the biodegradation of cassava starch-based bioplastics, with the rate constant peaking at 0.0283 days^{-1} in the 30% SCG formulation buried in soil. The rate of degradation is directly regulated by the concentration of SCG. The material becomes more porous and has a larger surface area when more filler is added, which enables the decomposition speed to be changed as necessary. Even though the soil environment and acidic conditions significantly improve decomposition through enzymatic activity and hydrolysis, a higher filler content results in a trade-off by lowering mechanical durability. These results show that coffee waste can be recycled to create beneficial biocomposites that actively prevent environmental buildup. It is intended that these findings will encourage broader industrial adoption of circular economy principles, ensuring that future packaging products not only serve their intended function but also safely and effectively return to the ecosystem.

5. ACKNOWLEDGEMENT

This research was financially supported by the DIPA (Budget Implementation List) of Politeknik Negeri Bali for the fiscal year 2025. The authors would like to express their sincere gratitude to the institution for the funding and facilities provided throughout the study.

6. REFERENCES

[1] M. Flury and R. Narayan, “Biodegradable plastic as an integral part of the solution to plastic waste pollution of the environment,” Current Opinion in Green and Sustainable Chemistry, vol. 30, p. 100490, 2021, doi: 10.1016/j.cogsc.2021.100490.
[2] O. M. Abel, E. G. Ifeanyi, A. S. Chinelo, G. K. Agbajor, and J. E. Imanah, "Surface Hydrophobicity of Starch Acetate for Enhanced Bioplastic Properties," J. Mater. Environ. Sci., vol. 12, no. 4, pp. 497–510, 2021.
[3] Y. Darni and H. Utami, "Studi pembuatan dan karakteristik sifat mekanik dan hidrofobisitas bioplastik dari pati sorgum," J. Rekayasa Kimia & Lingkungan, vol. 7, no. 2, 2009.
[4] A. C. Neves, T. Ming, M. Mroczkowska, and D. Culliton, "The effect of different starches in the environmental and mechanical properties of starch blended bioplastics," Adv. Sci. Technol. Eng. Syst. J., vol. 5, pp. 550–554, 2020. Doi: doi: 10.25046/aj050666
[5] M. M. Abe et al., "Advantages and disadvantages of bioplastics production from starch and lignocellulosic components," Polymers, vol. 13, no. 15, p. 2484, 2021. doi: https://doi.org/10.3390/polym13152484
[6] E. G. Özdamar and M. Ateş, "Rethinking sustainability: A research on starch based bioplastic," J. Sustain. Construct. Mater. Technol., vol. 3, no. 3, pp. 249–260, 2018. doi:https://doi.org/10.29187/jscmt.2018.28
[7] S. Jayarathna, M. Andersson, and R. Andersson, "Recent advances in starch-based blends and composites for bioplastics applications," Polymers, vol. 14, no. 21, p. 4557, 2022. doi: https://doi.org/10.3390/polym14214557
[8] R. V. Gadhave, A. Das, P. A. Mahanwar, and P. T. Gadekar, "Starch based bio-plastics: the future of sustainable packaging," Open J. Polymer Sci., 2018. doi: 10.4236/ojpchem.2018.82003
[9] R. Anugrahwidya, B. Armynah, and D. Tahir, "Bioplastics starch-based with additional fiber and nanoparticle: characteristics and biodegradation performance: a review," J. Polym. Environ., vol. 29, no. 11, pp. 3459–3476, 2021. doi:https://doi.org/10.1007/s10924-021-02152-z
[10] N. Asiah, C. Epriyani, A. Kurnia, K. Ramadhan, S. G. Hidayat, and A. Apriyantono, Profil Kopi Arabika Kintamani Bali, 2022.
[11] J. D. Hernández-Varela and D. I. Medina, "Revalorization of coffee residues: advances in the development of eco-friendly biobased potential food packaging," Polymers, vol. 15, no. 13, p. 2823, 2023. doi: https://doi.org/10.3390/polym15132823

[12] Z. Tabassum et al., "Trash to treasure: Advancing resource efficiency using waste-derived fillers as sustainable reinforcing agents in bioplastics," Mater. Adv., vol. 6, no. 2, pp. 527–546, 2025. doi :https://doi.org/10.1039/d4ma01043d
[13] K. W. Widantha, R. N. Baiti, and I. B. A. Peling, "Synthesis of hydroxyapatite from pig bone waste as adsorbent for heavy metal lead," in Proc. Int. Conf. Sustainable Green Tourism Appl. Sci. - Eng. Appl. Sci. 2024 (ICoSTAS-EAS 2024), pp. 126–133, 2024. doi: 10.2991/978-94-6463-587-4_15
[14] K. W. Widantha, R. N. Baiti, I. W. P. Y. Asana, A. Fitri, and I. B. A. Peling, "Innovative Bioplastic from Coffee Grounds Waste and Cassava Starch: A Circular Economy-Based Coffee Packaging Solution," in Proc. Int. Conf. Sustainable Green Tourism Appl. Sci.-Eng. Appl. Sci. 2025 (ICOSTAS-EAS 2025), p. 142, 2025. doi: 10.2991/978-94-6463-878-3_17
[15] R. Dewi, "Pengaruh penambahan polipropilena pada karakteristik plastik degradable berbasis pati ampas kopi," J. Teknol. Kimia Unimal, vol. 12, no. 2, pp. 274–293, 2023. doi: https://doi.org/10.29103/jtku.v12i2.13580
[16] Y. Chan, S. Phang, T. Tee, T. Lee, and T. Soo, "Preliminary study of mechanical properties in thermoplastic starch (TPS)/coffee-waste-derived fillers composites," in Proc. Eng. Undergraduate Res. Catalyst Conf. (EURECA), pp. 1–14, 2015.
[17] M. Asif et al., "Production of sustainable bioplastic derived from renewable lignocellulosic agricultural biomass: a comprehensive review," Front. Water Environ., vol. 4, no. 1, pp. 1–14, 2024. doi: https://doi.org/10.37934/fwe.4.1.114
[18] I. W. P. Y. Asana, R. N. Baiti, and K. W. Widantha, "The effect of wood sawdust surface modification with citric acid on the bending strength of wood sawdust reinforced epoxy composite," Logic: J. Rancang Bangun dan Teknol., vol. 25, no. 2, pp. 100–106, 2025. doi: https://doi.org/10.31940/logic.v25i2.100-106
[19] N. S. Payanthoth, N. N. N. Mut, P. Samanta, G. Li, and J. Jung, "A review of biodegradation and formation of biodegradable microplastics in soil and freshwater environments," Appl. Biol. Chem., vol. 67, no. 1, p. 110, 2024. doi: https://doi.org/10.1186/s13765-024-00959-7
[20] F. Degli-Innocenti et al., "Analysis of the microplastic emission potential of a starch-based biodegradable plastic material," Polym. Degrad. Stab., vol. 199, p. 109934, 2022. doi: https://doi.org/10.1016/j.polymdegradstab.2022.109934
[21] J. A. Wicaksono, T. Purwadaria, A. Yulandi, and W. A. Tan, "Bacterial dynamics during the burial of starch-based bioplastic and oxo-low-density-polyethylene in compost soil," BMC Microbiol., vol. 22, no. 1, p. 309, 2022. doi: https://doi.org/10.1186/s12866-022-02729-1
[22] M. Shanmathy, M. Mohanta, and A. Thirugnanam, "Development of biodegradable bioplastic films from Taro starch reinforced with bentonite," Carbohydrate Polym. Technol. Appl., vol. 2, p. 100173, 2021. doi: https://doi.org/10.1016/j.carpta.2021.100173
[23] A. S. Rusdianto, M. Usman, T. Lindriati, E. Ruriani, and N. S. Mahardika, "The Characterization of Biodegradable Plastics from Cassava Starch with Varried Addition of Robusta Coffee Skin (Coffea canefora) and Glycerol," Int. J. Food, Agric. Nat. Resour., vol. 3, no. 3, pp. 34–38, 2022. doi: https://doi.org/10.46676/ij-fanres.v3i3.68
[24] Z. J. A. Amer and A. Q. Saeed, "Soil burial degradation of polypropylene/starch blend," Int. J. Tech. Res. Appl., vol. 3, no. 1, pp. 91–96, 2015.
[25] M. Syuhada, S. A. Sofa, and E. Sedyadi, "The effect of cassava peel starch addition to bioplastic biodegradation based on chitosan on soil and river water media," Biol. Med. Nat. Prod. Chem., vol. 9, no. 1, pp. 7–13, 2020. doi: https://doi.org/10.14421/biomedich.2020.91.7-13
[26] R. Oblitas et al., "Physicochemical properties of bioactive bioplastics based on cellulose from coffee and cocoa by-products," Results in Chemistry, vol. 15, p. 102201, 2025. doi: https://doi.org/10.1016/j.rechem.2025.102201

LOGIC
Journal of Engineering Design and Technology
Vol. 26 No. 1 March 2026 ; p. 86 - 94

p-ISSN : 1412-114X
e-ISSN : 2580-5649
http://ojs2.pnb.ac.id/index.php/LOGIC

NUMERICAL STUDY ON THERMAL PERFORMANCE OF MINI-CHANNEL COOLING ON CYLINDRICAL LITHIUM-ION BATTERY COOLING SYSTEM

Elvi Armadani[1], James Julian[2)*], Bima Rakha Adhitama[2)], Fitri Wahyuni[2)], Riki Hendra Purba[2)], Fathin Muhammad Mahdhudhu[3)], Adi Winarta[4)]

1) Industrial Engineering, Universitas Pembangunan
2) Mechanical Engineering, Universitas Pembangunan Nasional Veteran Jakarta
3) Naval Architecture, Universitas Pembangunan Nasional Veteran Jakarta
4) Mechanical Engineering, Politeknik Negeri Bali

Corresponding email [1)] :
zames@upnvj.ac.id

Abstract. This study numerically examines the effect of liquid-based cooling on the thermal performance of a cylindrical lithium-ion battery pack under a 5C discharge rate. Proper thermal management is essential to ensure safety and extend battery life, particularly in electric vehicle applications. Three cooling-channel diameters (4, 6, and 8 *mm*) were evaluated. The 8 *mm* channel achieved the best thermal performance, with a maximum temperature of 36.2 °C and a average temperature of 33.6 °C. In contrast, the 4 *mm* channel reached 37.8 °C and produced the highest temperature gradient (8.3 °C), increasing hotspot risk. Pressure drop analysis revealed that the 4 *mm* configuration had the greatest hydraulic resistance, while 6 *mm* and 8 *mm* channels reduced ΔP by 28% and 46%, respectively. Overall, an 8 *mm* diameter provides optimal thermal uniformity and lower pumping power requirements.

Keywords : Hotspot, Li-ion battery, Liquid coooling

1. INTRODUCTION

Transportation is widely acknowledged as a major sector responsible for producing greenhouse gas emissions and contributing to deteriorating air quality in urban regions [1]. To address these issues and reduce reliance on petroleum-based fuels, the transition from conventional internal combustion vehicles to Electric Vehicles (EVs) has been increasingly advocated [1]. Lithium-ion batteries (LIB) are predominantly selected as the main energy-storage component for EVs because they possess several advantageous characteristics, including high energy density, strong power capability, extended lifespan, low self-discharge behavior, and the absence of memory effects [2]. Even so, the heat generated during charge–discharge processes can elevate the cell temperature, consequently influencing the battery's cycle durability, performance consistency, reliability, and safety [3]. If the temperature rise becomes excessive, the battery may experience hazardous events such as thermal runaway [3]. Prior investigations have indicated that lithium-ion batteries should ideally operate within a temperature window of approximately 20 °C to 40 °C, while the allowable temperature difference across the battery is recommended to remain below about 5°C [4]. This thermal control can be applied either within individual cells or across battery modules [4].

Therefore, establishing an effective battery thermal-management approach is essential. Cooling methodologies are generally categorized based on the medium involved, including air cooling [5][6], liquid cooling [7][8], heat-pipe systems [9][10], phase-change-material (PCM) cooling [11][12], and hybrid methods [13]. Among these options, air cooling is often considered the simplest technique, where airflow is directed into the battery structure using devices such as fans to enhance heat removal. Various studies have attempted to improve air-cooling performance by adjusting the airflow distribution. Yang et al. [14], for instance, demonstrated that changes in inlet angle affect the resulting airflow patterns. Additional parameters such as cell arrangement, spacing between cells, and airflow velocity have also been explored. Nonetheless, air cooling becomes less suitable for modern high-rate charge scenarios due to its inherently limited thermal-conductivity capability. Conversely, PCM-based cooling offers the advantage of reducing temperature and maintaining a low temperature gradient, although its application is restricted by the material's thermal properties and melting characteristics. Meanwhile, liquid cooling has been identified as the most effective BTMS method [15] with maximum temperature reductions of 8–14 °C and ΔT maintained within 3–5 °C [16] but its use remains constrained by structural complexity, and pumping power requirements.

This study focuses on evaluating the thermal performance of a liquid cooling system applied to cylindrical Li-ion battery packs consisting of eight cells. The research emphasizes the importance of energy efficiency, where the cooling method is expected not only to dissipate the internal heat generated during charge and discharge but also to minimize additional energy consumption. Numerical simulations are employed to analyze the effect of cold plate design variations, particularly through the use of internal channels with different inlet diameters. By maximizing the contact area between the cooling surface and the battery, these variations are proposed to improve overall uniformity across the battery pack. Furthermore, the study provides insights into enhancing both thermal safety and operational efficiency in LIB battery packs.

2. RESEARCH METHODS

2.1 Geometry of the Models

To evaluate the influence of cooling channel dimensions on the thermal performance of the battery pack, three geometric variations of the liquid cold plate were designed. Each model integrates cylindrical Li-ion cells with embedded cooling channels, allowing water to circulate and remove the generated heat. The variations are the cooling channel, where diameters were set to 4 *mm*, 6 *mm*, and 8 *mm*. The corresponding layouts of these designs are illustrated in figure 1. Specifically, model (a) represents the 4 *mm* channel configuration, model (b) corresponds to the 6 *mm* channel, and model (c) illustrates the 8 *mm* channel. These configurations were developed to investigate the relationship between channel diameter, temperature uniformity, and heat dissipation efficiency across the battery pack.

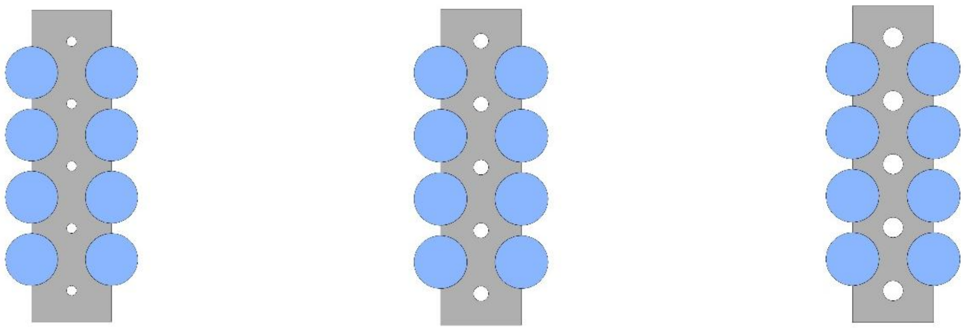

(a) (b) (c)

Figure 1. (a) 2-D view of the 4 *mm* channel on the LIBs pack, (b) 2-D view of the 6 *mm* channel on the LIBs pack, (c) 2-D view of the 8 *mm* channel on the LIBs pack

2.2 Governing Equations

To evaluate the cooling behavior of the battery system, the analysis first addresses the fluid-flow characteristics by employing the Reynolds-Averaged Navier–Stokes (RANS) formulation for mass and momentum conservation, as presented in Eq. 1 and 2 [17]. The subsequent thermal response of the battery is then described through the energy-balance relation in Eq. 3, with a heat source model based on experimental thermal characteristics at Eq. 4. This model is further developed into a parametric function in Eq. 5. The parametric coefficient was set based on Z. Rao experiment [23], representing the vertical heat inhomogeneity observed experimentally. The function was implemented in numerical software as a spatially dependent volumetric heat source using a UDF [18], [19], [20], [21]. These governing equations provide the model which ensures that the cooling channel configurations can be systematically assessed for their impact on maximum temperature, temperature uniformity, and overall thermal efficiency. [21]

$$\frac{\partial \rho}{\partial t} + \frac{\partial}{\partial x_i}(\rho u_i) = 0 \tag{1}$$

$$\frac{\partial}{\partial t}(\rho u_i) + \frac{\partial}{\partial x_i}(\rho u_i u_j) = \frac{\partial p}{\partial x_i} + \frac{\partial}{\partial x_j}\left[\mu\left(\frac{\partial u_i}{\partial x_j} + \frac{\partial u_j}{\partial x_i} - \frac{2}{3}\delta_{ij}\frac{\partial u_i}{\partial x_i}\right)\right] + \frac{\partial}{\partial x_i}\left(-\rho\overline{u_i^{'}u_j^{'}}\right) \tag{2}$$

$$\rho c_p \frac{\partial T}{\partial t} = \lambda_x \frac{\partial^2 T}{\partial^2 x} + \lambda y \frac{\partial^2 T}{\partial^2 y} + \lambda z \frac{\partial^2 T}{\partial^2 z} + Q_{gen} \tag{3}$$

$$Q_{gen}(t)=\rho c_p \frac{\Delta T}{\Delta t} \tag{4}$$

$$Q_{gen(1-3)}(x,y,z,t)=Q_{gen(1-3)}(t)-\lambda\nabla^2 T_{(1-3)} \tag{5}$$

2.3 Mesh and Boundary Conditions

To effectively capture the complex geometry of the battery cooling system, the computational domain was discretized using an unstructured tetrahedral mesh. This meshing strategy offers flexibility and accurate representation of faces at the cylindrical cells. Figure 2(a) illustrates a schematic of the liquid cooling system of the battery module, while figure 2(b) presents the mesh distribution. The system is composed of cylindrical cells embedded in an aluminum block, which incorporates five liquid coolant channels. The inlet mass flow rate was set to 0.0035 kg/s remembering pump power consumption. Velocity-inlet conditions were applied at the inlets, while a no-slip condition was applied on the internal channel surfaces. The entire module was assumed to be adiabatic, with an inlet liquid temperature fixed at 25 °C. The material properties employed in the simulation showed in Table 1.

Table 1. Material Properties

Materials	ρ (kg·m^{-3})	C (J·kg^{-1}·k^{-1})	k (W·m^{-1}·k^{-1})	μ (g m^{-1} s^{-1})
Aluminum	2719	871	202.4	-
Battery	2450	1108.4	3.917	-
Water	998.2	4128	0.6	1.003

(a) (b)

Figure 2. (a) Boundary conditions (b) Mesh

2.4 Grid Independence Test

The accuracy of Computational Fluid Dynamics (CFD) simulations is strongly influenced by the quality of the mesh employed. To ensure reliable model, a grid independence test was carried out using different meshes, where the coarse mesh consisted of 1,555×106 elements, the medium mesh of 2.333×106 elements, and the fine mesh of 3,5E×106 elements. The Richardson extrapolation technique, generalized by Roache [22], was applied as the methodological basis. Equations (9) and (10) were utilized to estimate the numerical error for both coarse and fine mesh cases, while a safety factor of 1.25 was adopted. The relative error values obtained, as presented in Table 2, indicated that mesh refinement affected the convergence index. As illustrated in figure 3, higher mesh resolution was associated with improved accuracy. Therefore, the fine mesh configuration was selected for subsequent simulations.

$$r=\frac{h_2}{h_1} \tag{7}$$

$$\bar{p}=\frac{\ln\left(\frac{f_3-f_2}{f_2-f_1}\right)}{\ln(r)} \tag{8}$$

$$GCI_{fine} = \frac{F_s \left| \in \right|}{\left(r^{\bar{p}} - 1 \right)} \quad (9)$$

$$GCI_{coarse} = \frac{F_s \left| \in \right| r^{\bar{p}}}{\left(r^{\bar{p}} - 1 \right)} \quad (10)$$

$$\in = \frac{f_{n+1} - f_n}{f_n} \quad (11)$$

$$\frac{GCI_{coarse}}{GCI_{fine} r^{\bar{p}}} \approx 1 \quad (12)$$

$$f\,\mathrm{r}_{h=0} = f_1 + \frac{(f_1 - f_2)}{\left(r^{\bar{p}} - 1 \right)} \quad (13)$$

Table 2. Result of grid convergence index

Mesh	Fine	Medium	Coarse
Difference of Temperature	35.1710	35.10881	34.82375
$p"$		3.751619273	
R		1.5	
GCI_{fine}		0.0062%	
GCI_{coarse}		0.2837%	
$f_{rh} = 0$		35.1884	
$\frac{GCI_{coarse}}{GCI_{fine} r^{p"}}$		1	
Error	0.04947%	0.22644%	1.03654%

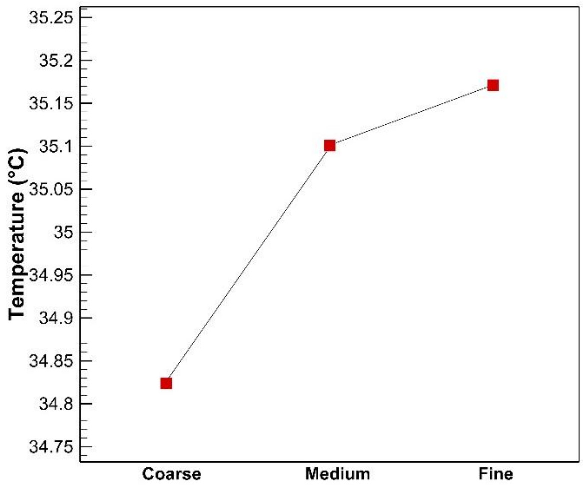

Figure 3. Mesh Sensitivity

3. RESULTS AND DISCUSSION

3.1 Validation

The experimental data utilized were obtained from the values of three heat sources who conducted by Z. Rao et. al. [23]. The setup conducted in such a way as to account for the slightly larger chemical reaction occurring at the positive terminal compared to other regions. The primary objective was the capture of vertical inhomogeneity within the battery. The experiment was performed at a discharge rate of 5C, representing high-power operating conditions in which thermal effects are more significant and critical for performance evaluation. As illustrated in figure 4, the predicted temperature closely matched the experimental data, with a maximum deviation of only 3.99%, which validates the suitability of the heat-generation model adopted in this study.

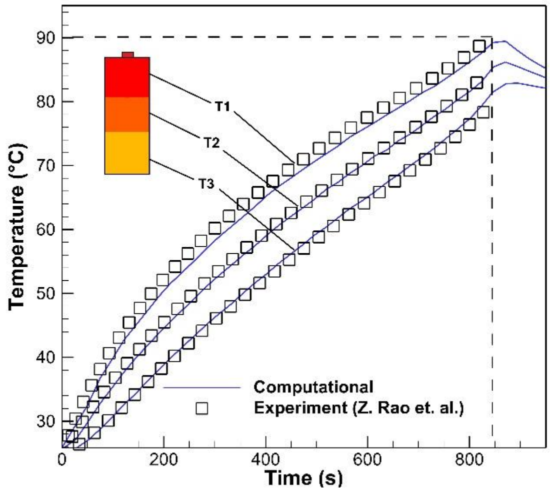

Figure 4. Validation with experiment

3.2 Analysis

Figure 5 presents the maximum temperature distribution of the battery pack for three cooling channel diameters, elucidating the influence of channel geometry on peak thermal management. In each scenario, the temperature profile initiates at 25 °C and exhibits a pronounced increase within the initial 200–300 s, subsequently followed by a gradual decline as the coolant counteracts the heat produced by internal electrochemical reactions. This transient response underscores the interplay between heat generation during 5C discharge and the thermal dissipation capacity of the liquid cooling architecture. For the *Ø4mm* configuration, the maximum temperature attains approximately 37.8 °C, representing the highest value among the three cases. The pronounced slope from 0 to 300 s reflects the restricted channel diameter, which limits coolant flow and diminishes the convective heat transfer coefficient. Consequently, thermal energy accumulates rapidly, resulting in an increased temperature gradient across the cells. Even after reaching quasi-steady-state, the temperature remains elevated at approximately 35°C, signifying suboptimal mitigation of peak thermal loads. The *Ø6mm* channel exhibits improved thermal performance, with the maximum temperature reduced to 36.9 °C.

The transient temperature rise retains an exponential character but with a diminished gradient relative to the 4mm case, indicating a more equilibrated relationship between heat generation and dissipation. The stabilized temperature decreases to approximately 34.2°C, constituting a moderate yet significant improvement in cooling efficiency. This configuration represents a balance between hydraulic resistance and effective thermal management. The *Ø8mm* channel achieves the most effective thermal management, constraining the maximum temperature to approximately 36.2 °C and stabilizing at 33.6 °C. The temperature profile within the initial 0–300 s is comparatively smoother, reflecting the superior efficacy of the enlarged flow passage in mitigating thermal accumulation. This configuration not only attenuates the overall peak temperature but also facilitates more rapid stabilization, thereby minimizing the likelihood of localized thermal hotspots. Across all configurations, the nearly superimposed temperature curves among the cells indicate a symmetrical coolant distribution. Nonetheless, smaller channel diameters yield increased peak gradients and a delayed thermal response. By contrast, the *Ø8mm* channel consistently exhibits enhanced cooling capacity, improved system stability, and superior safety margins under high-power operating conditions.

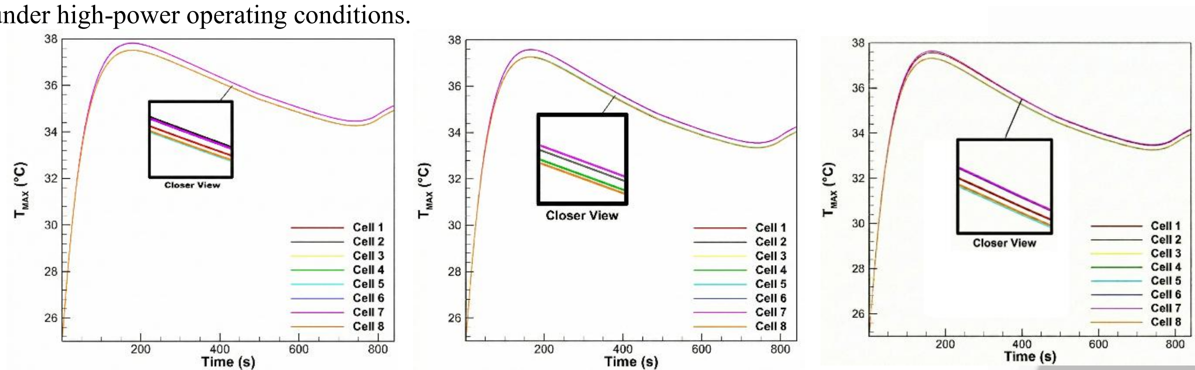

(a) (b) (c)

Figure 5. (a) Max temp. *Ø4mm* (b) Max temp. *Ø6mm* (c) Max temp. *Ø8mm*

Figure 6 presents the ΔT (temperature difference) curves for channel diameters of 4, 6, and 8 *mm*, illustrating the significance of temperature uniformity within the battery pack. All investigated configurations display a pronounced increase in temperature difference during the initial stage of discharge (0–200 s), corresponding to a period when heat generation exceeds heat dissipation. Following the peak, ΔT progressively declines as the temperature distribution among the cells approaches steady state. For the 4 *mm* channel diameter, the maximum ΔT attains 8.3 °C, the largest among the examined cases. The reduced channel dimension limits coolant flow, resulting in non-uniform heat extraction across the cells. This condition leads to the formation of localized hot spots, with cells at suboptimal cooling positions exhibiting elevated temperatures. Pronounced temperature gradients accelerate degradation mechanisms, shorten cycle life, and increase the likelihood of thermal runaway. The 6 *mm* channel demonstrates enhanced temperature uniformity.

The increased cross-sectional area facilitates improved coolant circulation, promoting more homogeneous heat removal from the cells. Although minor discrepancies persist between individual cells, the decrease in ΔT signifies a notable enhancement in thermal safety. The 8 *mm* channel achieves the most uniform temperature distribution, as ΔT is minimized. The temperature profiles of all eight cells exhibit greater overlap, indicating that heat dissipation is consistently maintained throughout the module. The smoother gradient observed during the transient phase suggests that the system effectively balances heat generation and removal, thereby limiting the development of thermal gradients. Maintaining temperature uniformity is essential for the safety and optimal performance of lithium-ion batteries. Even minor ΔT values between cells can induce non-uniform aging, with hotter cells undergoing accelerated degradation, thereby reducing the overall module capacity and lifespan. Consequently, minimizing ΔT through optimized cooling design not only enhances operational safety but also promotes long-term reliability and energy efficiency of the battery pack.

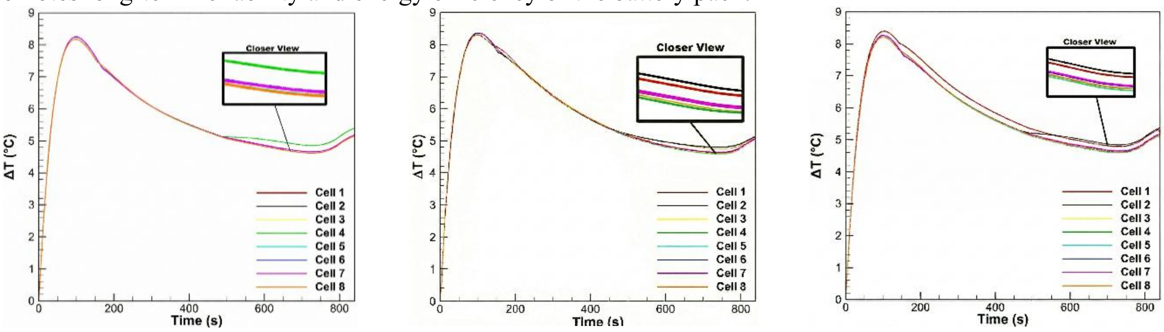

(a) (b) (c)

Figure 6. (a) ΔT *Ø4mm* (b) ΔT *Ø6mm* (c) ΔT *Ø8mm*

Table 3 presents the reduction of thermal difference for each battery cell under different cooling channel diameters of 4, 6, and 8 *mm*, compared to the baseline condition without cooling. In the no-cooling case, the maximum ΔT across the module was recorded at 59.358 °C. With the implementation of liquid cooling, all configurations demonstrate a remarkable reduction in ΔT exceeding 85%, confirming the effectiveness of channel-based cooling in suppressing temperature gradients among the cells. Specifically, the 4 *mm* channel yields an average ΔT reduction of 86.092%, the 6 *mm* channel achieves 86.108%, and the 8 *mm* channel records the highest improvement at 86.171%. The trend indicates that increasing channel diameter consistently enhances heat dissipation and promotes better thermal uniformity. It is also noteworthy that the reduction percentages remain stable across all eight cells, with only marginal variation between them. This indicates that the cooling system provides a nearly uniform cooling effect regardless of cell position, which is particularly important in cylindrical battery packs where localized hotspots are a critical issue. The slightly superior performance of the 8 *mm* configuration can be attributed to the larger conductive surface area and increased coolant flow capacity, which together improve the heat transfer rate from the cells to the coolant.

Table 3. Thermal difference reduction

Cell	**No Cooling**	***4mm***	***6mm***	***8mm***
	ΔT (°C)	ΔT reduction (%)	ΔT reduction (%)	ΔT reduction (%)
1	59.358	85.859	86.155	86.230
2		86.093	86.051	86.107
3		86.086	86.063	86.108
4		86.172	86.160	86.235
5		86.176	86.159	86.237
6		86.080	86.065	86.106
7		86.092	86.053	86.116
8		86.177	86.153	86.230
Average (%)		86.092	86.108	86.171

Figure 7 presents the pressure drop (ΔP) across the cooling channel for the three investigated diameters. The results demonstrate a clear inverse relationship between channel diameter and pressure drop. This trend is attributed to the reduction in hydraulic resistance as the channel area increases. A larger diameter reduces flow velocity and wall shear stress, thereby minimizing frictional losses along the channel. From an operational perspective, lower pressure drop directly translates into reduced pumping power requirements. Notably, the *Ø8mm* configuration not only provides the best thermal performance, but also results in the lowest hydraulic resistance.

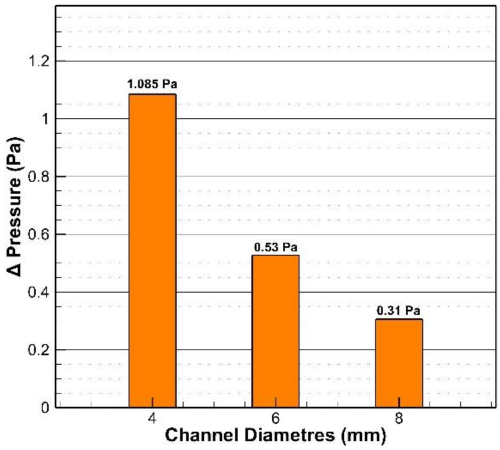

Figure 7. ΔP throughout the cooling channel

Figure 8 presents the temperature contours of the battery module under three cooling channel diameters, emphasizing the role of channel size in promoting thermal equalization and mitigating localized hotspots. At *Ø4mm* which is presented in figure 8(a), pronounced hotspot regions are observed around the mid-height of several cells, indicating localized heat accumulation and insufficient thermal dispersion. The narrow channel restricts coolant distribution, thereby limiting conduction–convection coupling and resulting in uneven temperature fields, as further evidenced by the non-uniform isothermal bands at the outlet. With an enlarged channel of *Ø6mm* presented in figure 8(b), these hotspots are significantly suppressed, and the contour distribution evolves into smoother transitions. This improvement reflects enhanced conductive spreading within the cold plate and a more effective convective heat transfer, which jointly facilitates inter-cell temperature homogenization. The *Ø8mm* configuration in figure 8(c) demonstrates the highest level of uniformity, where hotspot regions minimize consistently from inlet to outlet, and parallel contour spacing indicates a nearly isothermal module. This condition reveals that the increased channel diameter maximizes the heat removal performance, promotes more uniform gradient, and elevates the capacity for both conductive and convective dissipation. Importantly, the near elimination of localized high-temperature zones suggests a substantial improvement in thermal reliability and operational safety. Collectively, the results highlight that the enlargement of cooling channels progressively strengthens thermal equalization across the module. While *Ø6mm* offers a balanced trade-off between temperature uniformity and flow resistance, *Ø8mm* establishes itself as the optimal configuration for avoiding hotspots and ensuring stable temperature distribution, which are critical for extending the lifespan and safety of cylindrical Li-ion battery packs.

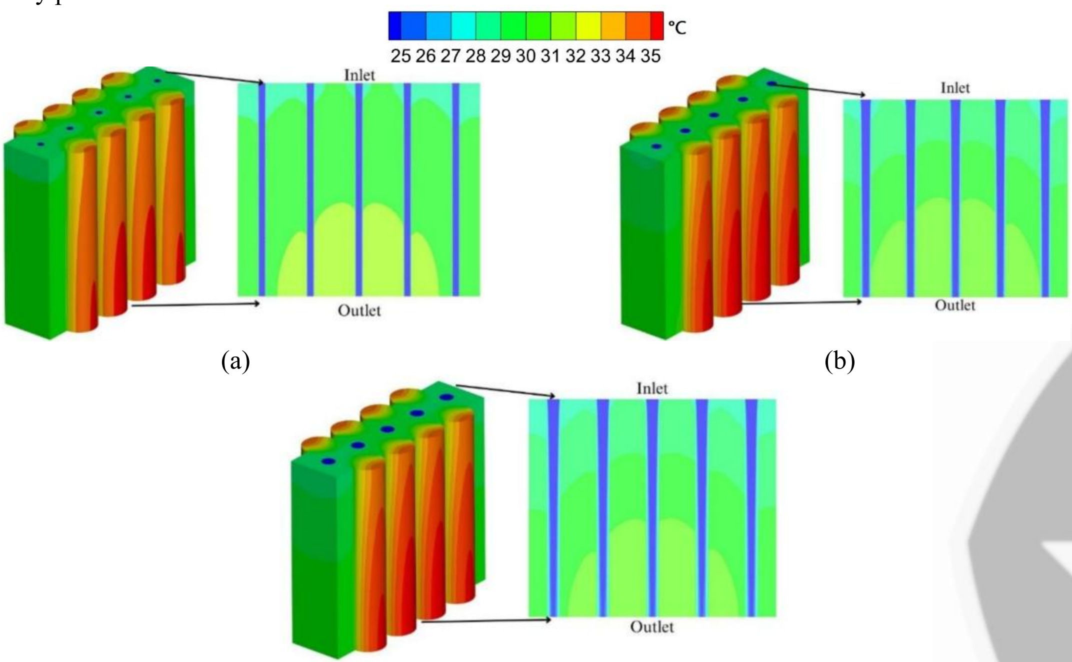

(a) (b)

(c)

Figure 8. (a) Contour at *Ø4mm* (b) Contour at *Ø6mm* (c) Contour at *Ø8mm*

4. CONCLUSION

This study numerically evaluated the thermal performance of a liquid cooling system for a cylindrical lithium-ion (Li-ion) battery pack, focusing on the effect of cooling channel diameter. Using CFD, three configurations with channel diameters of 4 *mm*, 6 *mm*, and 8 *mm* were analyzed under a high-power 5C discharge rate. The results consistently demonstrate that the channel diameter is a critical parameter for effective thermal management. The *Ø8mm* channel configuration proved to be the most effective, achieving the lowest peak and stabilized temperatures and promoting optimal temperature uniformity across the battery cells. This superior performance is due to the larger channel size, which decreases flow resistance, enhances coolant circulation, and improves heat transfer efficiency, thereby mitigating the accumulation of thermal energy. In contrast, the *Ø4mm* and *Ø6mm* channel configurations, while still providing significant temperature reduction compared to the uncooled state, were less effective. The smaller 4 *mm* channels led to higher peak temperatures, slower thermal stabilization, and a greater temperature difference (ΔT) of 8.3 °C across the cells. This non-uniformity creates localized hotspots, which can accelerate battery degradation and increase the risk of thermal runaway. In conclusion, optimizing cooling channel diameter is essential for maintaining the operational safety, performance, and longevity of Li-ion battery packs. The findings confirm that a larger channel diameter, such as the *Ø8mm* configuration, provides a substantial advantage in mitigating thermal stress and ensuring stable, uniform temperature distribution, which is crucial for high-power applications. Future research could explore the trade-offs between pumping power requirements and thermal performance for various channel geometries to further optimize battery thermal management systems.

5. REFERENCES

[1] S. Panchal, I. Dincer, M. Agelin-Chaab, R. Fraser, and M. Fowler, “Experimental and theoretical investigation of temperature distributions in a prismatic lithium-ion battery,” International Journal of Thermal Sciences, vol. 99, pp. 204–212, 2016. doi: https://doi.org/10.1016/j.ijthermalsci.2015.08.016

[2] S. Panchal, I. Dincer, M. Agelin-Chaab, R. Fraser, and M. Fowler, “Experimental and theoretical investigations of heat generation rates for a water cooled LiFePO4 battery,” Int J Heat Mass Transf, vol. 101, pp. 1093–1102, 2016. doi: https://doi.org/10.1016/j.ijheatmasstransfer.2016.05.126

[3] T. Yang, N. Yang, X. Zhang, and G. Li, “Investigation of the thermal performance of axial-flow air cooling for the lithium-ion battery pack,” International Journal of Thermal Sciences, vol. 108, pp. 132–144, 2016. doi: https://doi.org/10.1016/j.ijthermalsci.2016.05.009

[4] A. Greco, X. Jiang, and D. Cao, “An investigation of lithium-ion battery thermal management using paraffin/porous-graphite-matrix composite,” J Power Sources, vol. 278, pp. 50–68, 2015. doi: https://doi.org/10.1016/j.jpowsour.2014.12.027

[5] L. Luo, Y. Liu, Z. Liao, and J. Zhong, “Optimal structure design and heat transfer characteristic analysis of X- type air-cooled battery thermal management system,” J Energy Storage, vol. 67, p. 107681, 2023. doi: https://doi.org/10.1016/j.est.2023.107681

[6] G. Mohammed, H. Hasini, K. E. Elfeky, Q. Wang, M. A. Hajara, and N. I. Om, “Cooling effectiveness enhancement of parallel air-cooled battery system through integration with multi-phase change materials,” International Journal of Thermal Sciences, vol. 201, p. 109030, 2024. doi: https://doi.org/10.1016/j.ijthermalsci.2024.109030

[7] W. Liang et al., “Optimization design of proton exchange membrane fuel cell cooling plate based on dual- objective function topology theory,” International Communications in Heat and Mass Transfer, vol. 153, p. 107404, 2024. doi: https://doi.org/10.1016/j.icheatmasstransfer.2024.107404

[8] Q. Xu et al., “Enhancement of thermal management for cylindrical battery module based on a novel wrench- shaped design for the cold plate,” Sustainable Energy Technologies and Assessments, vol. 59, p. 103421, 2023.

[9] M. Zheng et al., “Numerical study on power battery thermal management system based on heat pipe technology,” Energy Reports, vol. 9, pp. 350–361, 2023. doi: https://doi.org/10.1016/j.seta.2023.103421

[10] J. Wang, Y. Gan, J. Liang, M. Tan, and Y. Li, “Sensitivity analysis of factors influencing a heat pipe-based thermal management system for a battery module with cylindrical cells,” Appl Therm Eng, vol. 151, pp. 475– 485, 2019. doi: https://doi.org/10.1016/j.applthermaleng.2019.02.036

[11] S. Mousavi, A. Zadehkabir, M. Siavashi, and X. Yang, "An improved hybrid thermal management system for prismatic Li-ion batteries integrated with mini-channel and phase change materials," Appl Energy, vol. 334, p. 120643, 2023. doi: https://doi.org/10.1016/j.apenergy.2023.120643
[12] Z. Liu, C. Huadan, B. Wang, and P. Li, "Coupling optimization of protruding fin and PCM in hybrid cooling system and cycle strategy matching for lithium-ion battery thermal management," International Journal of Thermal Sciences, vol. 207, p. 109372, 2025. doi: https://doi.org/10.1016/j.ijthermalsci.2024.109372
[13] L. Rong, X.-S. Bai, J.-C. Li, R.-Z. Zhang, and W.-W. Yang, "Design and optimization of a hybrid cooling configuration combining PCM and liquid cooling for Li-ion battery using data-based response surface approximation model," Appl Therm Eng, vol. 245, p. 122844, 2024. doi: https://doi.org/10.1016/j.applthermaleng.2024.122844
[14] H. Yang, G. Yang, N. Liu, S. Zhang, and Q. Gao, "Investigating the impact of inlet angle on the performance of air-cooling lithium-ion battery pack," Appl Therm Eng, vol. 263, p. 125314, 2025. doi: https://doi.org/10.1016/j.applthermaleng.2024.125314
[15] W. Wu, S. Wang, W. Wu, K. Chen, S. Hong, and Y. Lai, "A critical review of battery thermal performance and liquid based battery thermal management," Energy Convers Manag, vol. 182, pp. 262–281, 2019. doi: https://doi.org/10.1016/j.enconman.2018.12.051
[16] Wu et al., "A review on the liquid cooling thermal management system of lithium-ion batteries," Appl Energy, vol. 375, p. 124173, 2024. doi: https://doi.org/10.1016/j.apenergy.2024.124173
[17] S. M. A. Aftab, A. S. Mohd Rafie, N. A. Razak, and K. A. Ahmad, "Turbulence model selection for low Reynolds number flows," PLoS One, vol. 11, no. 4, p. e0153755, 2016. doi: https://doi.org/10.1371/journal.pone.0153755
[18] Zhang and K. Wei, "Experimental and numerical study of a passive thermal management system using flat heat pipes for lithium-ion batteries," Appl Therm Eng, vol. 166, p. 114660, 2020. doi: https://doi.org/10.1016/j.applthermaleng.2019.114660
[19] C. Wang et al., "Liquid cooling based on thermal silica plate for battery thermal management system," Int J Energy Res, vol. 41, no. 15, pp. 2468–2479, 2017. doi: https://doi.org/10.1002/er.3801
[20] Z. Wang, J. Ma, and L. Zhang, "Finite element thermal model and simulation for a cylindrical Li-ion battery," IEEE Access, vol. 5, pp. 15372–15379, 2017. doi: 10.1109/ACCESS.2017.2723436
[21] X. Peng, C. Ma, A. Garg, N. Bao, and X. Liao, "Thermal performance investigation of an air-cooled lithium-ion battery pack considering the inconsistency of battery cells," Appl Therm Eng, vol. 153, pp. 596–603, 2019. doi: https://doi.org/10.1016/j.applthermaleng.2019.03.042
[22] P. J. Roache, "Perspective: a method for uniform reporting of grid refinement studies," 1994. doi: https://doi.org/10.1115/1.2910291
[23] Rao, Y. Huo, X. Liu, and G. Zhang, "Experimental investigation of battery thermal management system for electric vehicle based on paraffin/copper foam," Journal of the Energy Institute, vol. 88, no. 3, pp. 241–246, 2015. doi: https://doi.org/10.1016/j.joei.2014.09.006